

Utah State University

DigitalCommons@USU

All Graduate Theses and Dissertations

Graduate Studies

5-2017

Applications of Relative Motion Models Using Curvilinear Coordinate Frames

Alex C. Perez
Utah State University

Follow this and additional works at: <https://digitalcommons.usu.edu/etd>

 Part of the [Mechanical Engineering Commons](#)

Recommended Citation

Perez, Alex C., "Applications of Relative Motion Models Using Curvilinear Coordinate Frames" (2017). *All Graduate Theses and Dissertations*. 5529.
<https://digitalcommons.usu.edu/etd/5529>

This Dissertation is brought to you for free and open access by the Graduate Studies at DigitalCommons@USU. It has been accepted for inclusion in All Graduate Theses and Dissertations by an authorized administrator of DigitalCommons@USU. For more information, please contact digitalcommons@usu.edu.



APPLICATIONS OF RELATIVE MOTION MODELS USING CURVILINEAR
COORDINATE FRAMES

by

Alex C. Perez

A dissertation submitted in partial fulfillment
of the requirements for the degree

of

DOCTOR OF PHILOSOPHY

in

Mechanical Engineering

Approved:

David K. Geller, Ph.D.
Major Professor

R. Rees Fullmer, Ph.D.
Committee Member

Stephen A. Whitmore, Ph.D.
Committee Member

T. Alan Lovell, Ph.D.
Committee Member

Jacob Gunther, Ph.D.
Committee Member

Mark R. McLellan, Ph.D.
Vice President for Research and Dean
of the School of Graduate Studies

UTAH STATE UNIVERSITY
Logan, Utah

2017

Copyright © Alex C. Perez 2017

All Rights Reserved

ABSTRACT

Applications of Relative Motion Models Using Curvilinear Coordinate Frames

by

Alex C. Perez, Doctor of Philosophy

Utah State University, 2017

Major Professor: David K. Geller, Ph.D.
Department: Mechanical and Aerospace Engineering

An angles-only initial relative orbit determination algorithm is derived using three line-of-sight observations or six angle measurements. This is accomplished by taking a Singular Value Decomposition of a 6x6 matrix to get a right singular vector approximately in the direction of the initial line-of-sight vector. Then an approximate initial relative orbit determination algorithm is derived that computes the range from the chief to the deputy vehicle. This involves the approximate solution of 6 polynomial equations in 6 unknowns. An iterative improvement is also derived that provides the exact solution, to numerical precision, of the 6 polynomial equations in 6 unknowns. The initial relative orbit algorithm is also expanded for more than three line-of-sight observations with an iterative improvement algorithm for more than three line-of-sight observations. The algorithm is tested for a range of relative motion cases in low earth orbit and geosynchronous orbit, with and without the inclusion of J_2 perturbations and with camera measurement errors.

(172 pages)

PUBLIC ABSTRACT

Applications of Relative Motion Models Using Curvilinear Coordinate Frames

Alex C. Perez

A new angles-only initial relative orbit determination (IROD) algorithm is derived using three line-of-sight observations. This algorithm accomplishes this by taking a Singular Value Decomposition of a 6x6 matrix to arrive at an approximate initial relative orbit determination solution. This involves the approximate solution of 6 polynomial equations in 6 unknowns. An iterative improvement algorithm is also derived that provides the exact solution, to numerical precision, of the 6 polynomial equations in 6 unknowns. The initial relative orbit algorithm is also expanded for more than three line-of-sight observations with an iterative improvement algorithm for more than three line-of-sight observations. The algorithm is tested for a range of relative motion cases in low earth orbit and geosynchronous orbit, with and without the inclusion of J_2 perturbations and with camera measurement errors. The performance of the IROD algorithm is evaluated for these cases and show that the tool is most accurate at low inclinations and eccentricities. Results are also presented that show the importance of including J_2 perturbations when modelling the relative orbital motion for accurate IROD estimates. This research was funded in part by the Air Force Research Lab, Albuquerque, NM.

ACKNOWLEDGMENTS

Bernard of Chartres, when talking about the advancements in science of modern men, said, “We are like dwarves perched on the shoulders of giants, and thus we are able to see more and farther than the latter. And it is not at all because of the acuteness of our sight or the stature of our body, but because we are carried aloft and elevated by the magnitude of the giants.” Without a doubt there have been many giants in my path that have lifted this little dwarf (me) to greater heights. I have no misgivings that the work I have done has been accomplished by me alone. These giants have been ever-present and ever-helpful in lifting me and letting me see further.

I would like to thank the members of my committee. Each of them have taught me, worked with me and employed me in my road to pursuing an education and finishing this dissertation. Through small acts, probably imperceptible to them, they have helped me to learn and helped shape my career at this early stage.

I would especially like to thank Dr. David Geller for his faith in me, taking me under his wing and starting me on a path that has culminated in this work. Dr. Geller is the best, most patient teacher and a true friend. A lot of long days and late nights went into this research and Dr. Geller was never far and always there to answer my questions.

This research and every good thing in my life would not have been possible without my supportive wife, Maggie. She has been my personal cheerleader and an anchor from the storms. She has helped trek to different states for internships and opportunities for me with no thought for her personal comfort. She has been my best friend and faithful supporter all these years. This work would not have been possible without her and she deserves all of the credit I can give her. My children, Clarke, Hattie, and Albert have been shining lights to me and made every long day worth it.

CONTENTS

	Page
ABSTRACT	iii
PUBLIC ABSTRACT	iv
ACKNOWLEDGMENTS	v
LIST OF TABLES	ix
LIST OF FIGURES	xv
ACRONYMS	xvii
1 INTRODUCTION	1
1.1 Dissertation Thesis Statement	2
1.2 Scope	3
1.3 Objectives	4
1.4 Dissertation Overview	4
2 ORBITAL RELATIVE MOTION	6
2.1 Satellite Relative Motion Trajectories	6
2.1.1 Chief and Deputy	6
2.1.2 V-bar Station-keeping	7
2.1.3 Flyby Orbit	7
2.1.4 Hopping Orbit	8
2.1.5 Football Orbit	9
2.1.6 Cross-track Sinusoidal Orbit	10
2.1.7 Combinations of Relative Motion Trajectories	10
2.2 Relative Satellite Motion Models	10
2.3 Derivation of Tschauner-Hempel Equations	13
3 INITIAL RELATIVE ORBIT DETERMINATION INCLUDING CAMERA OFF- SET	19
3.1 Problem Formulation	19
3.2 General Solution to the Initial Relative Orbit Determination Problem	22
3.2.1 $N > 3$ Observations	25
3.2.2 Observations of Known Target Features	27
3.3 Performance Analysis for Leader-Follower Cases with Constant Attitude	28
3.3.1 Three Observations	29
3.3.2 More than Three Observations	32
3.4 Conclusions	34

4	ORBITAL RELATIVE MOTION IN SPHERICAL COORDINATES	36
4.1	Relative Satellite Motion Equations with J_2 Perturbations	38
4.2	Linearized Equations of Motion with J_2	43
5	INITIAL RELATIVE ORBIT DETERMINATION PROBLEM, $N = 3$ OBSERVA- TIONS	47
5.1	Initial Orbit Determination	47
5.2	Initial Relative Orbit Determination	47
5.3	Line-Of-Sight Measurements	49
5.4	Derivation of LOS Measurement Equations	50
5.4.1	First-Order Measurement Equation Expansion	54
5.4.2	Second-Order Measurement Equation Expansion	54
5.5	Approximate Angles-Only IROD Solution, $N = 3$ Observations	56
5.6	Improving the IROD Solution, $N = 3$ Observations	61
5.7	Feasible Root Selection Process	62
5.8	IROD Performance Tables (Simplified Models)	68
6	INITIAL RELATIVE ORBIT DETERMINATION PROBLEM, $N > 3$ OBSERVA- TIONS	75
6.1	Approximate Angles-Only IROD Solution, $N > 3$ Observations	75
6.2	Improving the IROD Solution, $N > 3$ Observations	79
6.3	IROD Performance Tables (Simplified Models)	81
6.3.1	$N=4$ Observations, Simplified Models	82
6.3.2	$N=13$ Observations, Simplified Models	84
6.3.3	$N=25$ Observations, Simplified Models	86
7	LOW EARTH ORBIT RESULTS	89
7.1	$N=4$ Observations, Nonlinear Dynamics, $\Delta t = 1000 \text{ sec}$	89
7.2	$N=13$ Observations, Nonlinear Dynamics, $\Delta t = 250 \text{ sec}$	94
7.3	$N=25$ Observations, Nonlinear Dynamics, $\Delta t = 125 \text{ sec}$	96
8	EFFECT OF EXCLUDING J_2 FROM IROD ALGORITHM FOR LEO	102
8.1	$N=4$ Observations, Nonlinear Dynamics, $\Delta t = 1000 \text{ sec}$	102
8.2	$N=13$ Observations, Nonlinear Dynamics, $\Delta t = 250 \text{ sec}$	105
8.3	Summarizing Remarks	108
9	MEASUREMENT ERROR ANALYSIS	111
9.1	Measurement Error Analysis at LEO	111
9.1.1	Leader-Follower 5 km	112
9.1.2	Leader-Follower 10 km	113
9.1.3	Leader-Follower 100 km	115
9.1.4	Leader-Follower 500 km	117
9.2	Measurement Error Analysis for GEO	118
9.2.1	Leader-Follower 5 km	119
9.2.2	Leader-Follower 10 km	120
9.2.3	Leader-Follower 100 km	122
9.2.4	Leader-Follower 500 km	123

10	GEOSTATIONARY ORBIT RESULTS	126
10.1	N=4 Observations, Nonlinear Dynamics, $\Delta t = 9600 \text{ sec}$	126
10.2	N=13 Observations, Nonlinear Dynamics, $\Delta t = 2400 \text{ sec}$	128
10.3	N=25 Observations, Nonlinear Dynamics, $\Delta t = 1200 \text{ sec}$	130
10.4	N=4 Observations, Nonlinear Dynamics, Excluding J_2 from IROD	132
10.5	N=13 Observations, Nonlinear Dynamics, Excluding J_2 from IROD	134
10.6	N=25 Observations, Nonlinear Dynamics, Excluding J_2 from IROD	136
11	SUMMARY AND CONCLUSIONS	139
	REFERENCES	145
	CURRICULUM VITAE	152

LIST OF TABLES

Table		Page
5.1	First of Three Feasible IROD Solutions and Residuals	67
5.2	Second of Three Feasible IROD Solutions and Residuals	67
5.3	Third of Three Feasible IROD Solutions and Residuals	67
5.4	Color-Code Categorization for Percent Position Tables	72
5.5	Percent Position Errors, Simplified Models, Leader-Follower, $N = 3$, $\Delta t = 1000 \text{ sec}$, $\Delta z = 10\%$	72
5.6	Percent Position Errors, Simplified Models, Flyby, $N = 3$, $\Delta t = 1000 \text{ sec}$, $\Delta z = 10\%$	73
5.7	Percent Position Errors, Simplified Models, Football, $N = 3$, $\Delta t = 1000 \text{ sec}$, $\Delta z = 10\%$	74
6.1	Percent Position Errors, Simplified Models, Leader-Follower, $N = 4$, $\Delta t = 1000 \text{ sec}$, $\Delta z = 0\%$	82
6.2	Percent Position Errors, Simplified Models, Flyby, $N = 4$, $\Delta t = 1000 \text{ sec}$, $\Delta z = 0\%$	83
6.3	Percent Position Errors, Simplified Models, Football, $N = 4$, $\Delta t = 1000 \text{ sec}$, $\Delta z = 0\%$	83
6.4	Percent Position Errors, Simplified Models, Leader-Follower, $N = 13$, $\Delta t = 250 \text{ sec}$, $\Delta z = 0\%$	84
6.5	Percent Position Errors, Simplified Models, Flyby, $N = 13$, $\Delta t = 250 \text{ sec}$, $\Delta z = 0\%$	85
6.6	Percent Position Errors, Simplified Models, Football, $N = 13$, $\Delta t = 250 \text{ sec}$, $\Delta z = 0\%$	85
6.7	Percent Position Errors, Simplified Models, Leader-Follower, $N = 25$, $\Delta t = 125 \text{ sec}$, $\Delta z = 0\%$	86
6.8	Percent Position Errors, Simplified Models, Leader-Follower, $N = 25$, $\Delta t = 125 \text{ sec}$, $\Delta z = 0\%$	87

6.9	Percent Position Errors, Simplified Models, Leader-Follower, $N = 25$, $\Delta t = 125 \text{ sec}$, $\Delta z = 0\%$	88
7.1	Percent Position Errors, Nonlinear, Leader-Follower, $N = 4$, $\Delta t = 1000 \text{ sec}$, $\Delta z = 0\%$	90
7.2	Percent Position Errors, Nonlinear, Flyby, $N = 4$, $\Delta t = 1000 \text{ sec}$, $\Delta z = 0\%$	90
7.3	Percent Position Errors, Nonlinear, Football, $N = 4$, $\Delta t = 1000 \text{ sec}$, $\Delta z = 0\%$	91
7.4	Percent Position Errors, Nonlinear, Leader-Follower, $N = 4$, $\Delta t = 1000 \text{ sec}$, $\Delta z = 10\%$	92
7.5	Percent Position Errors, Nonlinear, Flyby, $N = 4$, $\Delta t = 1000 \text{ sec}$, $\Delta z = 10\%$	93
7.6	Percent Position Errors, Nonlinear, Football, $N = 4$, $\Delta t = 1000 \text{ sec}$, $\Delta z = 10\%$	93
7.7	Percent Position Errors, Nonlinear, Leader-Follower, $N = 13$, $\Delta t = 250 \text{ sec}$, $\Delta z = 0\%$	94
7.8	Percent Position Errors, Nonlinear, Flyby, $N = 13$, $\Delta t = 250 \text{ sec}$, $\Delta z = 0\%$	95
7.9	Percent Position Errors, Nonlinear, Football, $N = 13$, $\Delta t = 250 \text{ sec}$, $\Delta z = 0\%$	95
7.10	Percent Position Errors, Nonlinear, Leader-Follower, $N = 13$, $\Delta t = 250 \text{ sec}$, $\Delta z = 10\%$	96
7.11	Percent Position Errors, Nonlinear, Flyby, $N = 13$, $\Delta t = 250 \text{ sec}$, $\Delta z = 10\%$	97
7.12	Percent Position Errors, Nonlinear, Football, $N = 13$, $\Delta t = 250 \text{ sec}$, $\Delta z = 10\%$	97
7.13	Percent Position Errors, Nonlinear, Leader-Follower, $N = 25$, $\Delta t = 125 \text{ sec}$, $\Delta z = 0\%$	98
7.14	Percent Position Errors, Nonlinear, Flyby, $N = 25$, $\Delta t = 125 \text{ sec}$, $\Delta z = 0\%$	98
7.15	Percent Position Errors, Nonlinear, Football, $N = 25$, $\Delta t = 125 \text{ sec}$, $\Delta z = 0\%$	99
7.16	Percent Position Errors, Nonlinear, Leader-Follower, $N = 25$, $\Delta t = 125 \text{ sec}$, $\Delta z = 10\%$	99
7.17	Percent Position Errors, Nonlinear, Flyby, $N = 25$, $\Delta t = 125 \text{ sec}$, $\Delta z = 10\%$	100
7.18	Percent Position Errors, Nonlinear, Football, $N = 25$, $\Delta t = 125 \text{ sec}$, $\Delta z = 10\%$	100
8.1	Percent Position Errors, Nonlinear, Leader-Follower, $N = 4$, $\Delta t = 1000 \text{ sec}$, $\Delta z = 0\%$, NO IROD J_2	103

8.2	Percent Position Errors, Nonlinear, Flyby, $N = 4$, $\Delta t = 1000 \text{ sec}$, $\Delta z = 0\%$, NO IROD J_2	104
8.3	Percent Position Errors, Nonlinear, Football, $N = 4$, $\Delta t = 1000 \text{ sec}$, $\Delta z = 0\%$, NO IROD J_2	104
8.4	Percent Position Errors, Nonlinear, Leader-Follower, $N = 4$, $\Delta t = 1000 \text{ sec}$, $\Delta z = 10\%$, NO IROD J_2	105
8.5	Percent Position Errors, Nonlinear, Flyby, $N = 4$, $\Delta t = 1000 \text{ sec}$, $\Delta z = 10\%$, NO IROD J_2	106
8.6	Percent Position Errors, Nonlinear, Football, $N = 4$, $\Delta t = 1000 \text{ sec}$, $\Delta z = 10\%$, NO IROD J_2	106
8.7	Percent Position Errors, Nonlinear, Leader-Follower, $N = 13$, $\Delta t = 250 \text{ sec}$, $\Delta z = 0\%$, NO IROD J_2	107
8.8	Percent Position Errors, Nonlinear, Flyby, $N = 13$, $\Delta t = 250 \text{ sec}$, $\Delta z = 0\%$, NO IROD J_2	107
8.9	Percent Position Errors, Nonlinear, Football, $N = 13$, $\Delta t = 250 \text{ sec}$, $\Delta z = 0\%$, NO IROD J_2	108
8.10	Percent Position Errors, Nonlinear, Leader-Follower, $N = 13$, $\Delta t = 250 \text{ sec}$, $\Delta z = 10\%$, NO IROD J_2	109
8.11	Percent Position Errors, Nonlinear, Flyby, $N = 13$, $\Delta t = 250 \text{ sec}$, $\Delta z = 10\%$, NO IROD J_2	109
8.12	Percent Position Errors, Nonlinear, Football, $N = 13$, $\Delta t = 250 \text{ sec}$, $\Delta z = 10\%$, NO IROD J_2	110
9.1	Azimuth and Elevation Angles from L2O environment and Nonlinear Dynamics for a Leader-Follower 5 km LEO case.	112
9.2	Percent Position Errors and Standard Deviation with varying magnitudes of measurement noise added to L2O LOS angles for 100 Monte Carlo Runs (Leader-Follower 5 km LEO)	113
9.3	Percent Position Errors and Standard Deviation with varying magnitudes of measurement noise added to Nonlinear LOS angles for 100 Monte Carlo Runs (Leader-Follower 5 km LEO)	113
9.4	Azimuth and Elevation Angles from L2O environment and Nonlinear Dynamics for a Leader-Follower 10 km LEO case.	114

9.5	Percent Position Errors and Standard Deviation with varying magnitudes of measurement noise added to L2O LOS angles for 100 Monte Carlo Runs (Leader-Follower 10 km LEO)	114
9.6	Percent Position Errors and Standard Deviation with varying magnitudes of measurement noise added to Nonlinear LOS angles for 100 Monte Carlo Runs (Leader-Follower 10 km LEO)	115
9.7	Azimuth and Elevation Angles from L2O environment and Nonlinear Dynamics for a Leader-Follower 100 km LEO case.	115
9.8	Percent Position Errors and Standard Deviation with varying magnitudes of measurement noise added to L2O LOS angles for 100 Monte Carlo Runs (Leader-Follower 100 km LEO)	116
9.9	Percent Position Errors and Standard Deviation with varying magnitudes of measurement noise added to Nonlinear LOS angles for 100 Monte Carlo Runs (Leader-Follower 100 km LEO)	116
9.10	Azimuth and Elevation Angles from L2O environment and Nonlinear Dynamics for a Leader-Follower 500 km LEO case.	117
9.11	Percent Position Errors and Standard Deviation with varying magnitudes of measurement noise added to L2O LOS angles for 100 Monte Carlo Runs (Leader-Follower 500 km LEO)	118
9.12	Percent Position Errors and Standard Deviation with varying magnitudes of measurement noise added to Nonlinear LOS angles for 100 Monte Carlo Runs (Leader-Follower 500 km LEO)	118
9.13	Azimuth and Elevation Angles from L2O environment and Nonlinear Dynamics for a Leader-Follower 5 km GEO case.	119
9.14	Percent Position Errors and Standard Deviation with varying magnitudes of measurement noise added to L2O LOS angles for 100 Monte Carlo Runs (Leader-Follower 5 km GEO)	120
9.15	Percent Position Errors and Standard Deviation with varying magnitudes of measurement noise added to Nonlinear LOS angles for 100 Monte Carlo Runs (Leader-Follower 5 km GEO)	120
9.16	Azimuth and Elevation Angles from L2O environment and Nonlinear Dynamics for a Leader-Follower 10 km GEO case.	120
9.17	Percent Position Errors and Standard Deviation with varying magnitudes of measurement noise added to L2O LOS angles for 100 Monte Carlo Runs (Leader-Follower 10 km GEO)	121

9.18	Percent Position Errors and Standard Deviation with varying magnitudes of measurement noise added to Nonlinear LOS angles for 100 Monte Carlo Runs (Leader-Follower 10 km GEO)	121
9.19	Azimuth and Elevation Angles from L2O environment and Nonlinear Dynamics for a Leader-Follower 100 km GEO case.	122
9.20	Percent Position Errors and Standard Deviation with varying magnitudes of measurement noise added to L2O LOS angles for 100 Monte Carlo Runs (Leader-Follower 100 km GEO)	123
9.21	Percent Position Errors and Standard Deviation with varying magnitudes of measurement noise added to Nonlinear LOS angles for 100 Monte Carlo Runs (Leader-Follower 100 km GEO)	123
9.22	Azimuth and Elevation Angles from L2O environment and Nonlinear Dynamics for a Leader-Follower 500 km GEO case.	123
9.23	Percent Position Errors and Standard Deviation with varying magnitudes of measurement noise added to L2O LOS angles for 100 Monte Carlo Runs (Leader-Follower 500 km GEO)	124
9.24	Percent Position Errors and Standard Deviation with varying magnitudes of measurement noise added to Nonlinear LOS angles for 100 Monte Carlo Runs (Leader-Follower 500 km GEO)	124
10.1	Percent Position Errors, $N = 4$, $\Delta t = 9600 s$, $\Delta z = 0\%$, $e = 0$	127
10.2	Percent Position Errors, $N = 4$, $\Delta t = 9600 s$, $\Delta z = 0\%$, $e = 0.001$	127
10.3	Percent Position Errors, $N = 4$, $\Delta t = 9600 s$, $\Delta z = 10\%$, $e = 0$	127
10.4	Percent Position Errors, $N = 4$, $\Delta t = 9600 s$, $\Delta z = 10\%$, $e = 0.001$	128
10.5	Percent Position Errors, $N = 13$, $\Delta t = 2400 s$, $\Delta z = 0\%$, $e = 0$	128
10.6	Percent Position Errors, $N = 13$, $\Delta t = 2400 s$, $\Delta z = 0\%$, $e = 0.001$	129
10.7	Percent Position Errors, $N = 13$, $\Delta t = 2400 s$, $\Delta z = 10\%$, $e = 0$	129
10.8	Percent Position Errors, $N = 13$, $\Delta t = 2400 s$, $\Delta z = 10\%$, $e = 0.001$	129
10.9	Percent Position Errors, $N = 25$, $\Delta t = 1200 s$, $\Delta z = 0\%$, $e = 0$	130
10.10	Percent Position Errors, $N = 25$, $\Delta t = 1200 s$, $\Delta z = 0\%$, $e = 0.001$	130
10.11	Percent Position Errors, $N = 25$, $\Delta t = 1200 s$, $\Delta z = 10\%$, $e = 0$	131

10.12	Percent Position Errors, $N = 25$, $\Delta t = 1200 s$, $\Delta z = 0\%$, $e = 0$	131
10.13	Percent Position Errors, $N = 4$, $\Delta t = 9600 s$, $\Delta z = 0\%$, $e = 0$, NO IROD J_2	133
10.14	Percent Position Errors, $N = 4$, $\Delta t = 9600 s$, $\Delta z = 0\%$, $e = 0.001$, NO IROD J_2	133
10.15	Percent Position Errors, $N = 4$, $\Delta t = 9600 s$, $\Delta z = 10\%$, $e = 0$, NO IROD J_2	133
10.16	Percent Position Errors, $N = 4$, $\Delta t = 9600 s$, $\Delta z = 10\%$, $e = 0.001$, NO IROD J_2	134
10.17	Percent Position Errors, $N = 13$, $\Delta t = 2400 s$, $\Delta z = 0\%$, $e = 0$, NO IROD J_2	134
10.18	Percent Position Errors, $N = 13$, $\Delta t = 2400 s$, $\Delta z = 0\%$, $e = 0.001$, NO IROD J_2	135
10.19	Percent Position Errors, $N = 13$, $\Delta t = 2400 s$, $\Delta z = 10\%$, $e = 0$, NO IROD J_2	135
10.20	Percent Position Errors, $N = 13$, $\Delta t = 2400 s$, $\Delta z = 10\%$, $e = 0.001$, NO IROD J_2	135
10.21	Percent Position Errors, $N = 25$, $\Delta t = 1200 s$, $\Delta z = 0\%$, $e = 0$, NO IROD J_2	136
10.22	Percent Position Errors, $N = 25$, $\Delta t = 1200 s$, $\Delta z = 0\%$, $e = 0.001$, NO IROD J_2	137
10.23	Percent Position Errors, $N = 25$, $\Delta t = 1200 s$, $\Delta z = 10\%$, $e = 0$, NO IROD J_2	137
10.24	Percent Position Errors, $N = 25$, $\Delta t = 1200 s$, $\Delta z = 10\%$, $e = 0.001$, NO IROD J_2	137

LIST OF FIGURES

Figure	Page
2.1 Definition of LVLH coordinate frame	7
2.2 V-bar Station-keeping Left: Inertial Frame. Right: LVLH frame.	8
2.3 Flyby Orbit. Left: Inertial Frame. Right: LVLH frame.	8
2.4 Hopping Orbit Left: Inertial Frame. Right: LVLH frame.	9
2.5 Football Orbit Left: Inertial Frame. Right: LVLH frame.	9
2.6 Cross-track Sinusoidal Orbit Left: Inertial Frame. Right: LVLH frame.	10
3.1 IROD Camera Offset Problem Formulation	20
3.2 Downrange position error (3σ) based on 1000 Monte Carlo samples as a function of the time-interval between observations and camera offset orientation for $\sigma_{cam} = 1 \times 10^{-5} rad$	30
3.3 Downrange position error (3σ) based on 1000 Monte Carlo samples as a function of the time-interval between observations and camera offset orientation for $\sigma_{cam} = 1 \times 10^{-4} rad$	31
3.4 Downrange position error (3σ) based on 1000 Monte Carlo samples as a function of the time-interval between observations and camera offset orientation for $\sigma_{cam} = 1 \times 10^{-3} rad$	31
3.5 Downrange position error (3σ) based on 1000 Monte Carlo samples as a function of the time-interval between observations and the number of observations ($N = 3, 4, 5,$ and 6) for $\sigma_{cam} = 1 \times 10^{-5} rad$	32
3.6 Downrange position error (3σ) based on 1000 Monte Carlo samples as a function of the time-interval between observations and the number of observations ($N = 3, 4, 5,$ and 6) for $\sigma_{cam} = 1 \times 10^{-4} rad$	33
3.7 Downrange position error (3σ) based on 1000 Monte Carlo samples as a function of the time-interval between observations and the number of observations ($N = 3, 4, 5,$ and 6) for $\sigma_{cam} = 1 \times 10^{-3} rad$	33
4.1 Spherical Coordinate Frame with Two Neighboring Satellites	39

5.1	Line-Of-Sight in Spherical Coordinates for an Arbitrary Chief Inclination . .	50
5.2	Leader-Follower Relative Motion Simulation, 500 km Separation, LEO, $N = 4$ Observations, $T_f = 3000 \text{ sec}$	70
5.3	Flyby Relative Motion Simulation, 500 km DownrangeSeparation, 70 km LEO, $N = 4$ Observations, $T_f = 3000 \text{ sec}$	70
5.4	Football Relative Motion Simulation, 500 km Downrange Separation, LEO, $N = 4$ Observations, $T_f = 3000 \text{ sec}$	71

ACRONYMS

AON	angles-only navigation
DOF	degree of freedom
ECI	earth-centered inertial frame
GN&C	guidance, navigation, and control
HCW	Hill-Clohessy Wiltshire
IOD	initial orbit determination
IROD	initial relative orbit determination
LEO	low-earth orbit
LIDAR	light detection and ranging
LVLH	local vertical local horizontal frame
LOS	Line-of-sight
RPO	rendezvous and proximity operations
RSS	root-sum-square

CHAPTER 1

INTRODUCTION

The number of operational satellites and space debris is increasing at an exponential rate. Determining the orbits of threatening space debris is an essential task for ensuring the safety of satellite assets. Many space debris objects are too small for classical orbit determination techniques to track and catalog. One way of determining these unknown or currently un-tracked objects is through *relative* orbit determination techniques.

With the increases in relative orbital motion operations necessary for relative orbit determination, there is a need to find simple but accurate relative satellite motion models. The Hill-Clohessy-Wiltshire (HCW) equations [1] provide a linearized description for the relative motion between two space objects in orbit. These equations, which have a time-explicit solution, are most commonly expressed in a Cartesian (relative) coordinate frame. While the Cartesian solution yields a useful approximation of the relative trajectory given initial conditions, it has limitations in accuracy. The HCW equations require linearizing assumptions that do not accurately capture the curvature of orbits (e.g. they produce incorrect drift rates [2]) because the formulation of the relative motion problem is in Cartesian coordinates. Ideally, these linearized equations should be derived using a coordinate frame that more naturally captures the curvature and conic behavior of orbits. The main idea is that a curvilinear coordinate frame can innately capture more information about the true motion of an orbit than a Cartesian coordinate frame.

As a brief example, the comparison between a Cartesian frame and a curvilinear coordinate frame, when applied to the relative navigation observability problem, is instructive. For example, it has been mathematically proven that, if two satellites are moving in free motion, when the dynamics are modeled with the Cartesian HCW equations, using angles-only measurements to determine the relative position and velocity of a spacecraft is impossible [3]. In this case the relative navigation problem is unobservable. More recent

work has shown that if the angles-only relative navigation problem is instead formulated using relative motion equations derived from a cylindrical coordinate frame, the relative states can be determined and the navigation problem is observable [4].

The idea that formulating relative orbital motion in a curvilinear coordinate frame can provide more accuracy over the Cartesian coordinate frame has been expressed by a few researchers [5], [6]. The relative satellite motion equations derived in a curvilinear coordinate frame have different linearizing assumptions that provide more accuracy in the downrange direction than in the Cartesian coordinate frame. Ideally, if the satellite relative equations of motion can be formulated in curvilinear coordinates, a new initial relative orbit determination solution can be developed.

Previous research has shown that the effects of the J_2 perturbation can be significant for relative satellite motion. Ref. [7] has also shown that the J_2 perturbation is the second most significant perturbation after the two-body gravity force for satellites that are in Low Earth Orbits (LEO). The next logical step is formulating an initial relative orbit determination technique that factors in the perturbations due to J_2 effects.

Orbit determination techniques have been used by astronomers for centuries to determine the orbits of other planets, moons, comets and other orbiting satellites. Initial relative orbit determination is very similar to typical orbit determination algorithms. Relative orbit determination involves one satellite observing the neighboring, unknown object of interest and using either angle measurements or range measurements, determining the relative position and velocity states. These relative position and velocity states can be combined with a priori knowledge of the satellites inertial states to determine the inertial position and velocity of the unknown object of interest. Angle measurements from a camera have several advantages over range measurements. Cameras are lightweight, low-power, and more covert than range measurement techniques. There are several IROD algorithms that currently exist [8–13], though, none have implemented J_2 perturbations.

1.1 Dissertation Thesis Statement

Casting relative satellite motion equations in curvilinear coordinate frames, including

J_2 perturbations, allows the derivation of an approximate initial relative orbit determination algorithm that is of a higher fidelity than any other currently available.

1.2 Scope

This research lays down the derivation of new relative satellite motion equations with J_2 perturbations in spherical coordinates. Equations are derived for an initial relative orbit determination scheme for three observations and greater than three observations using angle measurements only. Results for a variety of orbits at LEO and GEO are presented with varying the inclinations, eccentricities, relative motion trajectories, downrange separations, number of measurements and crosstrack motion. One question to be answered in this research is: what effect does the J_2 perturbation have on the observability of an IROD solution? Does including the J_2 perturbation when generating measurements and in the IROD algorithm provide better observability (are the errors smaller) than without the J_2 perturbation in the measurements and IROD algorithm? Woffinden [3] showed that when the relative satellite motion dynamics are linear, taking only line-of-sight angles (LOS) measurements cannot uniquely determine the relative motion of a deputy satellite with respect to a chief vehicle. The motivation here is to include the J_2 perturbation in the relative motion equations to see if it removes the range ambiguity problem. The effect of J_2 on observability/accuracy of the IROD solutions is an important part of this research.

The topic of disambiguity (distinguishing between multiple feasible IROD solutions) is an important and non-trivial problem, but it does not fit into the scope of this research. As will be seen, the crucible of solving the IROD problem is the solution of a set of polynomial equations. With the approach outlined in this research, there are often several feasible roots that satisfy the set of polynomial equations and subsequently provide feasible IROD solutions. Residuals are a useful tool in providing information for disambiguating between which IROD solution is the “best” or most accurate IROD solution (the IROD solution that returns the initial relative states closest to the truth). All of this research is simulated cases where the initial relative states are already known and thus a position error compared to the truth is the most valuable residual for characterizing the accuracy of the IROD algorithm.

In on-board applications, the true initial relative states are not known, so a set of helpful residuals can be used in a process to disambiguate multiple IROD solutions to arrive at the “best” solution. This disambiguation process is grounds for future research and essential when sifting through actual, on-board mission LOS measurements for IROD applications. Possible disambiguation techniques include measurement residuals, hypothesis testing, and Gauss least squares.

Errors in the LOS measurements can come from a variety of sources. Error sources include camera measurement errors, camera bias, camera misalignment and modelling errors. Although measurement error is not a large focus of the enclosed research a handful of relative motion cases have camera errors injected into the LOS measurements and the IROD solutions are compared. A comprehensive study of different kinds of errors associated with IROD problems is also not the focus of this research.

1.3 Objectives

The objectives of this research are:

1. Derive relative satellite motion equations in spherical coordinates with J_2 perturbations
2. Derive LOS relationships based on the coordinate frame used in Objective 1.
3. Derive an angles-only Initial Relative Orbit Determination algorithm with J_2 perturbations
4. Test the IROD algorithm for a range of relative motion cases, characterizing the effect of J_2 perturbations on relative orbit determination problems.

1.4 Dissertation Overview

The organization of the dissertation is outlined as follows. Chapter 2 lays the groundwork of orbital relative motion in Cartesian coordinates, explaining the previous research in this area, providing a derivation of linearized satellite relative motion models, and showcasing a few common relative motion trajectories such as Leader-Follower, Flyby and Football

configurations. Chapter 3 shows a derivation of an IROD algorithm that accounts for the camera offset from the center-of-mass of the observing vehicle. Chapter 4 provides the background orbital relative motion equations in spherical coordinates and includes a derivation of new relative motion models with J_2 perturbations in spherical coordinates. Chapter 5 provides a derivation of an IROD algorithm that includes J_2 perturbations for three LOS observations (six measurements). Chapter 6 augments the previous IROD algorithm by including more than three LOS observations. Chapter 7 provides IROD results for various relative motion trajectories in LEO. Chapter 8 provides LEO IROD results where J_2 effects are removed from the IROD algorithm. Chapter 9 investigates the effects of camera measurement error. Chapter 10 provides IROD results for various relative motion trajectories in GEO. Chapter 11 summarizes the conclusions for this research and outlines some areas of future work.

CHAPTER 2

ORBITAL RELATIVE MOTION

2.1 Satellite Relative Motion Trajectories

A few common satellite relative motion trajectories are used in the body of this research. Since various categories of trajectories are often referenced with different names, this section introduces a consistent nomenclature to benefit both the reader and the organization of the research included.

2.1.1 Chief and Deputy

While the motion of satellites is often visualized in an inertial coordinate frame as shown in Figure 2.1, a rotating coordinate frame is introduced to visualize the motion of one satellite relative to another. The origin of the rotating coordinate frame is located at the inertial position of a reference satellite. As the reference satellite progresses along its orbit, the coordinate frame rotates. The rotating coordinate frame is called a Local-Vertical Local-Horizontal (LVLH) frame since the direction of the i_x axis is in the radial (Local-Vertical) direction and the i_y axis is in the downrange (Local-Horizontal) direction. The i_z axis completes the LVLH coordinate frame by pointing in the cross-track direction or the direction of angular momentum of the reference orbit. For the relative motion cases shown below, the reference satellite is hereafter referred to as the “chief” satellite (red satellite in Figure 2.1) and the second satellite is referred to as the “deputy” vehicle (blue satellite in Figure 2.1).

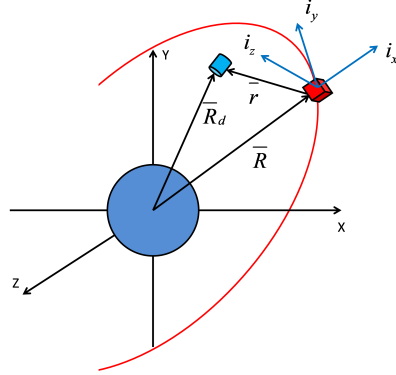


Fig. 2.1: Definition of LVLH coordinate frame

Radial : i_x

Downrange : i_y

Crosstrack : i_z

2.1.2 V-bar Station-keeping

Perhaps the simplest relative motion trajectory is the v-bar station-keeping case [3], where a deputy vehicle appears to remain stationary in the LVLH frame at some fixed position along the downrange axis. This is accomplished when both vehicles are in the same orbit with the only difference being the true anomaly of the each orbit as shown in Figure 2.2. This is also called a Leader-Follower formation and is the simplest formation when considering a satellite formation for communication or scientific missions [14].

2.1.3 Flyby Orbit

A flyby orbit is an orbit where the deputy vehicle appears to *flyby* the chief at some constant radial displacement from the chief vehicle in the LVLH frame [3]. Inertially, the deputy vehicle is in a higher circular orbit so the chief vehicle has a shorter orbital period.

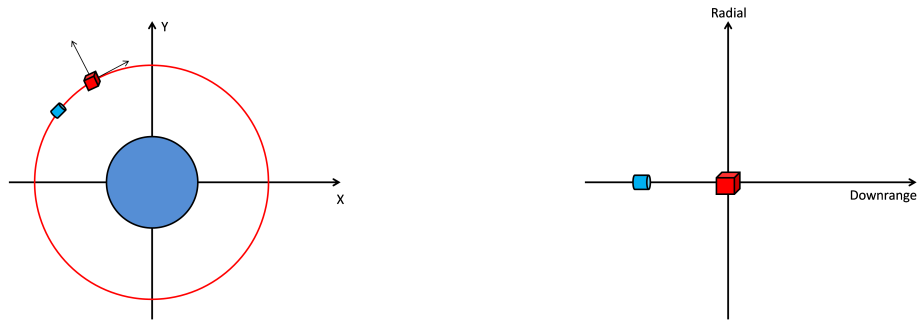


Fig. 2.2: V-bar Station-keeping Left: Inertial Frame. Right: LVLH frame.

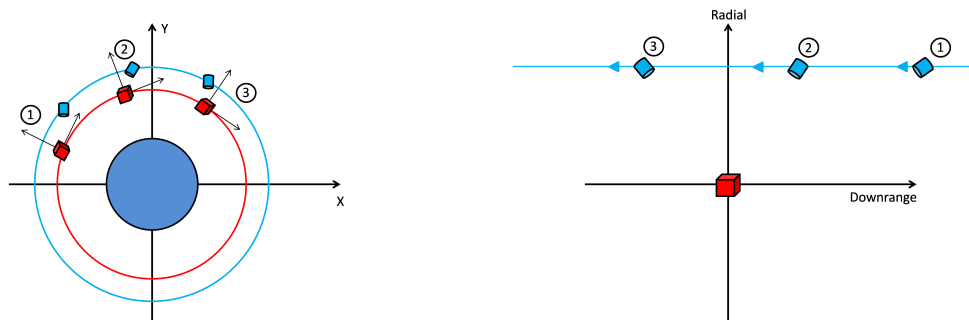


Fig. 2.3: Flyby Orbit. Left: Inertial Frame. Right: LVLH frame.

A flyby orbit is shown in Figure 2.3. A flyby orbit below the chief is achieved when the deputy vehicle is in a smaller circular orbit.

2.1.4 Hopping Orbit

A hopping orbit occurs when both the chief and deputy vehicles share the same periapse or apoapse but not both. The periods of the orbits are different, so the deputy vehicle is drifting either along the positive downrange direction when the deputy period is shorter than the chief period or in the negative downrange direction when the deputy period is longer than the chief period. A hopping orbit [3] where the deputy period is longer is shown in Figure 2.4.

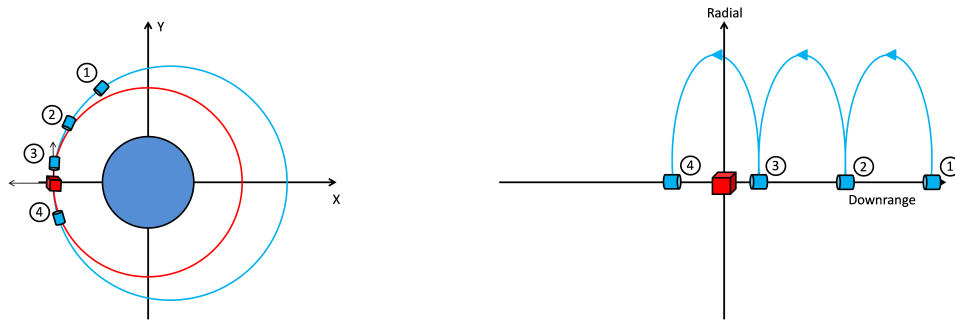


Fig. 2.4: Hopping Orbit Left: Inertial Frame. Right: LVLH frame.

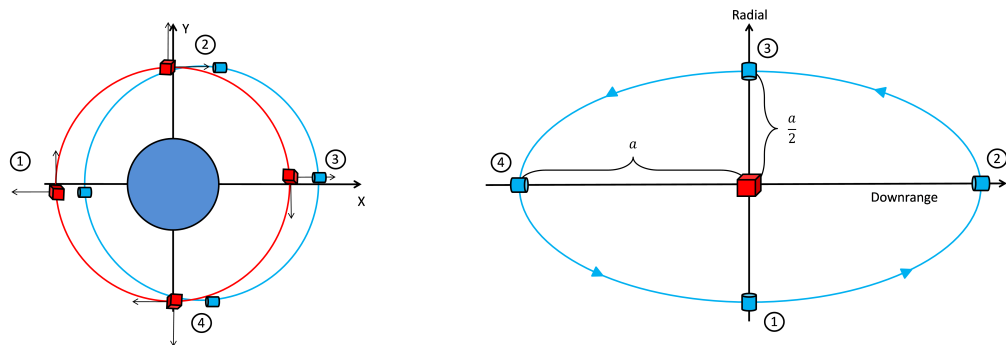


Fig. 2.5: Football Orbit Left: Inertial Frame. Right: LVLH frame.

2.1.5 Football Orbit

A football orbit [3] is formed when both the deputy and chief vehicle have the same orbit period but the deputy vehicle is in a slightly eccentric orbit. If given the proper initial true anomaly, the deputy vehicle circumnavigates the chief vehicle in the LVLH frame, forming a 2×1 ellipse in the radial/downrange plane as shown in Figure 2.5. A football orbit is of particular interest for safety-of-flight concerns. Introducing a small amount of sinusoidal cross-track motion properly phased with a football ellipse will insure that if the deputy vehicle loses power, no amount of drift will cause a collision with the chief vehicle. The football orbit with some cross-track motion is often called a Safety Ellipse for this reason.

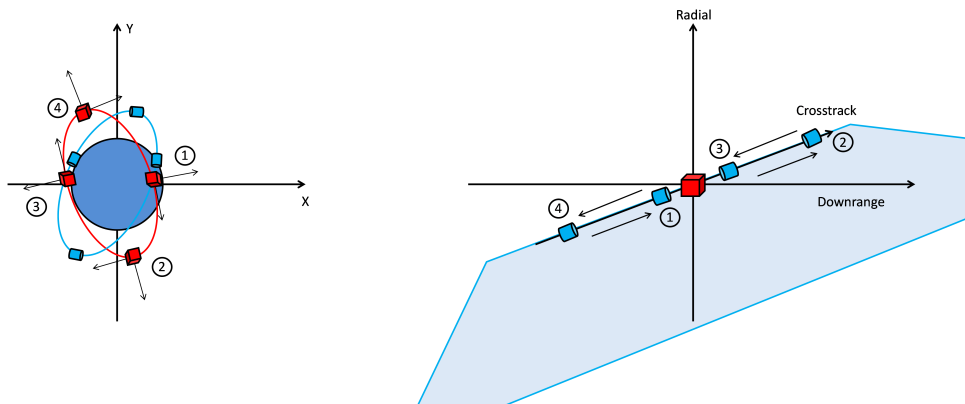


Fig. 2.6: Cross-track Sinusoidal Orbit Left: Inertial Frame. Right: LVLH frame.

2.1.6 Cross-track Sinusoidal Orbit

A sinusoidal cross-track orbit [3] in the LVLH frame occurs when both the deputy and chief vehicle have the same orbital radius but different inclinations. This particular setup results in pure sinusoidal motion in the cross-track direction as shown in Figure 2.6.

2.1.7 Combinations of Relative Motion Trajectories

The above trajectories are only a small number of the relative motion trajectories used in spacecraft navigation applications. These simple examples can be used as building blocks to combine relative motion trajectories.

2.2 Relative Satellite Motion Models

Although the first models for relative satellite motion were derived in the 1960's, relative satellite motion remains an evolving field in astrodynamics [15]. The equations of motion for two spacecraft are nonlinear with no closed-form solution. However, certain assumptions can be made to greatly simplify these equations in order to derive useful relative motion solutions. Mainly, the two satellites are assumed to be in nearly the same orbit. Clohessy and Wiltshire, starting with the nonlinear equations of motion in Cartesian coordinates, linearized the equations of motion about a nominal circular trajectory [1, 16]. The linearization restricts the solution space to small displacements from the circular orbit in

the relative LVLH frame. The linearized differential equations are called the Hill-Clohessy-Wiltshire (HCW) equations and can be written as:

$$\delta\ddot{x} - 3n^2\delta x - 2n\delta\dot{y} = 0 \quad (2.1)$$

$$\delta\ddot{y} + 2n\delta\dot{x} = 0 \quad (2.2)$$

$$\delta\ddot{z} + n^2\delta z = 0 \quad (2.3)$$

When the restriction of a circular chief is relaxed to include elliptical reference orbits, other relative motion solutions can be derived [17–20] the most famous of which are called the Tschauner-Hempel equations. These equations are not limited to circular reference orbits but the linearization still requires that the two spacecraft remain relatively close to one another for the equations to be accurate. The Tschauner-Hempel equations can be written as:

$$\ddot{x} - 2\dot{f}\dot{y} - \left(\dot{f}^2 + 2\frac{\mu}{R(t)^2} \right) x - \ddot{f}y = 0 \quad (2.4)$$

$$\ddot{y} + 2\dot{f}\dot{x} + \ddot{f}x - \left(\dot{f}^2 + \frac{\mu}{R(t)^3} \right) y = 0 \quad (2.5)$$

$$\ddot{z} + \frac{\mu}{R(t)^3} z = 0 \quad (2.6)$$

where f is the true anomaly of the reference orbit, and $R(t)$ is the instantaneous radius of the reference orbit. This solution requires that the problem be regularized, resulting in a solution that does not explicitly include time. Tschauner and Hempel found another formulation of satellite relative motion equations that includes derivatives with respect to eccentric anomaly of the chief satellite [21]. Other paths of research have been pursued to find relative motion solutions for chief satellites in arbitrary eccentric orbits. A complex,

state transition matrix has been developed for the relative motion between two spacecraft on elliptical orbits [15]. A simpler form of the state transition matrix for elliptical orbits has also been developed by using a simpler integral function related to the orbital dynamics [22].

Others have derived satellite relative motion solutions for an elliptical reference orbit using orbital elements. This is accomplished by approximating small differences in position and velocity between the two spacecraft as a linear transformation of small differences in their Keplerian elements [23]. The orbital elements are chosen such that, in the absence of disturbances or control, five will remain constant and the true anomaly will be time varying. The expressions for the positions and velocities are then linearized with respect to the reference orbit and transformed to a local coordinate frame. This process defines a state transition matrix instead of linearizing differential equations and then finding solutions for the linear differential equations. Kelly [24] showed that by making use of a non-orthogonal decomposition of the variational motion with respect to an elliptic reference orbit and the perturbation theory from Brumberg [25], an approach to the rendezvous problem can be derived. The effect of an eccentric reference orbit has been shown to be significant when compared to the linearization of the HCW equations [26].

Other work has been done to derive time-explicit representations of relative motion between elliptical orbits [27]. Still other satellite relative motion equations have been derived by defining a set of orbit element differences relative to a common chief orbit [28].

DeVries [29] showed that if non-dimensional variables are introduced for the relative distance and the true anomaly is used as the independent variable instead of time, a solution for the relative motion of two satellites in eccentric orbits may be developed in terms of the powers of the nominal orbit's eccentricity.

Using an integral introduced by Lawden [30], several relative motion solutions of two nearby points in elliptical orbits have been employed [31].

A few second-order relative motion sets of equations have been developed. London [32] added a second-order correction to the first order relative motion equations using the method of successive approximations (the second-order gravitational terms are retained in

the differential equations of motion). Anthony and Sasaki [33] continued London's work, finding corrections and showing that by retaining quadratic terms in the relative distance, the resulting solution was valid not only for close-in rendezvous applications but also for relatively larger distances. Newman [34] applied the Volterra multi-dimensional convolution theory to the nonlinear relative motion equations which yielded a 2nd-order polynomial relative motion solution. The Volterra kernel series expansion technique uses the Kronecker product to represent a nonlinear system in a bi-linear form. Kernels are then computed from matrix products involving the state transition matrix and other system matrices to finally get the Quadratic Volterra (QV) solution. The QV solution is a second-order solution expressing the instantaneous relative states as linear, quadratic and bi-linear combinations of the initial relative conditions. The solution also introduces secular terms not found in the Cartesian solution of the HCW equations. These equations are derived from the 2nd order expansion of the nonlinear differential equations of relative motion.

Sengupta and Vadali [35] show the effects of eccentricity on the shape and size of relative orbits and corrective schemes to account for the effects of eccentricity are derived.

Gim [36] derived a new geometric method using the relationships between the relative states and the differential orbital elements to obtain the state transition matrix instead of directly solving the complex relative motion differential equations. This geometric method includes the effects caused by the reference orbit eccentricity and J_2 gravitational perturbations. The state transition matrices for both mean elements and osculating elements were derived. This geometric method can also be extended to include effects of other perturbing forces such as higher-order gravitational terms of differential atmospheric drag.

2.3 Derivation of Tschauner-Hempel Equations

This section shows a derivation of the Tschauner-Hempel equations included in [6]. The position vector of a deputy vehicle can be written as

$$\bar{r}_d = \bar{r}_c + \bar{r} = (r_c + x) \hat{i}_r + y \hat{i}_\theta + z \hat{i}_h \quad (2.7)$$

where

$$\begin{aligned}\hat{i}_r &= \frac{\bar{r}}{\|\bar{r}\|} \\ \hat{i}_\theta &= \hat{i}_h \times \hat{i}_r \\ \hat{i}_h &= \frac{\bar{h}}{h}\end{aligned}\tag{2.8}$$

The angular velocity vector of the rotating Hill frame relative to the inertial frame is given by

$$\bar{\omega}_{LVLH/inertial} = \dot{f}\hat{i}_h\tag{2.9}$$

where f is the true anomaly of the chief orbit. Taking a derivative with respect to time in the inertial frame of Eq. 2.7 yields

$$\dot{\bar{r}}_d = \bar{v}_d = (\dot{r}_c + \dot{x})\hat{i}_r + (r_c + x)\dot{\hat{i}}_r + \dot{y}\hat{i}_\theta + y\dot{\hat{i}}_\theta + \dot{z}\hat{i}_h + z\dot{\hat{i}}_h\tag{2.10}$$

where

$$\begin{aligned}\dot{\hat{i}}_r &= \bar{\omega} \times \hat{i}_r = \dot{f}\hat{i}_\theta \\ \dot{\hat{i}}_\theta &= \bar{\omega} \times \hat{i}_\theta = -\dot{f}\hat{i}_r \\ \dot{\hat{i}}_h &= \bar{\omega} \times \hat{i}_h = 0\end{aligned}\tag{2.11}$$

So, Eq. 2.10 becomes

$$\dot{\bar{r}}_d = (\dot{r}_c + \dot{x} - y\dot{f})\hat{i}_r + (\dot{y} + \dot{f}(r_c + x))\hat{i}_\theta + \dot{z}\hat{i}_h\tag{2.12}$$

Taking a second derivative with respect to time yields the following expression for the acceleration of the deputy vehicle

$$\ddot{\vec{r}}_d = \left(\ddot{r}_c + \ddot{x} - 2\dot{y}\dot{f} - \dot{f}^2(r_c + x) - y\ddot{f} \right) \hat{i}_r + \left(\ddot{y} + 2\dot{f}(\dot{r}_c + \dot{x}) + \ddot{f}(r_c + x) - y\dot{f}^2 \right) \hat{i}_\theta + \ddot{z}\hat{i}_h \quad (2.13)$$

The chief orbital angular momentum magnitude can be expressed as follows

$$h = r_c^2 \dot{f} \quad (2.14)$$

taking the derivative with respect to time,

$$\dot{h} = 0 = 2r_c \dot{r}_c \dot{f} + r_c^2 \ddot{f} \quad (2.15)$$

which can be rewritten as

$$\ddot{f} = -\frac{2\dot{r}_c \dot{f}}{r_c} \quad (2.16)$$

The position vector of the chief vehicle can be written as

$$\vec{r}_c = r_c \hat{i}_r \quad (2.17)$$

Taking the derivative with respect to time yields

$$\dot{\vec{r}}_c = \dot{r}_c \hat{i}_r + r_c \dot{f} \hat{i}_\theta \quad (2.18)$$

The second time derivative is

$$\ddot{\vec{r}}_c = \left(\ddot{r} - r_c \dot{f}^2 \right) \hat{i}_r + \left(2\dot{r}_c \dot{f} + r_c \ddot{f} \right) \hat{i}_\theta \quad (2.19)$$

Inserting Eq. 2.16 into the above equation cancels out the term in the \hat{i}_θ direction, leaving the result as

$$\ddot{\vec{r}}_c = \left(\ddot{r} - r_c \dot{f}^2 \right) \hat{i}_r = -\frac{\mu}{r_c^2} \hat{i}_r \quad (2.20)$$

So, $\ddot{r} - r_c \dot{f}^2 = -\frac{\mu}{r_c^2}$ and thus $\ddot{r}_c = r_c \dot{f}^2 - \frac{\mu}{r_c^2} = r_c \dot{f}^2 \left(1 - \frac{r_c}{p}\right)$, where $p = \frac{h^2}{\mu}$ (the semi-latus rectum). Substituting this result into Eq. 2.13 gives

$$\ddot{\vec{r}}_d = \left(\ddot{x} - 2\dot{f} \left(\dot{y} - y \frac{\dot{r}_c}{r_c} \right) - x \dot{f}^2 - \frac{\mu}{r_c^2} \right) \hat{i}_r + \left(\ddot{y} + 2\dot{f} \left(\dot{x} - x \frac{\dot{r}_c}{r_c} \right) - y \dot{f}^2 \right) \hat{i}_\theta + \ddot{z} \hat{i}_h \quad (2.21)$$

Substitute the kinematic acceleration expression in Eq. 2.21 into the orbit equations of motion

$$\ddot{\vec{r}}_d = -\frac{\mu}{r_d^3} \vec{r}_d = -\frac{\mu}{r_d^3} \begin{bmatrix} r_c + x \\ y \\ z \end{bmatrix} \quad (2.22)$$

where $r_d = \sqrt{(r_c + x)^2 + y^2 + z^2}$. Eq. 2.22 is substituted into the left hand side of Eq. 2.21 to get

$$\begin{aligned} \ddot{x} - 2\dot{f} \left(\dot{y} - y \frac{\dot{r}_c}{r_c} \right) - x \dot{f}^2 - \frac{\mu}{r_c^2} &= -\frac{\mu}{r_d^3} (r_c + x) \\ \ddot{y} + 2\dot{f} \left(\dot{x} - x \frac{\dot{r}_c}{r_c} \right) - y \dot{f}^2 &= -\frac{\mu}{r_d^3} y \\ \ddot{z} &= -\frac{\mu}{r_d^3} z \end{aligned} \quad (2.23)$$

These are the exact nonlinear relative equations of motion. The only assumption made was that no disturbances are acting on the chief or deputy satellites (the satellites are moving in Keplerian orbits). These equations are valid for arbitrarily large relative orbits, and the chief orbit may be eccentric. If the relative orbit coordinates x , y , and z are small compared to the chief orbit radius r_c , then Eq. 2.23 can be further simplified. The deputy orbit radius can be rewritten as

$$r_d = r_c \sqrt{1 + 2\frac{x}{r_c} + \frac{x^2 + y^2 + z^2}{r_c^2}} \approx r_c \sqrt{1 + 2\frac{x}{r_c}} \quad (2.24)$$

So now $\frac{\mu}{r_d^3}$ can be rewritten as

$$\frac{\mu}{r_d^3} \approx \frac{\mu}{r_c^3} \left(1 - 3\frac{x}{r_c}\right) \quad (2.25)$$

And $\frac{\mu}{r_c^3}$ can be rewritten as

$$\frac{\mu}{r_c^3} = \frac{h^2}{r_c^4} \frac{1}{1 + e \cos f} = \frac{r_c^4 \dot{f}^2}{r_c^4} \frac{1}{1 + e \cos f} = \frac{\dot{f}^2}{1 + e \cos f} = \frac{r_c \dot{f}^2}{p} \quad (2.26)$$

where the orbit elements are the chief orbital elements. Neglecting higher order terms, the right-hand side of Eq. 2.22 can be simplified as

$$-\frac{\mu}{r_d^3} \begin{bmatrix} r_c + x \\ y \\ z \end{bmatrix} \approx -\frac{\mu}{r_c^3} \left(1 - 3\frac{x}{r_c}\right) \begin{bmatrix} r_c + x \\ y \\ z \end{bmatrix} \approx -\frac{\mu}{r_c^3} \begin{bmatrix} r_c - 2x \\ y \\ z \end{bmatrix} \quad (2.27)$$

Now this equation is substituted into the right-hand side of Eq. 2.23 to get

$$\begin{aligned} \ddot{x} - 2\dot{f} \left(\dot{y} - y \frac{\dot{r}_c}{r_c} \right) - x \dot{f}^2 - \frac{\mu}{r_c^2} &= -\frac{\mu}{r_c^3} (r_c - 2x) \\ \ddot{y} + 2\dot{f} \left(\dot{x} - x \frac{\dot{r}_c}{r_c} \right) - y \dot{f}^2 &= -\frac{\mu}{r_c^3} y \\ \ddot{z} &= -\frac{\mu}{r_c^3} z \end{aligned} \quad (2.28)$$

Using Eq. 2.26, these equations can be rewritten as

$$\begin{aligned} \ddot{x} - 2\dot{f} \left(\dot{y} - y \frac{\dot{r}_c}{r_c} \right) - x \dot{f}^2 \left(1 + 2\frac{r_c}{p}\right) &= 0 \\ \ddot{y} + 2\dot{f} \left(\dot{x} - x \frac{\dot{r}_c}{r_c} \right) - y \dot{f}^2 \left(1 - \frac{r_c}{p}\right) &= 0 \\ \ddot{z} + \frac{r_c}{p} \dot{f}^2 z &= 0 \end{aligned} \quad (2.29)$$

Using Eqs. 2.16 and 2.26, along with the true latitude $\theta = \omega + f$, the general relative equations of motion are rewritten in the common form

$$\begin{aligned}
 \ddot{x} - x \left(\dot{\theta}^2 + 2\frac{\mu}{r_c^3} \right) - 2\dot{\theta}\dot{y} - y\ddot{\theta} &= 0 \\
 \ddot{y} + 2\dot{\theta}\dot{x} - x\ddot{\theta} - y \left(\dot{\theta}^2 - \frac{\mu}{r_c^3} \right) &= 0 \\
 \ddot{z} + \frac{\mu}{r_c^3}z &= 0
 \end{aligned} \tag{2.30}$$

These are the Tschauner-Hempel equations. These equations are valid for arbitrary chief eccentricity but the relative separations between satellites must remain small. If the chief satellite is assumed to be in a circular orbit, the chief orbital radius r_c is constant, and the orbital mean motion n is equal to \dot{f} , the true anomaly rate. The above equations can then be simplified into the Clohessy-Wiltshire Equations.

$$\begin{aligned}
 \ddot{x} - 2n\dot{y} - 3n^2x &= 0 \\
 \ddot{y} + 2n\dot{x} &= 0 \\
 \ddot{z} + n^2z &= 0
 \end{aligned} \tag{2.31}$$

At this point it is useful to review the assumptions that went into the derivation of these HCW equations. These equations are only valid for a circular chief orbit and for small separations of x , y , and z when compared to the chief orbital radius r_c . The Clohessy-Wiltshire differential equations are simple enough that they can be analytically integrated to arrive at a closed-form solution. Also, notice that the cross-track differential equation, z , is just simple harmonic motion in the cross-track direction, uncoupled from the in-plane $x - y$ motion.

CHAPTER 3

INITIAL RELATIVE ORBIT DETERMINATION INCLUDING CAMERA OFFSET

In this chapter, the initial relative orbit determination problem is investigated, in particular, for close-in proximity operations using three or more line-of-sight observations to either the center-of-mass of an object or known object features. The solution to this problem is presented and discussed in the context of the Clohessy-Wiltshire orbital relative motion equations. In previous work, this problem has been shown to be unobservable, but, when the camera offset from the vehicle center-of-mass is considered, the relative position and velocity become observable and an initial relative orbit determination solution can be found in terms of three or more observations. The solution is shown to reduce to a simple linear, algebraic problem. The sensitivity of the solution accuracy to spacecraft separation, camera offset, camera accuracy, and the time-interval between measurements is presented and discussed.

3.1 Problem Formulation

This section outlines the reference frames, vector quantities and the HCW equations used in the formulation of the IROD problem. Figure 3.1 shows a rotating local-vertical local horizontal (LVLH) reference frame co-located with the chief center-of-mass.

The relative position of the deputy center-of-mass with respect to the chief center-of-mass in LVLH coordinates is denoted by $\mathbf{r}(t)$, and the relative velocity of the deputy center-of-mass with respect to the chief center-of-mass with respect to the rotating LVLH frame is denoted by $\mathbf{v}(t)$. Vectors without a subscript are assumed to be coordinatized in LVLH coordinates.

The HCW equations can be written in the form

$$\mathbf{r}(i) = \phi_{rr}(i)\mathbf{r}(0) + \phi_{rv}(i)\mathbf{v}(0) \quad (3.1)$$

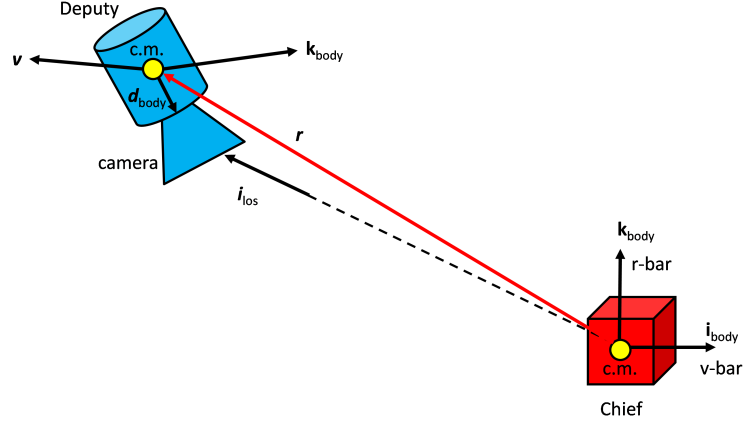


Fig. 3.1: IROD Camera Offset Problem Formulation

$$\mathbf{v}(i) = \phi_{vr}(i)\mathbf{r}(0) + \phi_{vv}(i)\mathbf{v}(0) \quad (3.2)$$

where $\mathbf{r}(0)$, $\mathbf{v}(0)$ are the position and velocity at $t = 0$, $\mathbf{r}(i)$, $\mathbf{v}(i)$ are the position and velocity at time t_i , and $\phi(i)$ is a shorthand notation for $\phi(t_i - t_0)$. The state transition matrix partitions in Eqs. 3.1-3.2 are given by

$$\phi_{rr}(i) = \begin{bmatrix} 1 & 0 & 6 \{ \sin [\omega (\Delta t)] - \omega (\Delta t) \} \\ 0 & \cos [\omega (\Delta t)] & 0 \\ 0 & 0 & 4 - 3 \cos [\omega (\Delta t)] \end{bmatrix} \quad (3.3)$$

$$\phi_{rv}(i) = \begin{bmatrix} \{4 \sin [\omega (\Delta t)] - 3\omega (\Delta t)\} / \omega & 0 & 2 \{ \cos [w (\Delta t)] - 1 \} / \omega \\ 0 & \sin [\omega (\Delta t)] / \omega & 0 \\ 2 \{1 - \cos [\omega (\Delta t)]\} / \omega & 0 & \sin [\omega (\Delta t)] / \omega \end{bmatrix} \quad (3.4)$$

$$\phi_{vr}(i) = \begin{bmatrix} 0 & 0 & 6\omega \{ \cos [\omega (\Delta t)] - 1 \} \\ 0 & -\omega \sin [\omega (\Delta t)] & 0 \\ 0 & 0 & 3\omega \sin [\omega (\Delta t)] \end{bmatrix} \quad (3.5)$$

$$\phi_{vv}(i) = \begin{bmatrix} 4 \cos [\omega (\Delta t)] - 3 & 0 & -2 \sin [\omega (\Delta t)] \\ 0 & \cos [\omega (\Delta t)] & 0 \\ 2 \sin [\omega (\Delta t)] & 0 & \cos [\omega (\Delta t)] \end{bmatrix} \quad (3.6)$$

where $\Delta t = t_i - t_0$ and the axes of the LVLH frame are aligned with the target inertial position vector ($z - axis$), the normal to the target orbit plane ($y - axis$), and the target along-track direction ($x - axis$ in the direction of the “v-bar”, completed the orthogonal set). The angular velocity of the LVLH frame is given by ω rad/s about the y-axis.

It is assumed that the origin of the deputy-fixed reference frame is co-located with the deputy center-of-mass. Without loss of generality it is also assumed that a camera is mounted on the body x-axis at a distance d from the deputy center-of-mass. The camera measurement frame is assumed to be aligned with the focal-plane of the camera, and its orientation with respect to the deputy-fixed frame is assumed to be known and constant.

The pixel location of the chief center-of-mass is used to form a LOS vector from the chief center-of-mass to the camera and is normally expressed in the camera frame at time t_i . However, since the transformation from LVLH to the camera measurement frame at time

t_i is assumed to be known (using knowledge of inertial attitude, position, and velocity), an alternative description of the LOS measurement expressed in the LVLH frame, $i_{los}(i)$, can be utilized.

$$i_{los}(i) = \frac{\mathbf{r}(i) + \mathbf{d}(i)}{\|\mathbf{r}(i) + \mathbf{d}(i)\|} \quad (3.7)$$

where $\mathbf{d}(i) = T_{deputy}^{lvlh}(i)\mathbf{d}^{deputy}$ is the camera center-of-mass offset in the LVLH frame at time t_i , and $\mathbf{d}^{deputy} = \begin{bmatrix} d & 0 & 0 \end{bmatrix}^T$ is the constant position of the camera in the chaser frame. If the initial relative position and velocity of the deputy are $\mathbf{r}(0)$ and $\mathbf{v}(0)$, the LOS time-history in the LVLH frame can be determined by substituting Eqs. 3.1-3.2 into Eq. 3.7

$$i_{los}(i) = \frac{\phi_{rr}(i)\mathbf{r}(0) + \phi_{rv}(i)\mathbf{v}(0) + \mathbf{d}(i)}{\|\phi_{rr}(i)\mathbf{r}(0) + \phi_{rv}(i)\mathbf{v}(0) + \mathbf{d}(i)\|} \quad (3.8)$$

When $\mathbf{d}(i) = \mathbf{0}$, Woffinden and Geller [37] recognized that the above LOS measurement time-history is unchanged when the initial conditions are multiplied by an arbitrary scalar k

$$i_{los}(i) = \frac{\phi_{rr}(i)[k\mathbf{r}(0)] + \phi_{rv}(i)[k\mathbf{v}(0)]}{\|\phi_{rr}(i)[k\mathbf{r}(0)] + \phi_{rv}(i)[k\mathbf{v}(0)]\|} \quad (3.9)$$

and no matter how many measurements of $i_{los}(i)$ are available, the initial conditions cannot be uniquely determined [38].

However, since it is known that the initial conditions are generally observable when $\mathbf{d}(i) \neq \mathbf{0}$ [39], how do we determine the initial position $\mathbf{r}(0)$ and velocity $\mathbf{v}(0)$ in Eq. 3.8 based on three or more LOS observations $i_{los}(i)$, $i = 0, 1, 2, \dots$?

3.2 General Solution to the Initial Relative Orbit Determination Problem

Consider the first LOS observation, $i_{los}(0)$. The solution for the initial position $\hat{\mathbf{r}}(0)$ must satisfy

$$k_0 i_{los}(0) = \hat{\mathbf{r}}(0) + \mathbf{d}(0) \quad (3.10)$$

where k_0 is some unknown scale factor of $i_{los}(0)$. Similarly, for the second and third LOS observations the solution for the initial position and velocity $\hat{\mathbf{r}}(0)$, $\hat{\mathbf{v}}(0)$ must satisfy

$$k_1 i_{los}(1) = \phi_{rr}(1) \hat{\mathbf{r}}(0) + \phi_{rv}(1) \hat{\mathbf{v}}(0) + \mathbf{d}(1) \quad (3.11)$$

$$k_2 i_{los}(2) = \phi_{rr}(2) \hat{\mathbf{r}}(0) + \phi_{rv}(2) \hat{\mathbf{v}}(0) + \mathbf{d}(2) \quad (3.12)$$

where k_1 and k_2 are also unknown scale factors of $i_{los}(1)$ and $i_{los}(2)$, respectively. Solving Eq.3.10 for $\hat{\mathbf{r}}(0)$ produces

$$\hat{\mathbf{r}}(0) = k_0 i_{los}(0) - \mathbf{d}(0) \quad (3.13)$$

and substituting this into Eq. 3.11 and solving for $\hat{\mathbf{v}}(0)$ produces

$$\hat{\mathbf{v}}(0) = \phi_{rv}^{-1}(1) [k_1 i_{los}(1) - \phi_{rr}(1) \{k_0 i_{los}(0) - \mathbf{d}(0)\} - \mathbf{d}(1)] \quad (3.14)$$

Note that the matrix $\phi_{rv}(1)$ is clearly singular when t_1 is an exact integer multiple of one-half the orbital period, but this situation is easily avoided. Now, substituting Eqs. 3.13 and 3.14 back into Eq. 3.12 produces the result

$$\begin{aligned} k_2 i_{los}(2) &= \phi_{rr}(2) \{k_0 i_{los}(0) - \mathbf{d}(0)\} \\ &+ \phi_{rv}(2) \left\{ \phi_{rv}^{-1}(1) [k_1 i_{los}(1) - \phi_{rr}(1) \{k_0 i_{los}(0) - \mathbf{d}(0)\} - \mathbf{d}(1)] \right\} + \mathbf{d}(2) \end{aligned} \quad (3.15)$$

This vector equation represents 3 equations in 3 unknowns, $K = \begin{bmatrix} k_0 & k_1 & k_2 \end{bmatrix}^T$. Rearranging and writing the result in matrix form produces

$$AK = B \quad (3.16)$$

where

$$A = \begin{bmatrix} \{\phi_{rr}(2) - \phi_{rv}(2)\phi_{rv}^{-1}(1)\phi_{rr}(1)\} i_{los}(0) & \phi_{rv}(2)\phi_{rv}^{-1}(1)i_{los}(1) & -i_{los}(2) \end{bmatrix} \quad (3.17)$$

$$B = \left\{ \phi_{rr}(2) - \phi_{rv}(2)\phi_{rv}^{-1}(1)\phi_{rr}(1) \right\} \mathbf{d}(0) + \phi_{rv}(2)\phi_{rv}^{-1}(1)\mathbf{d}(1) - \mathbf{d}(2) \quad (3.18)$$

If A is non-singular, the solutions for the scale factors $\hat{K} = \begin{bmatrix} \hat{k}_0 & \hat{k}_1 & \hat{k}_2 \end{bmatrix}^T$ can be determined from

$$\hat{K} = A^{-1}B \quad (3.19)$$

and unique values for the initial position $\hat{\mathbf{r}}(0)$ and velocity $\hat{\mathbf{v}}(0)$ can be determined from Eqs. 3.13 and 3.14, respectively

$$\hat{x}_0 = \begin{bmatrix} \hat{\mathbf{r}}(0) \\ \hat{\mathbf{v}}(0) \end{bmatrix} = C\hat{K} + D = CA^{-1}B + D \quad (3.20)$$

where

$$C = \begin{bmatrix} i_{los}(0) & 0 & 0 \\ -\phi_{rv}^{-1}(1)\phi_{rr}(1)i_{los}(0) & \phi_{rv}^{-1}(1)i_{los}(1) & 0 \end{bmatrix} \quad (3.21)$$

$$D = - \begin{bmatrix} \mathbf{d}(0) \\ \phi_{rv}^{-1}(1) \{ \mathbf{d}(1) - \phi_{rr}(1)\mathbf{d}(2) \} \end{bmatrix} \quad (3.22)$$

Thus, Eqs. 3.17-3.22 represents a simple algorithm that can be used to determine the solution to the IROD problem based on 3 observations for any relative motion coasting trajectory, and for any known constant or time-varying deputy orientation. Although it has not yet been *proven* that A is non-singular in all cases, the A matrix has been invertible

for all of the numerous numerical tests conducted in this chapter without exception. For the special case of station-keeping on the v-bar with constant attitude and a camera offset in the cross-track direction, the A matrix is shown to always be non-singular [39]. There are special cases when the camera offset does not produce observability and the A matrix is singular, e.g. when the offset is only in the v-bar direction, or when the offset always lies directly between the chief and deputy center-of-masses [39]. In this paper, these special cases have been avoided.

The consequences of A being non-singular deserves further discussion. It has been experimentally verified by numerous examples that when the observations have no error, the A matrix is always invertible (except for the special cases mentioned above) and Eq. 3.19 produces the exact solution to the problem, i.e., a unique trajectory solution can be found (within the context of the HCW equations) given three perfect observations.

When the observations are chosen randomly or when perfect measurements are corrupted by errors, the A matrix is again always found to be invertible. However, these cases occasionally produce negative values for the elements of $\hat{K} = \begin{bmatrix} \hat{k}_0 & \hat{k}_1 & \hat{k}_2 \end{bmatrix}^T$ which have been implicitly assumed to be positive. In these cases, when any $\hat{k}_i < 0$, the solution for the initial position and velocity is incorrect (though A is invertible) and produce a trajectory that passes exactly through the anti-LOS measurement direction. This will be investigated further in future work.

3.2.1 $N > 3$ Observations

When $N > 3$ observations are available during a coasting period, a least squares approach can be taken to determine a solution to the IROD problem. For example, when $N > 3$ the i^{th} observation must satisfy

$$k_i i_{los}(i) = \phi_{rr}(i) \hat{\mathbf{r}}(0) + \phi_{rv}(i) \hat{\mathbf{v}}(0) + \mathbf{d}(i) \quad (3.23)$$

Substituting Eqs. 3.13 and 3.14 into Eq. 3.23 produces

$$\begin{aligned} k_i i_{los}(i) &= \phi_{rr}(i) \{k_0 i_{los}(0) - \mathbf{d}(0)\} \\ &+ \phi_{rv}(i) \left\{ \phi_{rv}^{-1}(1) [k_1 i_{los}(1) - \phi_{rr}(1) \{k_0 i_{los}(0) - \mathbf{d}(0)\} - \mathbf{d}(1)] \right\} + \mathbf{d}(i) \end{aligned} \quad (3.24)$$

This vector equation represents 3 equations in 3 unknowns, k_0 , k_1 , and k_i . Thus the first three observations produce Eq. 3.15, and each additional observation produces a copy of Eq. 3.24. For $N > 3$ observations this results in 3 $(N - 2)$ equations in N unknowns. In matrix form this is written as

$$A_N K_N = B_N \quad (3.25)$$

where

$$A_N = \begin{bmatrix} \Phi(2)i_{los}(0) & \phi_{rv}(2)\phi_{rv}^{-1}(1)i_{los}(1) & -i_{los}(2) & \mathbf{0} & \cdots & \mathbf{0} \\ \Phi(3)i_{los}(0) & \phi_{rv}(3)\phi_{rv}^{-1}(1)i_{los}(1) & \mathbf{0} & -i_{los}(3) & \cdots & \mathbf{0} \\ \vdots & \vdots & \vdots & \vdots & \ddots & \mathbf{0} \\ \Phi(N-1)i_{los}(0) & \phi_{rv}(N-1)\phi_{rv}^{-1}(1)i_{los}(1) & \mathbf{0} & \mathbf{0} & \cdots & -i_{los}(N-1) \end{bmatrix} \quad (3.26)$$

and

$$B_N = \begin{bmatrix} \Phi(2)\mathbf{d}(0) + \phi_{rv}(2)\phi_{rv}^{-1}(1)\mathbf{d}(1) - \mathbf{d}(2) \\ \Phi(3)\mathbf{d}(0) + \phi_{rv}(3)\phi_{rv}^{-1}(1)\mathbf{d}(1) - \mathbf{d}(3) \\ \vdots \\ \Phi(N-1)\mathbf{d}(0) + \phi_{rv}(N-1)\phi_{rv}^{-1}(1)\mathbf{d}(1) - \mathbf{d}(N-1) \end{bmatrix} \quad (3.27)$$

where $\Phi(i) = \phi_{rr}(i) - \phi_{rv}^{-1}(i)\phi_{rv}^{-1}(1)\phi_{rr}(1)$ has been introduced to reduce the size of the

above expressions. When $N > 3$, the least-squares solution to this set of over-determined equation is

$$\hat{K}_N = \left(A_N^T A_N \right)^{-1} A_N^T B_N \quad (3.28)$$

and the solution to the IROD problem, $\hat{\mathbf{r}}(0)$, $\hat{\mathbf{v}}(0)$ is given by

$$\hat{\mathbf{x}}_0 = \begin{bmatrix} \hat{\mathbf{r}}(0) \\ \hat{\mathbf{v}}(0) \end{bmatrix} = C \hat{K} + D \quad (3.29)$$

where $\hat{K} = \begin{bmatrix} \hat{k}_0 & \hat{k}_1 & \hat{k}_2 \end{bmatrix}^T$ contains the first 3 elements of the least-squares solution \hat{K}_N .

3.2.2 Observations of Known Target Features

In many cases, the LOS to the chief center-of-mass i_{los} may be inaccurate or difficult to determine. However, if a LOS to a known target feature can be obtained, the above equations can be reformulated to provide an identical solution to the IROD problem. To simplify the problem, it is assumed that the position of a chief feature relative to the chief center-of-mass r_f^{chief} is in a chief-fixed frame and the orientation of the chief vehicle is known.

The time-history of the LOS to this feature is obtained simple by adding r_f^{chief} to the chief center-of-mass in Eq. 3.8. This gives

$$i_{los_f}(i) = \frac{\phi_{rr}(i)\mathbf{r}(0) + \phi_{rv}(i)\mathbf{v}(0) + \mathbf{d}(i) + T_{chief}^{lvlh}(i)\mathbf{r}_f^{chief}}{\| \phi_{rr}(i)\mathbf{r}(0) + \phi_{rv}(i)\mathbf{v}(0) + \mathbf{d}(i) + T_{chief}^{lvlh}(i)\mathbf{r}_f^{chief} \|} \quad (3.30)$$

A good example of this is the International Space Station (ISS) whose orientation $T_{chief}^{lvlh}(i)$ is known to be aligned near LVLH.

Since it is assumed that r_f^{chief} , \mathbf{d}^{deputy} , $T_{deputy}^{lvlh}(i)$ and $T_{chief}^{lvlh}(i)$ are known quantities, the solution to the IROD problem using a known chief feature is given by the same equations as Eqs. 3.19-3.20 and Eqs. 3.28-3.29 with $T_{deputy}^{lvlh}(i)\mathbf{d}^{deputy}$ replaced by $T_{deputy}^{lvlh}(i)\mathbf{d}^{deputy} + T_{chief}^{lvlh}(i)\mathbf{r}_f^{chief}$. Interestingly, in this case the camera offset \mathbf{d}^{deputy} may be zero while the

feature offset \mathbf{r}_f^{chief} provides the observability that the camera offset would otherwise provide. For the ISS, a large feature offset \mathbf{r}_f^{chief} could provide powerful measurements to an incoming spacecraft, not unlike a navigation beacon.

Finally, if the LOS to a chief feature can be obtained, the possibility of identifying multiple known features is possible. If the orientation of the chief is known, the above equations require only minor modifications. If the orientation of the chief is unknown, the above equations can be augmented with models of the target attitude. This then becomes a pose estimation problem and is beyond the scope of this work.

3.3 Performance Analysis for Leader-Follower Cases with Constant Attitude

In this section it is assumed that the deputy vehicle is in a leader-follower configuration at a fixed distance from the chief vehicle on the v-bar and maintaining a fixed orientation. This is considered a worst case situation since there is no translational or rotational motion to help facilitate a solution to the problem. The key parameters of this problem are camera accuracy, σ_{cam} , camera center-of-mass offset in the deputy frame, \mathbf{d}^{deputy} , the separation between the two vehicles (i.e., the v-bar location of the chaser), \mathbf{R}_0 , and a fixed time-interval between the observations, Δt . It is assumed that the translational motion is governed accurately by CW dynamics since the separation distances are small, e.g. $R_0 \ll 10 \text{ km}$.

The standard deviation of the camera accuracy σ_{cam} is used to represent the effect of all angular errors including deputy attitude uncertainty, chief center-of-mass identification errors, and camera resolution. In the Monte Carlo analysis presented below, random measurement errors ϵ_i with a standard deviation of σ_{cam} are added to the true observations in the form of small random rotations

$$\bar{i}_{los}(i) = (I - [\epsilon_i \times]) i_{los}(i) \quad (3.31)$$

where $[\epsilon_i \times]$ is a skew-symmetric cross-product matrix. The range of values considered for σ_{cam} are varied from realistic values of $\sigma_{cam} = 1 \times 10^{-3}$ rad (200 arc sec) to perhaps an unrealistic value of $\sigma_{cam} = 1 \times 10^{-5}$ rad (2 arc sec). However, this range of measurement

errors is intended to provide the system designer with a larger picture of the overall trends and accuracy needed to meet system requirements. Results for measurement errors on the order of $\sigma_{cam} = 1 \times 10^{-2}$ rad (2000 arc sec) were generally unpredictable for only three observations.

The camera offset is nominally in the cross-track direction normal to the orbit plane, 0 deg from the orbit normal, For comparison, two other camera positions are considered, one in which the camera offset is 45 deg from the orbit normal (i.e., halfway between the orbit normal and the local vertical), and one in which the camera offset is 80 deg from the orbit normal (i.e., 10 deg from the local vertical). When the camera offset is in the direction of the local-vertical, three observations are no longer sufficient to solve the IROD problem since the camera, chaser, and target all lie in one plane. In this situation, a minimum of four observations are required [39].

The magnitude of the camera offset $d = \| \mathbf{d}^{deputy} \|$ and the separation distance $R_0 = \| \mathbf{R}_0 \|$ can conveniently be combined into a single parameter d/R_0 . The accuracy of the IROD solution is dependent only on this ratio rather than the individual values of d and R_0 due to the scalability of the problem, i.e., angles-only measurements and linear dynamics. The range of values considered is $d/R_0 = 0.001$ to $d/R_0 = 0.1$. This encompasses a wide range of practical separation distances and camera offsets.

Finally, the time-interval between observations Δt is perhaps the most important parameter of this problem. Observations separated by large values of Δt may be impractical due to the cumulative effect of unmodeled disturbances or translational maneuvers. Observations separated by small values of Δt may also not be useful due to insufficient evolution of the dynamics. Thus, several values of Δt ranging from 100 sec to 1000 sec are considered.

3.3.1 Three Observations

The accuracy of the IROD solutions based on Eqs. 3.17-3.22 is investigated. Eqs. 3.7 and 3.31 are used to generate measurements, and T_{deputy}^{lvlh} is constant and aligned with LVLH. Monte Carlo analysis is used to determine the standard deviation of the solution errors based on 1000 samples.

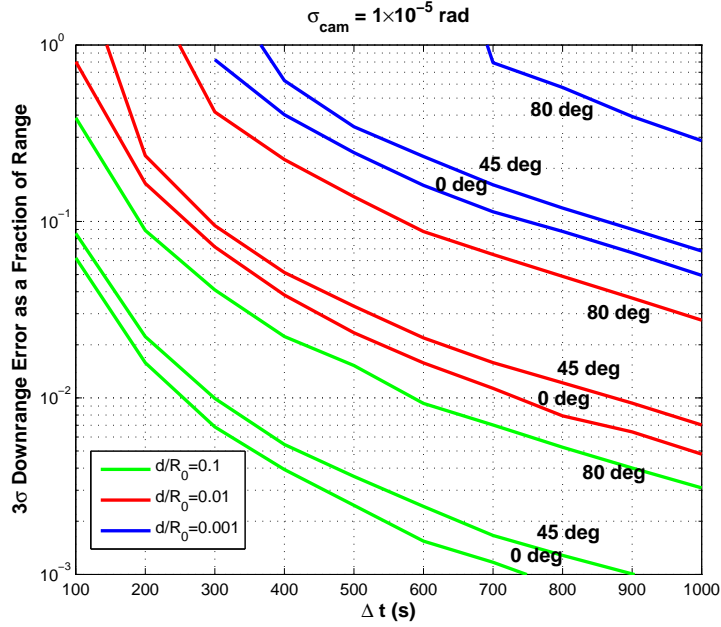


Fig. 3.2: Downrange position error (3σ) based on 1000 Monte Carlo samples as a function of the time-interval between observations and camera offset orientation for $\sigma_{cam} = 1 \times 10^{-5} \text{ rad}$

Figures 3.2-3.4 show the 3σ downrange solution error as a fraction of the range where σ_{cam} is varied from $1 \times 10^{-5} \text{ rad}$ to $1 \times 10^{-3} \text{ rad}$, d/R_0 is varied from 0.001 to 0.1, and Δt is varied from 100 sec to 1000 sec. These figures also show the effect of different orientations of the camera offset.

Several conclusions can be drawn from these figures. First, measurements errors at the milliradian level or better are required to obtain reasonably accurate solutions. A camera offset normal to the orbit plane (i.e., 0 deg from the orbit normal) produces the best performance. When the orientation of the offset is 45 deg from the orbit normal, a minimal reduction in performance is evident, while an orientation 80 deg from the orbit normal results in an order of magnitude reduction in performance.

It is also clear that the solution error is proportional to the measurement error σ_{cam} and inversely proportional to the ratio d/R_0 . For example, the accuracy of the position/velocity solution as a percent of the range when $\sigma_{cam} = 1 \times 10^{-5} \text{ rad}$ and $d/R_0 = 0.001$ (Fig. 3.2) is nearly the same when $\sigma_{cam} = 1 \times 10^{-4} \text{ rad}$ and $d/R_0 = 0.01$ (Fig. 3.3) or when $\sigma_{cam} = 1 \times 10^{-3} \text{ rad}$ and $d/R_0 = 0.1$ (Fig. 3.4).

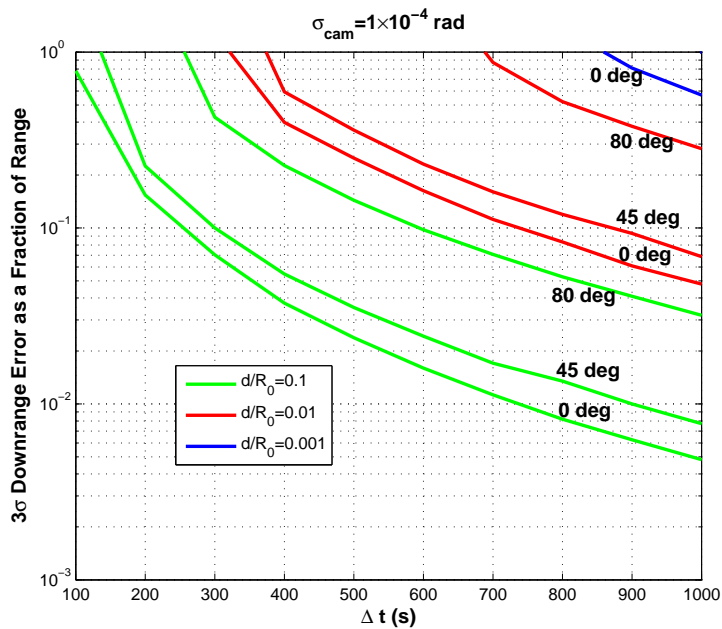


Fig. 3.3: Downrange position error (3σ) based on 1000 Monte Carlo samples as a function of the time-interval between observations and camera offset orientation for $\sigma_{cam} = 1 \times 10^{-4} \text{ rad}$

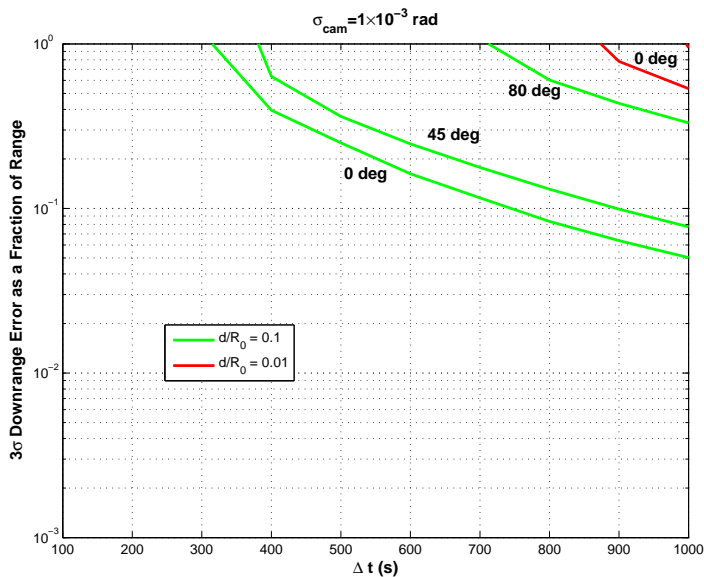


Fig. 3.4: Downrange position error (3σ) based on 1000 Monte Carlo samples as a function of the time-interval between observations and camera offset orientation for $\sigma_{cam} = 1 \times 10^{-3} \text{ rad}$

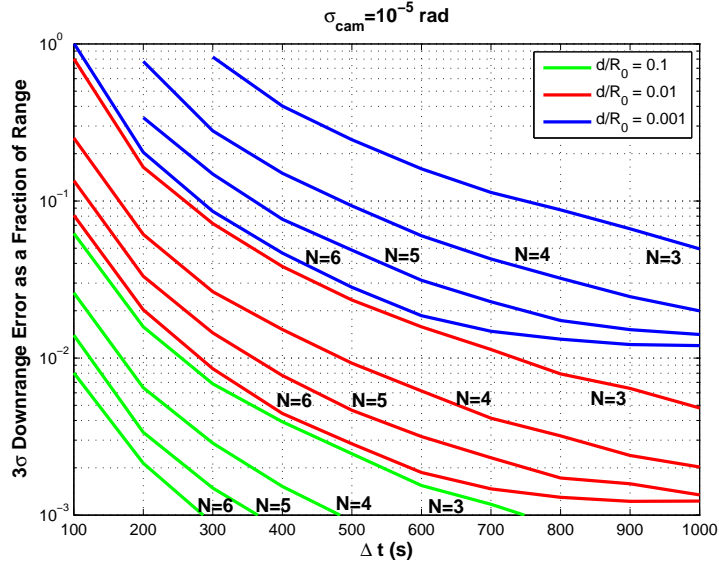


Fig. 3.5: Downrange position error (3σ) based on 1000 Monte Carlo samples as a function of the time-interval between observations and the number of observations ($N = 3, 4, 5,$ and 6) for $\sigma_{cam} = 1 \times 10^{-5} \text{ rad}$

Figures 3.2-3.4 also clearly show how the time interval between measurements significantly affects performance. While larger time-intervals may have the potential to produce more accurate solutions, the additional performance may be difficult to realize due to the cumulative effect of unmodeled disturbances (maneuver execution errors, differential J_2 , drag, solar radiation pressure) on the accuracy of the solution.

3.3.2 More than Three Observations

The accuracy of the IROD problem solutions based on Eq. 3.28 for $N = 3, 4, 5,$ and 6 observations is investigated. Eqs. 3.7 and 3.31 are used to generate measurements, and T_{deputy}^{lvlh} is constant and aligned with LVLH. Monte Carlo analysis is used to determine the standard deviation of the solution errors based on 1000 samples.

Figures 3.5-3.7 show the 3σ downrange error as a fraction of the range for $N = 3, 4, 5,$ and 6 , where σ_{cam} is varied from $1 \times 10^{-5} \text{ rad}$ to $1 \times 10^{-3} \text{ rad}$, d/R_0 is varied from 0.001 to 0.1, and Δt is varied from 100 sec to 1000 sec.

As for three observations, the solution error for $N = 4, 5,$ and 6 is proportional to the

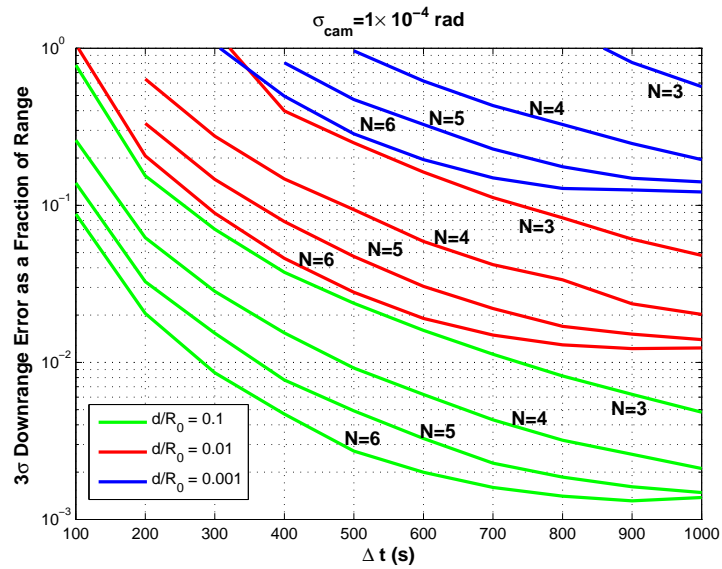


Fig. 3.6: Downrange position error (3σ) based on 1000 Monte Carlo samples as a function of the time-interval between observations and the number of observations ($N = 3, 4, 5,$ and 6) for $\sigma_{cam} = 1 \times 10^{-4} \text{ rad}$

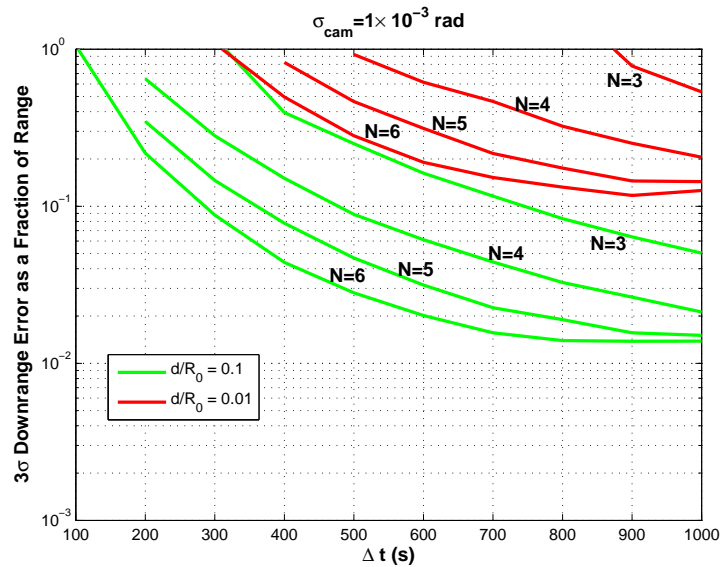


Fig. 3.7: Downrange position error (3σ) based on 1000 Monte Carlo samples as a function of the time-interval between observations and the number of observations ($N = 3, 4, 5,$ and 6) for $\sigma_{cam} = 1 \times 10^{-3} \text{ rad}$

measurement error σ_{cam} and inversely proportional to the ratio d/R_0 . For example, the accuracy of the position/velocity solution when $\sigma_{cam} = 1 \times 10^{-5} rad$ and $d/R_0 = 0.001$ (Fig. 3.5) is nearly the same when $\sigma_{cam} = 1 \times 10^{-4} rad$ and $d/R_0 = 0.01$ (Fig. 3.6), or when $\sigma_{cam} = 1 \times 10^{-3} rad$ and $d/R_0 = 0.1$ (Fig. 3.7).

More importantly, the effect of adding 1, 2, or 3 observations to the original three observations is significant. Figures 3.2-3.4 show a consistent increase in accuracy as the number of observations is increased. For a given ΔT , an increase in the number of observations from 3 to 6 results in over an order of magnitude improvement in the solution accuracy. Unfortunately, this is primarily due to the increase in the time-period over which the 6 observations are taken rather than an increase in the number of observations. When the time-period of interest is held fixed, an increase in the number of observations (and decrease in the measurement time-interval) results in only a small improvement in the solution accuracy.

3.4 Conclusions

Since the angles-only relative navigation problem, within the context of Clohessy-Wiltshire dynamics, is known from previous work to be observable when an offset between the camera and the chaser center-of-mass exists, a solution to the angles-only initial relative orbit determination problem is thus possible when three or more line-of-sight observations are available. This chapter has developed a solution to this problem for close-in proximity operations when three or more line-of-sight observations to either the center-of-mass of an object or known object features are available. The solution takes the form of simple algebraic equations and requires the inversion of one matrix of dimension $3N - 6$ when N is the number of observations.

During v-bar station-keeping, the accuracy of the algorithm is dependent on the ratio of the camera offset to the deputy-chief separation distance, the time-interval between observations, and standard deviation of the measurement errors. Within the context of the Clohessy-Wiltshire equations, the algorithm solutions are exact when the measurement errors are zero. Otherwise, the solution errors are proportional to the measurement error

and inversely proportional to the ratio of the camera-offset to the vehicle-separation distance. The measurement time-interval is also a key parameter in this problem. When the measurement errors are not zero, the observations must be separated by > 100 's of seconds (for LEO) to achieve useful solutions. When more than three observations are available, the above conclusions are unchanged and, as expected, solution accuracy slightly improves.

For all cases examined, the solution accuracy depends on the magnitude of the camera offset or the magnitude of a known target feature offset from the center-of-mass. It has been shown that small offsets < 1 m may be helpful during proximity operations < 100 m range, and large offsets ≈ 50 m associated with large space structures (e.g. the ISS) can extend the relative navigation range to 1000 's of meters, using moderately accurate sensors.

CHAPTER 4

ORBITAL RELATIVE MOTION IN SPHERICAL COORDINATES

In 1963, Stern [40] formulated the Elliptical Cylindrical Coordinate System and showed that the curvilinear system has definite advantages for studying motion along a known, fixed elliptical trajectory. He also noted that in studies involving the dynamic or geometric characteristics associated with a known ellipse, the elliptical cylindrical coordinate system has some advantages. Jones [41] continued Stern's work by developing a state transition matrix for the cylindrical coordinate system derived by Stern. Berreen and Crisp [42] formulated special relative motion equations in curvilinear coordinates for a probe ejecting from a space station and found that by employing curvilinear coordinates, their approximate solution could be used over larger relative displacements than earlier solutions in a rectangular coordinate frame. The derivation of the relative motion equations in a cylindrical coordinate frame has been available for some time [43], though its utility has not been realized until more recent research publications [44]. In Ref. [44], the nonlinear equations of relative orbital motion in a cylindrical frame are presented. These nonlinear equations are linearized about a circular reference orbit resulting in a set of linear time-invariant relative motion differential equations. These equations can be written as

$$\delta\ddot{r} - 3n^2\delta r - 2Rn\delta\dot{\theta} = 0 \quad (4.1)$$

$$\delta\ddot{\theta} + \frac{2n}{R}\delta\dot{r} = 0 \quad (4.2)$$

$$\delta\ddot{z} + n^2\delta z = 0 \quad (4.3)$$

where δr is the relative radial position change, $\delta\theta$ is the relative azimuth angle, and δz is the relative cross-track position change. Although the derivation for these equations is

similar to the derivation for the Cartesian HCW equations, there is a significant difference. Since the nonlinear equations of motion in cylindrical coordinates are not a function of $\delta\theta$ or $\delta\dot{z}$, the above linearized equations are valid for arbitrarily large $\delta\theta$ and $\delta\dot{z}$. This nuance of the linearization process in curvilinear coordinates was noted by Gobetz [45]. This is an important result of the linearization process that provides increased accuracy over the HCW equations for arbitrarily large $\delta\theta$ (downrange separation) and $\delta\dot{z}$ (cross-track velocity).

The method of multiple scales has also been used to derive 2nd-order relative motion equations in spherical coordinates [46]. Multiple scales is a perturbation theory that assumes the solution will be a function of several timescales, each of which is independent of the others. In Ref. [46], the linear, time-invariant equations of relative motion are also derived for spherical coordinate frames. The equations are very similar to the Cartesian HCW form and can be written as

$$\delta\ddot{\rho} - 3n^2\delta\rho - 2nR\delta\dot{\theta} = 0 \quad (4.4)$$

$$\delta\ddot{\theta} + \frac{2n}{R}\delta\dot{\rho} = 0 \quad (4.5)$$

$$\delta\ddot{\phi} + n^2\delta\phi = 0 \quad (4.6)$$

where $\delta\rho$ is the relative radial position change, $\delta\theta$ is the relative azimuth angle, and $\delta\phi$ is the relative elevation angle. The linearization process in spherical coordinates is similar to the linearization assumptions in cylindrical coordinates. Since the nonlinear equations of motion in spherical coordinates are not a function of $\delta\theta$ or $\delta\dot{\phi}$, the above linearized equations are valid for arbitrarily large $\delta\theta$ and $\delta\dot{\phi}$. The solution to these equations is known and is very similar to the corresponding Cartesian solution of the HCW equations.

Schweighart and Sedwick [47] derived a set of linearized relative motion equations with the J_2 geopotential disturbance by performing orbit averaging of the gradient of the J_2 disturbance. Kechichian and Kelly [48] also derived an analytic first order solution

of the J_2 perturbation effects on relative satellite motion in Cartesian coordinates for a spacecraft in a near-circular orbit with small eccentricity and arbitrary inclination. Schaub and Alfriend [49] analytically derived J_2 invariant relative orbits (relative orbits where the effect of J_2 would not cause relative separation over time because the orbits matched in angular drift rate) specifically for spacecraft formations but it also has applications in studying relative satellite motion with J_2 perturbations.

4.1 Relative Satellite Motion Equations with J_2 Perturbations

For the derivation of relative satellite motion equations with J_2 perturbations, the reference orbit must be chosen carefully. When no J_2 perturbations are included, the reference orbit is the chief orbit which results in the relative satellite motion expressions in cylindrical and spherical coordinate frames as shown above in Eqs 4.1-4.6. The equations for J_2 perturbations in a spherical coordinate frame can be written as [6]

$$a_{J_2} = -\frac{3}{4}J_2k_2 [(3 \cos(2\phi) - 1) e_\rho + 2 \sin(2\phi)e_\phi] \quad (4.7)$$

where $k_2 = \frac{\mu}{\rho^2} \left(\frac{r_{eq}}{\rho}\right)^2$ and states that the acceleration due to J_2 perturbations can be written as a function of ϕ , the inclination angle as measured from the equatorial plane. To use this equation for the acceleration due to J_2 perturbations, the reference orbit must be fixed in the equatorial plane. A key difference of this derivation from the previous derivation of relative satellite motion equation in a curvilinear frame is that the reference orbit is not coincident with the chief orbit, but instead is fixed in the equatorial plane of the Earth.

Two satellites in orbit about a central body can be visualized in a spherical coordinate frame as shown in Fig. 4.1. This figure shows two satellites, a chief and deputy satellite that each have inclined orbits. The reference orbit in this figure is fixed in the XY inertial plane of the Earth (the equatorial plane). The subscript c is used for the chief vehicle and the subscript d is used for the deputy vehicle.

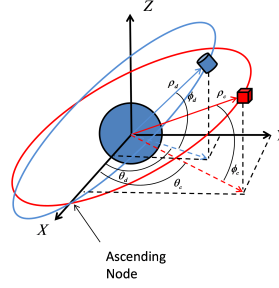


Fig. 4.1: Spherical Coordinate Frame with Two Neighboring Satellites

The position vector of a satellite orbiting the Earth can be written as

$$\bar{r} = \rho e_\rho \quad (4.8)$$

where ρ is the scalar distance from the center of the Earth to the center of mass of the satellite and e_ρ is a direction vector in the current direction of the satellite. Taking the time derivative of this equation yields an equation for the velocity of a satellite orbit the Earth

$$\dot{\bar{r}} = \bar{v} = \dot{\rho} e_\rho + \rho \dot{e}_\rho = \dot{\rho} e_\rho + \rho(\bar{\omega} \times e_\rho) \quad (4.9)$$

where $\dot{\rho}$ is the scalar radial velocity of the satellite and $\bar{\omega}$ can be expressed as

$$\bar{\omega} = \dot{\theta} e_z - \dot{\phi} e_\theta = \dot{\theta} (\cos \phi e_\phi + \sin \phi e_\rho) - \dot{\phi} e_\theta \quad (4.10)$$

Substituting Eq. 4.10 into 4.9 results in a simplified expression for the velocity of a satellite

$$\bar{v} = \dot{\rho} e_\rho + \rho \dot{\theta} \cos \phi e_\theta + \rho \dot{\phi} e_\phi \quad (4.11)$$

Taking the time derivative of this equation yields an expression for the acceleration of an orbiting satellite

$$\dot{\vec{v}} = \vec{a} = \ddot{\rho} e_\rho + \dot{\rho} \dot{e}_\rho + \dot{\rho} \dot{\theta} \cos \phi e_\theta + \rho \ddot{\theta} \cos \phi e_\theta - \rho \dot{\theta} \dot{\phi} \sin \phi e_\theta + \rho \dot{\theta} \cos \phi \dot{e}_\theta + \dot{\rho} \dot{\phi} e_\phi + \rho \ddot{\phi} e_\phi + \rho \dot{\phi} \dot{e}_\phi \quad (4.12)$$

where

$$\begin{aligned} \dot{e}_\rho &= \bar{\omega} \times e_\rho = \dot{\theta} \cos \phi e_\theta + \dot{\phi} e_\phi \\ \dot{e}_\theta &= \bar{\omega} \times e_\theta = -\dot{\theta} \cos \phi e_\rho + \dot{\theta} \sin \phi e_\phi \\ \dot{e}_\phi &= \bar{\omega} \times e_\phi = -\dot{\theta} \sin \phi e_\theta - \dot{\phi} e_\rho \end{aligned} \quad (4.13)$$

Substituting Eq. 4.13 into 4.12 yields

$$\begin{aligned} \vec{a} &= \left(\ddot{\rho} - \rho \dot{\theta}^2 \cos^2 \phi - \rho \dot{\phi}^2 \right) e_\rho \\ &+ \left(2\dot{\rho} \dot{\theta} \cos \phi + \rho \ddot{\theta} \cos \phi - 2\rho \dot{\theta} \dot{\phi} \sin \phi \right) e_\theta + \left(2\dot{\rho} \dot{\phi} + \rho \dot{\theta}^2 \sin \phi \cos \phi + \rho \ddot{\phi} \right) e_\phi \end{aligned} \quad (4.14)$$

The acceleration due to gravity can be written as

$$a_g = -\frac{\mu}{\rho^2} e_\rho \quad (4.15)$$

From Ref. [6], the acceleration due to J_2 perturbations can be written in spherical coordinates as

$$a_{J_2} = -\frac{3}{4} J_2 k_2 [(3 \cos(2\phi) - 1) e_\rho + 2 \sin(2\phi) e_\phi] \quad (4.16)$$

where $k_2 = \frac{\mu}{\rho^2} \left(\frac{r_{eq}}{\rho} \right)^2$.

From Newton's Law, we can equate Eq. 4.15, 4.16 and 4.14 as

$$\begin{aligned}
-\frac{\mu}{\rho^2}e_\rho - \frac{3}{4}J_2\frac{\mu r_{eq}^2}{\rho^4} [(3\cos(2\phi) - 1)e_\rho + 2\sin(2\phi)e_\phi] &= \left(\ddot{\rho} - \rho\dot{\theta}^2 \cos^2 \phi - \rho\dot{\phi}^2\right) e_\rho \quad (4.17) \\
&+ \left(2\dot{\rho}\dot{\theta} \cos \phi + \rho\ddot{\theta} \cos \phi - 2\rho\dot{\phi}\dot{\theta} \sin \phi\right) e_\theta \\
&+ \left(2\dot{\rho}\dot{\phi} + \rho\dot{\theta}^2 \sin \phi \cos \phi + \rho\ddot{\phi}\right) e_\phi
\end{aligned}$$

This equation can be split into the orthogonal components, e_ρ , e_θ , e_ϕ to get

$$\begin{aligned}
e_\rho : \quad \ddot{\rho} &= \rho\dot{\theta}^2 \cos^2 \phi + \rho\dot{\phi}^2 - \frac{\mu}{\rho^2} - \frac{3}{4}J_2\frac{\mu r_{eq}^2}{\rho^4} (3\cos(2\phi) - 1) \\
e_\theta : \quad \ddot{\theta} &= -\frac{2\dot{\rho}\dot{\theta}}{\rho} + 2\dot{\phi}\dot{\theta} \tan \phi \quad (4.18) \\
e_\phi : \quad \ddot{\phi} &= -\frac{2\dot{\rho}\dot{\phi}}{\rho} - \dot{\theta}^2 \sin \phi \cos \phi - \frac{3}{2}J_2\frac{\mu r_{eq}^2}{\rho^5} \sin(2\phi)
\end{aligned}$$

This set of equations can be written with a subscript c to denote the equations of motion of the chief vehicle and with the subscript d to denote the equations of motion of the deputy vehicle:

$$\begin{aligned}
e_{\rho_c} : \quad \ddot{\rho}_c &= \rho_c\dot{\theta}_c^2 \cos^2 \phi_c + \rho_c\dot{\phi}_c^2 - \frac{\mu}{\rho_c^2} - \frac{3}{4}J_2\frac{\mu r_{eq}^2}{\rho_c^4} (3\cos(2\phi_c) - 1) \\
e_{\theta_c} : \quad \ddot{\theta}_c &= -\frac{2\dot{\rho}_c\dot{\theta}_c}{\rho_c} + 2\dot{\phi}_c\dot{\theta}_c \tan \phi_c \quad (4.19) \\
e_{\phi_c} : \quad \ddot{\phi}_c &= -\frac{2\dot{\rho}_c\dot{\phi}_c}{\rho_c} - \dot{\theta}_c^2 \sin \phi_c \cos \phi_c - \frac{3}{2}J_2\frac{\mu r_{eq}^2}{\rho_c^5} \sin(2\phi_c)
\end{aligned}$$

$$\begin{aligned}
e_{\rho_d} : \quad \ddot{\rho}_d &= \rho_d\dot{\theta}_d^2 \cos^2 \phi_d + \rho_d\dot{\phi}_d^2 - \frac{\mu}{\rho_d^2} - \frac{3}{4}J_2\frac{\mu r_{eq}^2}{\rho_d^4} (3\cos(2\phi_d) - 1) \\
e_{\theta_d} : \quad \ddot{\theta}_d &= -\frac{2\dot{\rho}_d\dot{\theta}_d}{\rho_d} + 2\dot{\phi}_d\dot{\theta}_d \tan \phi_d \quad (4.20) \\
e_{\phi_d} : \quad \ddot{\phi}_d &= -\frac{2\dot{\rho}_d\dot{\phi}_d}{\rho_d} - \dot{\theta}_d^2 \sin \phi_d \cos \phi_d - \frac{3}{2}J_2\frac{\mu r_{eq}^2}{\rho_d^5} \sin(2\phi_d)
\end{aligned}$$

We define the spherical deputy states in the same manner as the spherical chief states plus some small deviation.

$$\begin{aligned}
\rho_d &= \rho_c + \delta\rho \\
\theta_d &= \theta_c + \delta\theta \\
\phi_d &= \phi_c + \delta\phi
\end{aligned} \tag{4.21}$$

Taking the second derivative yields

$$\begin{aligned}
\delta\ddot{\rho} &= \ddot{\rho}_d - \ddot{\rho}_c \\
\delta\ddot{\theta} &= \ddot{\theta}_d - \ddot{\theta}_c \\
\delta\ddot{\phi} &= \ddot{\phi}_d - \ddot{\phi}_c
\end{aligned} \tag{4.22}$$

These relationships are substituted into Eqs. 4.20 to yield

$$\begin{aligned}
\delta\ddot{\rho} &= (\rho_c + \delta\rho) \left(\dot{\theta}_c + \delta\dot{\theta} \right)^2 \cos^2(\phi_c + \delta\phi) + (\rho_c + \delta\rho) \left(\dot{\phi}_c + \delta\dot{\phi} \right)^2 \\
&\quad - \frac{\mu}{(\rho_c + \delta\rho)^2} - \frac{3}{4} J_2 \frac{\mu r_{eq}^2}{(\rho_c + \delta\rho)^4} (3 \cos(2(\phi_c + \delta\phi)) - 1) \\
&\quad - \rho_c \dot{\theta}_c^2 \cos^2 \phi_c - \rho_c \dot{\phi}_c^2 + \frac{\mu}{\rho_c^2} + \frac{3}{4} J_2 \frac{\mu r_{eq}^2}{\rho_c^4} (3 \cos(2\phi_c) - 1)
\end{aligned} \tag{4.23}$$

$$\begin{aligned}
\delta\ddot{\theta} &= -\frac{2(\dot{\rho}_c + \delta\dot{\rho}) \left(\dot{\theta}_c + \delta\dot{\theta} \right)}{(\rho_c + \delta\rho)} + 2 \left(\dot{\phi}_c + \delta\dot{\phi} \right) \left(\dot{\theta}_c + \delta\dot{\theta} \right) \tan(\phi_c + \delta\phi) \\
&\quad + \frac{2\dot{\rho}_c \dot{\theta}_c}{\rho_c} - 2\dot{\phi}_c \dot{\theta}_c \tan \phi_c
\end{aligned} \tag{4.24}$$

$$\begin{aligned}
\delta\ddot{\phi} &= -\frac{2(\dot{\rho}_c + \delta\dot{\rho}) \left(\dot{\phi}_c + \delta\dot{\phi} \right)}{\rho_c + \delta\rho} - \left(\dot{\theta}_c + \delta\dot{\theta} \right)^2 \sin(\phi_c + \delta\phi) \cos(\phi_c + \delta\phi) \\
&\quad - \frac{3}{2} J_2 \frac{\mu r_{eq}^2}{(\rho_c + \delta\rho)^5} \sin(2(\phi_c + \delta\phi)) + \frac{2\dot{\rho}_c \dot{\phi}_c}{\rho_c} + \dot{\theta}_c^2 \sin \phi_c \cos \phi_c + \frac{3}{2} J_2 \frac{\mu r_{eq}^2}{\rho_c^5} \sin(2\phi_c)
\end{aligned} \tag{4.25}$$

These are the exact nonlinear two-body with J_2 perturbation equations of relative orbital motion in spherical coordinates. The coordinates of the chief are assumed to be known. From these equations it is evident that the dynamics are independent of the relative azimuth angle since it does not appear in that equation. These equations are valid for arbitrary chief eccentricity. There is a singularity in these equations when the inclination of the satellite approaches a polar orbit (as $\phi \rightarrow 90^\circ$). This is a remnant of writing the equations of motion in the spherical coordinate frame.

4.2 Linearized Equations of Motion with J_2

Next, the above equations are linearized about a reference orbit. Certain linearizing assumptions are made to arrive at a set of linearized relative orbital motion equations that include J_2 perturbations. Similar to the HCW cylindrical/spherical set of linearized equations, since $\delta\theta$ does not appear anywhere in the above set of nonlinear equations, the relative azimuth angle, $\delta\theta$, can be arbitrarily large. One difference between previous linearization processes is that now $\delta\dot{\phi}$ does appear in the above set of nonlinear equations so now the relative elevation angle rate must be assumed to be small to first order. The nonlinear equations of motion for a deputy vehicle in Eq. 4.20 can be written in the form

$$\dot{\mathbf{x}} = \mathbf{f}(\mathbf{x}) \tag{4.26}$$

where

$$\mathbf{f}(\mathbf{x}) = \begin{bmatrix} \dot{\rho}_d \\ \dot{\theta}_d \\ \dot{\phi}_d \\ \ddot{\rho}_d \\ \ddot{\theta}_d \\ \ddot{\phi}_d \end{bmatrix} \quad (4.27)$$

and the first-order Taylor Series expansion of Eq. 4.26 can be written as

$$\dot{\mathbf{X}} = \left. \frac{\partial \mathbf{f}}{\partial \mathbf{x}} \right|_{chief} \mathbf{X} \quad (4.28)$$

where

$$\frac{\partial \mathbf{f}}{\partial \mathbf{x}} = \nabla \mathbf{f}(\mathbf{x}) = \begin{bmatrix} \frac{\partial \mathbf{f}}{\partial \rho} & \frac{\partial \mathbf{f}}{\partial \theta} & \frac{\partial \mathbf{f}}{\partial \phi} & \frac{\partial \mathbf{f}}{\partial \dot{\rho}} & \frac{\partial \mathbf{f}}{\partial \dot{\theta}} & \frac{\partial \mathbf{f}}{\partial \dot{\phi}} \end{bmatrix} \quad (4.29)$$

where

$$\frac{\partial \mathbf{f}}{\partial \rho} = \begin{bmatrix} 0 \\ 0 \\ 0 \\ \frac{2\mu}{\rho^3} + \dot{\theta}^2 \cos^2 \phi + \dot{\phi}^2 + \frac{3J_2\mu R_{eq}^2(6 \cos^2 \phi - 4)}{\rho^5} \\ \frac{2\dot{\rho}\dot{\theta}}{\rho^2} \\ \frac{4\dot{\rho}\dot{\phi}^4 + 15J_2\mu R_{eq}^2 \sin 2\phi}{2\rho^6} \end{bmatrix}, \quad \frac{\partial \mathbf{f}}{\partial \theta} = \begin{bmatrix} 0 \\ 0 \\ 0 \\ 0 \\ 0 \\ 0 \end{bmatrix} \quad (4.30)$$

$$\frac{\partial \mathbf{f}}{\partial \phi} = \begin{bmatrix} 0 \\ 0 \\ 0 \\ -\frac{\sin 2\phi(\dot{\theta}^2 \rho^5 - \frac{9}{2} J_2 \mu R_{eq}^2)}{\rho^4} \\ 2\dot{\phi}\dot{\theta}(\tan^2 \phi + 1) \\ -\frac{\cos 2\phi(\dot{\theta}^2 \rho^5 + 3J_2 \mu R_{eq}^2)}{\rho^5} \end{bmatrix}, \quad \frac{\partial \mathbf{f}}{\partial \dot{\rho}} = \begin{bmatrix} 1 \\ 0 \\ 0 \\ 0 \\ -\frac{2\dot{\theta}}{\rho} \\ -\frac{2\dot{\phi}}{\rho} \end{bmatrix} \quad (4.31)$$

$$\frac{\partial \mathbf{f}}{\partial \dot{\theta}} = \begin{bmatrix} 0 \\ 1 \\ 0 \\ 2\dot{\theta}\rho \cos^2 \phi \\ -\frac{2\dot{\rho}}{\rho} + 2\dot{\phi} \tan \phi \\ -\dot{\theta} \sin 2\phi \end{bmatrix}, \quad \frac{\partial \mathbf{f}}{\partial \dot{\phi}} = \begin{bmatrix} 0 \\ 0 \\ 1 \\ 2\dot{\phi}\rho \\ 2\dot{\theta} \tan \phi \\ -\frac{2\dot{\rho}}{\rho} \end{bmatrix} \quad (4.32)$$

These partial derivatives are evaluated for the chief states. Eqs. 4.30-4.32 form a 6x6 Jacobian matrix that is a function of the instantaneous inertial states of the chief vehicle. This Jacobian can be multiplied by the relative position and velocity of the deputy vehicle with respect to the chief vehicle to arrive at Eq. 4.28. To implement these equations in the IROD algorithm, it is assumed that the instantaneous inertial states of the chief vehicle are known. The Jacobian is also used to write a differential equation for a state transition matrix, Φ ,

$$\dot{\Phi} = F\Phi, \quad \Phi(0) = I \quad (4.33)$$

where $F = \frac{\partial \mathbf{f}}{\partial \mathbf{x}}|_{chief}$ is the Jacobian matrix from above and the initial condition of the state transition matrix is identity. The exact, nonlinear differential equations for the chief, along with the differential equations for the state transition matrix, are numerically integrated using a Runge-Kutta integrator to arrive at solutions for the relative position and velocity states, i.e., $\mathbf{X}(t) = \Phi \mathbf{X}_0$.

These are linearized relative motion equations with J_2 that are implemented in the IROD algorithm. These equations closely approximate the nonlinear motion of a satellite with J_2 perturbations except at higher inclinations because the same singularity at $\phi = 90^\circ$ occurs in these linearized equations.

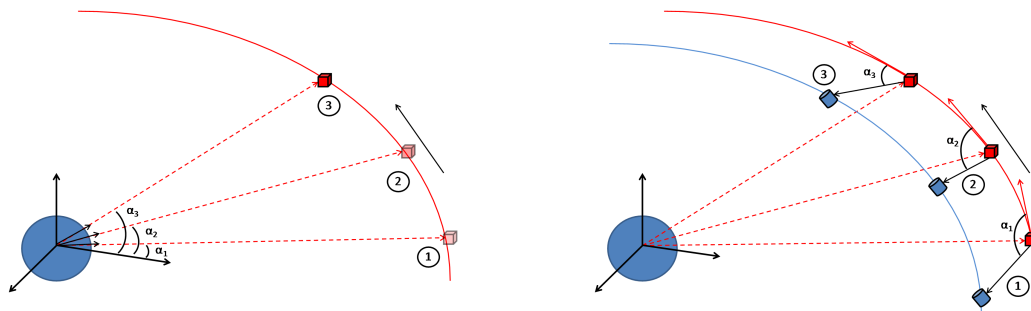
CHAPTER 5

INITIAL RELATIVE ORBIT DETERMINATION PROBLEM, $N = 3$ OBSERVATIONS**5.1 Initial Orbit Determination**

Orbit determination is the art of processing measurements to determine the orbit of a celestial body or orbiting satellite. The techniques of orbit determination go back hundreds of years. Johannes Kepler used available line-of-sight angle measurements of Mars to determine its elliptical orbit. Orbit determination was used by early astronomers to map the solar system and derive the planetary laws of motion. Orbit determination techniques also exist to determine the orbits of satellites around Earth. Orbit determination is also an important part of space situational awareness. Identification of orbital debris is the first step in any debris removal mission [50]. Knowing the orbits of spacecraft assets and neighboring orbital debris is essential for propagating trajectories forward to determine probability of collisions. Initial Orbit Determination (IOD) schemes often require earth-based observations, an initial guess, and an iterative solution whose convergence criteria require a human in the loop.

5.2 Initial Relative Orbit Determination

An alternative to initial orbit determination from observations on Earth is initial *relative* orbit determination (IROD) which can be employed by a neighboring satellite, does not require an initial guess and does not require an iterative solution. If a satellite asset has a camera on-board, it can take LOS measurements of unknown orbital debris objects to determine the relative position and relative velocity of the unknown orbital debris object. The satellite asset can then use its knowledge of its own orbital states to determine the inertial position and velocity states of the orbital debris object and repeat this process for any neighboring debris object, thus identifying and characterizing the orbits of many un-



(a) Gauss' Initial Orbit Determination problem. Three line-of-sight measurements are required to uniquely determine the position and velocity of an orbiting satellite.

(b) Initial Relative Orbit Determination Problem. Three relative line-of-sight measurements are required to uniquely determine the relative position and velocity of a neighboring satellite.

known and potentially hazardous debris objects. Figure 5.1a shows the basic setup for an initial orbit determination problem of an orbiting satellite where measurements are taken from Earth. Figure 5.1b shows the basic setup for an initial relative orbit determination problem where a neighboring satellite is making observations of another satellite.

Gauss' initial orbit determination problem is well known and determines the position and velocity of an orbiting body using only angle measurements [51]. By taking elevation and azimuth angle measurements, i.e. LOS measurements of an orbiting body, an observer can determine the orbit of the body. For a solution to Gauss' problem, at least 3 observations (6 angle measurements) are required to determine the position and velocity uniquely.

The initial relative orbit determination problem is solved in a similar way, however, Woffinden [3] showed that using Hill-Clohessey-Wiltshire (HCW) dynamics to represent the relative motion of two satellites, no number of LOS measurements will uniquely determine the relative states of a neighboring satellite. In other words, relative orbits whose state histories differ only by a scalar multiple, possess the same LOS history. The unique relative states cannot be determined if the following conditions are satisfied:

- Linearized Relative Dynamics
- No thrusting maneuvers

- LOS measurements only (no range information)
- No Camera Offset from the Center of Mass
- LOS measurements can be written in a homogeneous form ($A\mathbf{X}_0 = 0$)
- No other perturbing forces are included

However, using angle measurements, the relative states can be determined with some special considerations. These considerations include taking into account the camera offset of the deputy vehicle when observing the chief vehicle [13] or using higher-order dynamics to model the relative motion [52].

IROD algorithms have been developed using the 2nd-order Quadratic Volterra (QV) solution [52]. This IROD algorithm makes use of Macaulay resultant expressions to solve n polynomial equations in the IROD algorithm [53]. This IROD algorithm is mathematically intensive since the solution to n polynomial equations is not trivial.

Other research has investigated using the relative satellite motion equations in spherical coordinates to formulate an approximate IROD algorithm [12]. Although any IROD algorithm will not exactly determine the relative states of a satellite, the estimate can be used to initialize a Kalman filter where, with more measurements, the estimation errors will decrease.

5.3 Line-Of-Sight Measurements

The advantages of using line-of-sight (LOS) angle measurements from a chief vehicle to a target vehicle have been realized since the early 1960's [54]. Weight and power requirements may exclude other radar or range measurements devices from being implemented on-board. Cameras, from which LOS measurements can be extracted are relatively cheap, light and do not require a lot of power for use. Also, when security or discretion are required for certain missions, LOS measurements are not invasive as opposed to LIDAR measurements where the observed vehicle is splashed with a low-level laser. Since LOS

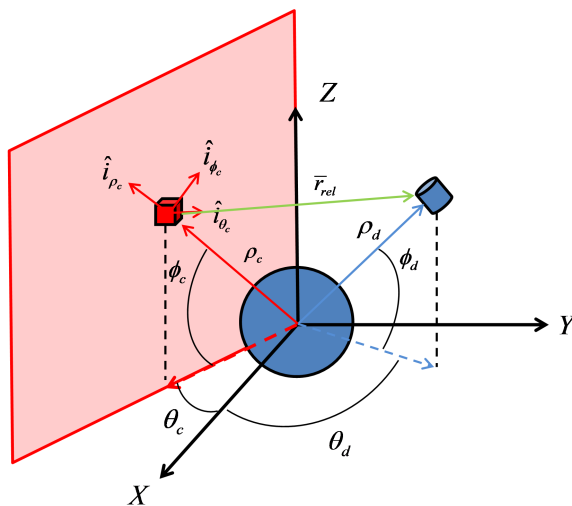


Fig. 5.1: Line-Of-Sight in Spherical Coordinates for an Arbitrary Chief Inclination

measurements are so simple, they have also been proposed as a useful backup navigation tool in the event that the primary guidance system fails.

5.4 Derivation of LOS Measurement Equations

The following section outlines the derivation of the second-order measurement equations that are implemented in a newly derived IROD solution. First, the measurement equations are derived from the exact relative LOS relationships of a chief and deputy vehicle. Then, these nonlinear relationships are expanded to second order using a Taylor Series expansion. Two satellites in orbit about a central body can be visualized in a spherical coordinate frame as shown in Figure 5.1.

Since the chief orbit is not defined as being in the X-Y inertial plane, some care has to be taken when deriving the angle measurement equations. Figure 5.1 shows how first an intermediate coordinate system is defined. This coordinate system is defined by the position

vector of the chief vehicle and the inertial z -axis. The unit position vectors of the chief in this intermediate coordinate system can be written as

$$\hat{i}_{\rho_c} = \begin{bmatrix} \cos \phi_c \\ 0 \\ \sin \phi_c \end{bmatrix}, \quad \hat{i}_{\theta_c} = \begin{bmatrix} 0 \\ 1 \\ 0 \end{bmatrix}, \quad \hat{i}_{\phi_c} = \begin{bmatrix} -\sin \phi_c \\ 0 \\ \cos \phi_c \end{bmatrix} \quad (5.1)$$

The unit position vector of the deputy, \hat{i}_{ρ_d} can be written as

$$\hat{i}_{\rho_d} = \begin{bmatrix} \cos \phi_d \cos \delta\theta \\ \cos \phi_d \sin \delta\theta \\ \sin \phi_d \end{bmatrix} = \begin{bmatrix} \cos (\phi_c + \delta\phi) \cos \delta\theta \\ \cos (\phi_c + \delta\phi) \sin \delta\theta \\ \sin (\phi_c + \delta\phi) \end{bmatrix} \quad (5.2)$$

The relative position vector, \bar{r}_{rel} , can be written as

$$\bar{r}_{rel} = (\rho_c + \delta\rho) \hat{i}_{\rho_d} - \rho_c \hat{i}_{\rho_c} \quad (5.3)$$

Now, the azimuth angle, α , and the elevation angle, β , are defined as

$$\tan \alpha = \frac{\bar{r}_{rel} \cdot \hat{i}_{\rho_c}}{\bar{r}_{rel} \cdot \hat{i}_{\theta_c}} \quad (5.4)$$

$$\tan \beta = \frac{\bar{r}_{rel} \cdot \hat{i}_{\phi_c}}{\bar{r}_{rel} \cdot \hat{i}_{\theta_c}} \quad (5.5)$$

where

$$\begin{aligned} \bar{r}_{rel} \cdot \hat{i}_{\rho_c} &= (\rho_c + \delta\rho) \hat{i}_{\rho_d} \cdot \hat{i}_{\rho_c} - \rho_c \\ &= (\rho_c + \delta\rho) [\cos \phi_c \cos (\phi_c + \delta\phi) \cos \delta\theta + \sin \phi_c \sin (\phi_c + \delta\phi)] - \rho_c \end{aligned} \quad (5.6)$$

$$\bar{r}_{rel} \cdot \hat{i}_{\theta_c} = (\rho_c + \delta\rho) \hat{i}_{\rho_d} \cdot \hat{i}_{\theta_c} = (\rho_c + \delta\rho) \cos(\phi_c + \delta\phi) \sin \delta\theta \quad (5.7)$$

$$\bar{r}_{rel} \cdot \hat{i}_{\phi_c} = (\rho_c + \delta\rho) \hat{i}_{\rho_d} \cdot \hat{i}_{\phi_c} = (\rho_c + \delta\rho) [\cos \phi_c \sin(\phi_c + \delta\phi) - \sin \phi_c \cos(\phi_c + \delta\phi) \cos \delta\theta] \quad (5.8)$$

Then, the in-plane azimuth angle measurement, $\tan \alpha$, is written as

$$\tan \alpha = \frac{\bar{r}_{rel} \cdot \hat{i}_{\rho_c}}{\bar{r}_{rel} \cdot \hat{i}_{\theta_c}} = \frac{(\rho_c + \delta\rho) [\cos \phi_c \cos(\phi_c + \delta\phi) \cos \delta\theta + \sin \phi_c \sin(\phi_c + \delta\phi)] - \rho_c}{(\rho_c + \delta\rho) \cos(\phi_c + \delta\phi) \sin \delta\theta} \quad (5.9)$$

The out-of-plane elevation angle measurement, $\tan \beta$, is given by

$$\tan \beta = \frac{\bar{r}_{rel} \cdot \hat{i}_{\phi_c}}{\bar{r}_{rel} \cdot \hat{i}_{\theta_c}} = \frac{(\rho_c + \delta\rho) [\cos \phi_c \sin(\phi_c + \delta\phi) - \sin \phi_c \cos(\phi_c + \delta\phi) \cos \delta\theta]}{(\rho_c + \delta\rho) \cos(\phi_c + \delta\phi) \sin \delta\theta} \quad (5.10)$$

and Eq. 5.10 can be simplified

$$\tan \beta = \frac{[\cos \phi_c \sin(\phi_c + \delta\phi) - \sin \phi_c \cos(\phi_c + \delta\phi) \cos \delta\theta]}{\cos(\phi_c + \delta\phi) \sin \delta\theta} \quad (5.11)$$

The state $\mathbf{X}(t)$ can be written in two different ways. One is in the traditional spherical, ρ, θ, ϕ coordinates

$$\mathbf{X}(t) = \begin{bmatrix} \delta\rho(t) \\ \delta\theta(t) \\ \delta\phi(t) \\ \delta\dot{\rho}(t) \\ \delta\dot{\theta}(t) \\ \delta\dot{\phi}(t) \end{bmatrix} \quad (5.12)$$

or the state vector can be written using arc-lengths in the azimuth, $\delta\hat{y}$ and elevation, $\delta\hat{z}$ directions

$$\mathbf{X}_{\rho\hat{y}\hat{z}}(t) = \begin{bmatrix} \delta\rho(t) \\ \delta\hat{y} \\ \delta\hat{z} \\ \delta\dot{\rho}(t) \\ \delta\dot{\hat{y}} \\ \delta\dot{\hat{z}} \end{bmatrix} = \begin{bmatrix} 1 & & & & & \\ & a_c & & & & \\ & & a_c & & & \\ & & & 1 & & \\ & & & & a_c & \\ & & & & & a_c \end{bmatrix} \begin{bmatrix} \delta\rho(t) \\ \delta\theta(t) \\ \delta\phi(t) \\ \delta\dot{\rho}(t) \\ \delta\dot{\theta}(t) \\ \delta\dot{\phi}(t) \end{bmatrix} = T^{-1}\mathbf{X}(t) \quad (5.13)$$

where a_c is the semi-major axis of the chief vehicle. This new state vector is constructed with consistent units (all of the units are in meters and meters/second) for better numerical accuracy and stability.

5.4.1 First-Order Measurement Equation Expansion

The numerator and denominator of Eqs. 5.9 and 5.11 can be expanded to first-order about $\delta\rho = 0$, $\delta\theta = 0$ and $\delta\phi = 0$. The first order expansions of the azimuth and elevation equations are

$$\delta\rho - \rho_c \delta\theta \cos \phi_c \tan \alpha \approx 0 \quad (5.14)$$

$$\delta\phi - \delta\theta \cos \phi_c \tan \beta \approx 0 \quad (5.15)$$

5.4.2 Second-Order Measurement Equation Expansion

The numerator and denominator of Eqs. 5.9 and 5.11 can be expanded to second-order about $\delta\rho = 0$, $\delta\theta = 0$ and $\delta\phi = 0$. The second order expansions of the azimuth and elevation equations are

$$\begin{aligned} \delta\rho - \frac{\rho_c}{2} \delta\phi^2 - \frac{\rho_c}{2} \cos^2 \phi_c \delta\theta^2 \\ - \delta\theta \tan \alpha (\cos \phi_c \delta\rho + \rho_c \cos \phi_c - \rho_c \sin \phi_c \delta\phi) \approx 0 \end{aligned} \quad (5.16)$$

$$\frac{\sin \phi_c \cos \phi_c}{2} \delta\theta^2 - \tan \beta (\cos \phi_c - \delta\phi \sin \phi_c) \delta\theta + \delta\phi \approx 0 \quad (5.17)$$

Eqs. 5.14 and 5.15 can be rewritten using the relationships $\delta\rho = \Phi_\rho(t_i)\mathbf{X}_0$, $\delta\theta = \Phi_\theta(t_i)\mathbf{X}_0$ and $\delta\phi = \Phi_\phi(t_i)\mathbf{X}_0$

$$(\Phi_\rho(t_i) - \rho_c \cos \phi_c \tan \alpha \Phi_\theta(t_i)) \mathbf{X}_0 \approx 0 \quad (5.18)$$

$$[-\tan \beta \cos \phi_c \Phi_\theta(t_i) + \Phi_\phi(t_i)] \mathbf{X}_0 \approx 0 \quad (5.19)$$

Now, Eqs.5.18 and 5.19 can be rewritten in a more compact form

$$b_i^\alpha \mathbf{X}_0 \approx 0, \quad b_i^\beta \mathbf{X}_0 \approx 0 \quad i = 0, 1, 2 \quad (5.20)$$

or using Eq. 5.13 the compact form can be written as

$$b_i^\alpha T \mathbf{X}_{\rho \hat{y} \hat{z}} \approx 0 \quad b_i^\beta T \mathbf{X}_{\rho \hat{y} \hat{z}} \approx 0 \quad i = 0, 1, 2 \quad (5.21)$$

where

$$b_i^\alpha = \Phi_\rho(t_i) - \rho_c \cos \phi_c \tan \alpha \Phi_\theta(t_i) \quad (5.22)$$

$$b_i^\beta = -\tan \beta \cos \phi_c \Phi_\theta(t_i) + \Phi_\phi(t_i) \quad (5.23)$$

And Eqs. 5.16 and 5.17 can be rewritten using the same, transition matrix relationships:

$$\begin{aligned} & \mathbf{X}_0^T \left[-\frac{\rho_c}{2} \Phi_\phi^T(t_i) \Phi_\phi(t_i) - \frac{\rho_c}{2} \cos^2 \phi_c \Phi_\theta^T(t_i) \Phi_\theta(t_i) \right] \mathbf{X}_0 \\ & \mathbf{X}_0^T \left[-\cos \phi_c \tan \alpha \Phi_\theta^T(t_i) \Phi_\rho(t_i) + \rho_c \sin \phi_c \tan \alpha \Phi_\theta^T(t_i) \Phi_\phi(t_i) \right] \mathbf{X}_0 \\ & \quad + [\Phi_\rho(t_i) - \rho_c \cos \phi_c \tan \alpha \Phi_\theta(t_i)] \mathbf{X}_0 \approx 0 \quad (5.24) \end{aligned}$$

$$\begin{aligned} & \mathbf{X}_0^T \left[\frac{\sin \phi_c \cos \phi_c}{2} \Phi_\theta^T(t_i) \Phi_\theta(t_i) + \tan \beta \sin \phi_c \Phi_\theta^T(t_i) \Phi_\phi(t_i) \right] \mathbf{X}_0 \\ & \quad + [-\tan \beta \cos \phi_c \Phi_\theta(t_i) + \Phi_\phi(t_i)] \mathbf{X}_0 \approx 0 \quad (5.25) \end{aligned}$$

Notice that Eqs. 5.24 and 5.25 can be rewritten in a more compact form

$$\mathbf{X}_0^T A_i^\alpha \mathbf{X}_0 + b_i^\alpha \mathbf{X}_0 \approx 0 \quad (5.26)$$

$$\mathbf{X}_0^T A_i^\beta \mathbf{X}_0 + b_i^\beta \mathbf{X}_0 \approx 0 \quad i = 0, 1, 2$$

or using Eq. 5.13 the compact form can be written as

$$\begin{aligned} \mathbf{X}_0^T T^T A_i^\alpha T \mathbf{X}_0 + b_i^\alpha T \mathbf{X}_0 &\approx 0 \\ \mathbf{X}_0^T T^T A_i^\beta T \mathbf{X}_0 + b_i^\beta T \mathbf{X}_0 &\approx 0 \quad i = 0, 1, 2 \end{aligned} \quad (5.27)$$

where

$$\begin{aligned} A_i^\alpha &= -\frac{\rho_c}{2} \Phi_\phi^T(t_i) \Phi_\phi(t_i) - \frac{\rho_c}{2} \cos^2 \phi_c \Phi_\theta^T(t_i) \Phi_\theta(t_i) \\ &\quad - \cos \phi_c \tan \alpha \Phi_\theta^T(t_i) \Phi_\rho(t_i) + \rho_c \sin \phi_c \tan \alpha \Phi_\theta^T(t_i) \Phi_\phi(t_i) \end{aligned} \quad (5.28)$$

$$A_i^\beta = \frac{\sin \phi_c \cos \phi_c}{2} \Phi_\theta^T(t_i) \Phi_\theta(t_i) + \tan \beta \sin \phi_c \Phi_\theta^T(t_i) \Phi_\phi(t_i) \quad (5.29)$$

The ultimate goal of the IROD algorithm derived below is to find a solution of the initial relative states, \mathbf{X}_0 , in Eq. 5.27.

5.5 Approximate Angles-Only IROD Solution , $N = 3$ Observations

Given three observations (three azimuth and three elevation angles), an approximate, non-trivial solution to the first-order linearized measurement equations in Eq. 5.20 is determined by singular value decomposition [55] of the matrix

$$B = \begin{bmatrix} b_0^\alpha \\ b_0^\beta \\ b_1^\alpha \\ b_1^\beta \\ b_2^\alpha \\ b_2^\beta \end{bmatrix} = U \Sigma V^* \quad (5.30)$$

where the elements of B are given by Eq. 5.22 and $U = [\mathbf{u}_0, \mathbf{u}_1, \mathbf{u}_2, \mathbf{u}_3, \mathbf{u}_4, \mathbf{u}_5]$ contain the six left-singular vectors, $V = [\mathbf{v}_0, \mathbf{v}_1, \mathbf{v}_2, \mathbf{v}_3, \mathbf{v}_4, \mathbf{v}_5]$ contains the 6 right-singular vectors, and Σ is a diagonal matrix of singular values, σ_i , $i = 0, 1, 2, 3, 4, 5$. Since $BX_0 \approx 0$, there exists a singular value, σ_0 , with an associated right-singular vector, \mathbf{v}_0 , that satisfies

$$B\mathbf{v}_0 = \sigma_0\mathbf{u}_0 \approx 0 \quad (5.31)$$

Coincidentally, the selection of the correct singular value, σ_0 , and the associated correct right singular vector is vital for an accurate IROD solution. The smallest singular value and its associated right singular vector, are sometimes not the correct singular value eigenvector. The correct right singular vector is in the same direction as the first LOS measurement. Since the azimuth and elevation angles are used in the IROD solution, the azimuth and elevation angles can be used to calculate an approximate LOS unit vector. The LOS unit vector can be calculated as

$$\begin{bmatrix} \hat{x} \\ \hat{y} \\ \hat{z} \end{bmatrix} = \begin{bmatrix} \sin \alpha \\ \cos \alpha \cos \beta \\ \cos \alpha \sin \beta \end{bmatrix} \quad (5.32)$$

where α and β are the initial azimuth and elevation angles, \hat{x} , \hat{y} , and \hat{z} are the unit vectors in the radial, downrange and cross-track directions respectively. To find the correct right singular vector, the dot product of the LOS unit vector in Eq. 5.32, is dotted with each of the right singular vectors is computed and the maximum result is the correct right singular vector (in the correct direction).

Thus, based only on the first-order expansion of the azimuth and elevation measurement model, \mathbf{X}_0 is approximately a scalar multiple of \mathbf{v}_0

$$\mathbf{X}_0 = k_0\mathbf{v}_0 \quad (5.33)$$

where k_0 is unknown.

Since the true solution for \mathbf{X}_0 is expected to be near $k_0\mathbf{v}_0$, the proposed structure of the solution to the six quadratic equations is expressed in terms of six unknown parameters, $k_0, \delta k_1, \delta k_2, \delta k_3, \delta k_4, \delta k_5$

$$\mathbf{X}_0 = k_0\mathbf{v}_0 + \delta k_1\mathbf{v}_1 + \delta k_2\mathbf{v}_2 + \delta k_3\mathbf{v}_3 + \delta k_4\mathbf{v}_4 + \delta k_5\mathbf{v}_5 = k_0\mathbf{v}_0 + V_5\delta\mathbf{k} \quad (5.34)$$

where $V_5 = [\mathbf{v}_1, \mathbf{v}_2, \mathbf{v}_3, \mathbf{v}_4, \mathbf{v}_5]$ and $\delta\mathbf{k} = [\delta k_1, \delta k_2, \delta k_3, \delta k_4, \delta k_5]^T$ and the six right-singular vectors, $\mathbf{v}_i, i = 0, 1, 2, 3, 4, 5$ span the six-dimensional solution space. In this way of formulating the problem, $k_0\mathbf{v}_0$ is the larger or dominate term of the solution and $V_5\delta\mathbf{k}$ is the smaller or minor part of the solution. Thus, the six unknown parameters of \mathbf{X}_0 have been replaced by the six unknown parameters $k_0, \delta k_1, \delta k_2, \delta k_3, \delta k_4, \delta k_5$. The advantage in formulating a solution in this form is that all of the δk 's can be assumed to be small compared to k_0 which is not possible with the unknown parameters of \mathbf{X}_0 .

The six unknown parameters, k_0 and $\delta\mathbf{k}$ can be determined by first substituting Eq. 5.34 into Eq. 5.26

$$k_0^2\mathbf{v}_0^T A_i^\alpha \mathbf{v}_0 + 2k_0\mathbf{v}_0^T A_i^\alpha V_5 \delta\mathbf{k} + \delta\mathbf{k}^T V_5^T A_i^\alpha V_5 \delta\mathbf{k} + b_i^\alpha k_0\mathbf{v}_0 + b_i^\alpha V_5 \delta\mathbf{k} \approx 0 \quad (5.35)$$

and a similar expression for A_i^β and b_i^β . If the second-order term, $\delta\mathbf{k}^T V_5^T A_i^\alpha V_5 \delta\mathbf{k}$, is assumed to be small, Eq. 5.35 can be rewritten as

$$\left(k_0^2\mathbf{v}_0^T A_i^* \mathbf{v}_0 + b_i^* k_0\mathbf{v}_0\right) + \left(2k_0\mathbf{v}_0^T A_i^\alpha V_5 + b_i^\alpha V_5\right) \delta\mathbf{k} \approx 0 \quad (5.36)$$

where the last five equations can be solved for $\delta\mathbf{k}$ in terms of k_0

$$\delta\mathbf{k} = -(k_0 D_5 + B_5 V_5)^{-1} \left(k_0^2 C_5 + k_0 B_5 \mathbf{v}_0\right) \quad (5.37)$$

where

$$B_5 = \begin{bmatrix} b_0^\beta \\ b_1^\alpha \\ b_1^\beta \\ b_2^\alpha \\ b_2^\beta \end{bmatrix}, \quad C_5 = \begin{bmatrix} \mathbf{v}_0^T A_0^\beta \mathbf{v}_0 \\ \mathbf{v}_0^T A_1^\alpha \mathbf{v}_0 \\ \mathbf{v}_0^T A_1^\beta \mathbf{v}_0 \\ \mathbf{v}_0^T A_2^\alpha \mathbf{v}_0 \\ \mathbf{v}_0^T A_2^\beta \mathbf{v}_0 \end{bmatrix}, \quad D_5 = \begin{bmatrix} 2\mathbf{v}_0^T A_0^\beta V_5 \\ 2\mathbf{v}_0^T A_1^\alpha V_5 \\ 2\mathbf{v}_0^T A_1^\beta V_5 \\ 2\mathbf{v}_0^T A_2^\alpha V_5 \\ 2\mathbf{v}_0^T A_2^\beta V_5 \end{bmatrix} \quad (5.38)$$

Now, Eq. 5.37 can be substituted back into Eq. 5.36 to produce a single scalar equation in one unknown, k_0

$$\left(k_0^2 c_0 + b_0^\alpha k_0 \mathbf{v}_0\right) - (k_0 \mathbf{d}_0 + b_0^\alpha V_5) (k_0 D_5 + B_5 V_5)^{-1} \left(k_0^2 C_5 + k_0 B_5 \mathbf{v}_0\right) \approx 0 \quad (5.39)$$

where

$$c_0 = \mathbf{v}_0^T A_0^\alpha \mathbf{v}_0 \quad (5.40)$$

$$\mathbf{d}_0 = 2\mathbf{v}_0^T A_0^\alpha V_5 \quad (5.41)$$

Dividing both sides of Eq. 5.39 by $(k_0^2 c_0 + b_0^\alpha k_0 \mathbf{v}_0)$ to get

$$1 - (k_0 \mathbf{d}_0 + b_0^\alpha V_5) (k_0 D_5 + B_5 V_5)^{-1} \frac{(k_0^2 C_5 + k_0 B_5 \mathbf{v}_0)}{(k_0^2 c_0 + b_0^\alpha k_0 \mathbf{v}_0)} \approx 0 \quad (5.42)$$

The solution to Eq. 5.42 for k_0 requires the inverse of a 6×6 matrix in terms of k_0 . This can be greatly simplified by making use of the following identity, the Matrix Determinant Lemma [56]:

$$\text{Det} \left[1 - PQ^{-1}R \right] = \frac{\text{Det} [Q - RP]}{\text{Det} [Q]} \quad (5.43)$$

So from Eq. 5.42 we can write

$$\begin{aligned}
 P &= k_0 \mathbf{d}_0 + b_0^\alpha V_5 \\
 Q &= k_0 D_5 + B_5 V_5 \\
 R &= \frac{k_0^2 C_5 + k_0 B_5 \mathbf{v}_0}{k_0^2 c_0 + b_0^\alpha k_0 \mathbf{v}_0}
 \end{aligned} \tag{5.44}$$

which gives us

$$1 - PQ^{-1}R = 0 \tag{5.45}$$

Taking the determinant of both sides of this equation and applying the identity in Eq. 5.43 results in

$$\frac{\text{Det}[Q - RP]}{\text{Det}[Q]} = 0 \tag{5.46}$$

Now, multiplying both sides by $\text{Det}[Q]$ and substituting P , Q , and R from Eq. 5.44 into the equation above gives

$$\text{Det} \left[(k_0 D_5 + B_5 V_5) - \frac{(k_0^2 C_5 + k_0 B_5 \mathbf{v}_0)(k_0 \mathbf{d}_0 + b_0^\alpha V_5)}{k_0^2 c_0 + k_0 b_0^\alpha \mathbf{v}_0} \right] = 0 \tag{5.47}$$

Since the denominator $k_0^2 c_0 + k_0 b_0^\alpha \mathbf{v}_0$ is a scalar it can be factored out of the determinant to produce the final result

$$\text{Det} \left[(k_0^2 c_0 + k_0 b_0^\alpha \mathbf{v}_0) (k_0 D_5 + B_5 V_5) - (k_0^2 C_5 + k_0 B_5 \mathbf{v}_0) (k_0 \mathbf{d}_0 + b_0^\alpha V_5) \right] = 0 \tag{5.48}$$

A k_0 can be factored out from the determinant to reduce the order of the polynomial from Eq. 5.48.

$$\text{Det} [(k_0 c_0 + b_0^\alpha \mathbf{v}_0) (k_0 D_5 + B_5 V_5) - (k_0 C_5 + B_5 \mathbf{v}_0) (k_0 \mathbf{d}_0 + b_0^\alpha V_5)] = 0 \tag{5.49}$$

The equation is a maximum 10th-order polynomial in k_0 where sometimes the order of the polynomial will be less if the 5x5 matrix in Eq. 5.49 is not fully populated. So, there are a maximum of 10 roots resulting from the solution of the 10th-order polynomial

equation in k_0 . The selection of feasible roots (roots that yield feasible IROD solutions) is not a trivial problem and Section 5.7 explains this root selection process in detail. The roots of this polynomial are substituted back into Eq. 5.37 to find $\delta\mathbf{k}$. The solution for the initial relative states is then just given by Eq. 5.34

$$\mathbf{X}_0 = k_0\mathbf{v}_0 + V_5\delta\mathbf{k} \quad (5.50)$$

5.6 Improving the IROD Solution, $N = 3$ Observations

Once an approximate solution to the IROD problem is obtained, a simple iterative algorithm can be applied to improve the solution. The approximate solution in Eq. 5.50 will not exactly satisfy the 6 quadratic equations in Eq. 5.26 because the second-order terms in $\delta\mathbf{k}$ have been neglected. The objective of the following iterative scheme is to recover these second-order terms and determine a more accurate solution to the 6 quadratic equations using the approximate solution as a starting point. It is important to point out that although an exact solution is typically found in a few iterations, this is not the exact solution to the original 2-body relative motion problem (with or without J_2). It is only the exact solution to the problem modeled by the second-order measurement equations and the linearized equations of relative motion in spherical coordinates.

Starting with the initial approximate solution \mathbf{X}_0 , let the exact solution be given by $\mathbf{X}_0^* = \mathbf{X}_0 + \delta\mathbf{X}_0$. Substitute \mathbf{X}_0^* into Eq. 5.26 and neglecting second-order terms in $\delta\mathbf{X}_0$ produces

$$\begin{aligned} \mathbf{X}_0^T A_i^\alpha \mathbf{X}_0 + 2\mathbf{X}_0^T A_i^\alpha \delta\mathbf{X}_0 + b_i^\alpha (\mathbf{X}_0 + \delta\mathbf{X}_0) &\approx 0, & i = 0, 1, 2 \\ \mathbf{X}_0^T A_i^\beta \mathbf{X}_0 + 2\mathbf{X}_0^T A_i^\beta \delta\mathbf{X}_0 + b_i^\beta (\mathbf{X}_0 + \delta\mathbf{X}_0) &\approx 0, & i = 0, 1, 2 \end{aligned} \quad (5.51)$$

These 6 equations can then be used to solve for $\delta\mathbf{X}_0$

$$\delta\mathbf{X}_0 = -M^{-1}N \quad (5.52)$$

where

$$M = \begin{bmatrix} 2\mathbf{X}_0^T A_0^\alpha + b_0^\alpha \\ 2\mathbf{X}_0^T A_0^\beta + b_0^\beta \\ 2\mathbf{X}_0^T A_1^\alpha + b_1^\alpha \\ 2\mathbf{X}_0^T A_1^\beta + b_1^\beta \\ 2\mathbf{X}_0^T A_2^\alpha + b_2^\alpha \\ 2\mathbf{X}_0^T A_2^\beta + b_2^\beta \end{bmatrix}, \quad N = \begin{bmatrix} \mathbf{X}_0^T A_0^\alpha \mathbf{X}_0 + b_0^\alpha \mathbf{X}_0 \\ \mathbf{X}_0^T A_0^\beta \mathbf{X}_0 + b_0^\beta \mathbf{X}_0 \\ \mathbf{X}_0^T A_1^\alpha \mathbf{X}_0 + b_1^\alpha \mathbf{X}_0 \\ \mathbf{X}_0^T A_1^\beta \mathbf{X}_0 + b_1^\beta \mathbf{X}_0 \\ \mathbf{X}_0^T A_2^\alpha \mathbf{X}_0 + b_2^\alpha \mathbf{X}_0 \\ \mathbf{X}_0^T A_2^\beta \mathbf{X}_0 + b_2^\beta \mathbf{X}_0 \end{bmatrix} \quad (5.53)$$

The value of $\mathbf{X}_0^* = \mathbf{X}_0 + \delta\mathbf{X}_0$ is then used as a starting point for the next iteration, i.e., set $\mathbf{X}_0 = \mathbf{X}_0 + \delta\mathbf{X}_0$ and repeat Eqs. 5.52-5.53. This is equivalent to a simple Newton-Raphson procedure applied to a set of 6 quadratic equations in 6 unknowns. The algorithm is simple and typically converges in a few iterations.

5.7 Feasible Root Selection Process

Included in this section is an explanation of the root selection process for one relative motion example. This example is a Leader-Follower case with downrange separation of 500 km, J_2 is off and the inclination of the chief vehicle is 10° . For comparison, the true initial relative states (in arc-length form) are given as

$$\begin{bmatrix} \rho_d \\ \delta \hat{y} \\ \delta \hat{z} \\ \dot{\rho}_d \\ \delta \hat{y} \\ \delta \hat{z} \end{bmatrix} = \begin{bmatrix} 0.000000007160716 \\ 4.924117812741954 \\ 0.868509867326283 \\ 0.00000000015400 \\ 0.000011241018532 \\ -0.000031345509776 \end{bmatrix} \times 10^5 (m)/(m/s)$$

Since all of the results that test the IROD solution are simulated results, the true initial relative states are known and that information can be used and compared with the IROD solutions to calculate an error residual from truth. For this particular case, there are 9 roots from the matrix determinant equation and they are given as

$$\mathbf{X}_0 = \begin{bmatrix} 0.000000000023 \\ 0.000000000023 \\ 0.000000000023 \\ 0.000000000023 \\ -3270.193936206584 \\ -862.361321304611 \\ 0.07358976907 \\ 4.709345584467 \\ 71.652935259169 \end{bmatrix} \times 10^5 \text{ meters}$$

Feasible roots are chosen that satisfy the following criteria:

- Positive (the setup of the test cases assume the deputy vehicle always has a positive downrange separation in the v_{bar} direction)
- Within 100 meters and 10,000 km (eliminates solutions that are outside the bounds of the relative motion models utilized)

Given the above criteria in this particular case, there are three feasible solutions

$$k_0 = \text{feasible roots} = \begin{bmatrix} 0.07358976907 \\ 4.709345584467 \\ 71.652935259169 \end{bmatrix} \times 10^5 \text{ meters}$$

Each of the above feasible roots is then plugged into the equation

$$\mathbf{X}_0 = k_0 \mathbf{v}_0 - V_5 (k_0 D_5 + B_5 V_5)^{-1} (k_0^2 C_5 + k_0 B_5 \mathbf{v}_0) \quad (5.54)$$

to get a feasible solution to the IROD problem. Residuals are then calculated for each of the feasible solutions. The feasible solutions are calculated to be

$$\mathbf{X}_0(1) = \begin{bmatrix} -0.0258896705108 \\ 0.0724269170709 \\ 0.01277082042662 \\ -0.00000009112455 \\ 0.00000404517151 \\ 0.00000072197355 \end{bmatrix} \times 10^5 (m)/(m/s)$$

$$\mathbf{X}_0(2) = \begin{bmatrix} -0.01012074024748 \\ 4.64040329119092 \\ 0.81822830160532 \\ 0.00000077384716 \\ 0.0000205747459 \\ -0.00002602237964 \end{bmatrix} \times 10^5 (m)/(m/s)$$

$$\mathbf{X}_0(3) = \begin{bmatrix} 32.82238715997516 \\ 71.76430694142002 \\ 12.65398356561613 \\ -0.03044115776186 \\ -0.05034332617120 \\ -0.01142891918514 \end{bmatrix} \times 10^5 (m)/(m/s)$$

Since these feasible solutions (\mathbf{X}_0) do not exactly satisfy the quadratic equations (because the second-order terms were assumed to be small), a simple iterative improvement algorithm is used to iterate on the above feasible solutions so that the quadratic equations are satisfied to numerical precision. The iteratively improved roots (\mathbf{X}_0^*) are calculated to be

$$\mathbf{X}_0^*(1) = \begin{bmatrix} -0.00258960749630 \\ 0.0724451517600 \\ 0.01277403488316 \\ -0.00000009114631 \\ 0.00000404617348 \\ 0.00000072215020 \end{bmatrix} \times 10^5 (m)/(m/s)$$

$$\mathbf{X}_0^*(2) = \begin{bmatrix} -0.00001762926979 \\ 4.925646184880150 \\ 0.86852431980422 \\ 0.000000212582642 \\ 0.00000563288540 \\ -0.00003239511931 \end{bmatrix} \times 10^5 (m)/(m/s)$$

$$\mathbf{X}_0^*(3) = \begin{bmatrix} 54.13796843968275 \\ 90.21583586633945 \\ 15.9074859040208 \\ -0.04970477766798 \\ -0.08268648712777 \\ -0.01858280625684 \end{bmatrix} \times 10^5 (m)/(m/s)$$

Table 5.1: First of Three Feasible IROD Solutions and Residuals

$\mathbf{X}_0^*(1)$			
Position Error (percent)	99		
Quadratic Residual (percent)	2.9×10^{-12}		
Linearized Spherical Residual (rad)	8.4×10^{-4}		
2-body/ J_2 residual (rad)	2.8×10^{-5}		
Dot Product Residual (rad)	2.8×10^{-5}		
ROE Ratios	$x_r = 1.003$ $E_r = 0.015$	$y_r = 0.015$ $A_z = 1.000$	$a_r = 1.002$ $\psi = 0.015$

Table 5.2: Second of Three Feasible IROD Solutions and Residuals

$\mathbf{X}_0^*(2)$			
Position Error (percent)	3.4×10^{-2}		
Quadratic Residual (percent)	3.7×10^{-14}		
Linearized Spherical Residual (rad)	4.5×10^{-3}		
2-body/ J_2 residual (rad)	1.8×10^{-3}		
Dot Product Residual (rad)	1.8×10^{-3}		
ROE Ratios	$x_r = 1.000$ $E_r = 1.000$	$y_r = 1.000$ $A_z = 1.000$	$a_r = 1.000$ $\psi = 1.001$

The second feasible solution, $\mathbf{X}_0^*(2)$, is closest to the true initial relative states. Even though the first and third solutions also satisfy the quadratic equations (the quadratic residual percent is low) these solutions do not yield the correct initial relative states (refer to the percent position error). For an on-board implementation of this IROD algorithm, the task of disambiguation, choosing which of the IROD solutions is the best estimate, is not a trivial problem. The disambiguation problem is acknowledged but not pursued in this research. However, an example of some desired residuals for this case are shown in the tables below:

Table 5.3: Third of Three Feasible IROD Solutions and Residuals

$\mathbf{X}_0^*(3)$			
Position Error (percent)	2×10^3		
Quadratic Residual (percent)	1.2×10^{-12}		
Linearized Spherical Residual (rad)	1.8×10^{-1}		
2-body/ J_2 residual (rad)	1.8×10^{-1}		
Dot Product Residual (rad)	8.2×10^{-1}		
ROE Ratios	$x_r = 0.107$ $E_r = -5.948$	$y_r = 7.663$ $A_z = 2.789$	$a_r = 0.032$ $\psi = 30.406$

The linearized spherical residual is a LOS residual where the deputy vehicle is initialized at the IROD estimate and then propagated forward using the linearized, spherical equations of relative motion. At each measurement time, the LOS of the propagated linearized deputy is compared with the measured LOS vectors and the residual is calculated.

The 2-body/ J_2 residual is very similar. The deputy vehicle is initialized at the IROD estimate and then propagated forward using the nonlinear two-body + J_2 perturbation (when J_2 is turned on in the simulation) equations of motion. At each measurement time, the LOS of the propagated 2-body/ J_2 deputy is compared with the measured LOS vectors and the residual is calculated.

The Dot Product Residual is very similar to the 2-body/ J_2 residual. At each measurement time, the LOS of the propagated 2-body/ J_2 deputy is dotted with the measured LOS vector and the RMS of those dot products are the residual.

The Relative Orbital Element (ROE) ratios are just helpful metrics for visualizing the relative motion shape in the LVLH frame. The ratios are the estimated relative orbital elements divided by the true relative orbital elements. Again, this is a residual that is available only when running simulation cases since the true relative orbital elements would be unknown when implementing this IROD algorithm on-board an actual mission.

For all of the cases presented for the rest of the paper, only the number of solutions and the percent position error residual will be tabulated. For the purpose of verifying that the IROD algorithm gives accurate solutions close to the true initial relative states, this is the best metric. The metric would not be available, however, when taking real LOS measurements from an unknown object since the true initial relative states are unknown and the problem of disambiguation needs to be addressed.

5.8 IROD Performance Tables (Simplified Models)

In this section the IROD algorithm is tested with linearized dynamics (including J_2) and second-order measurement equations. The value of performing the following test on the IROD algorithm is to verify that the IROD algorithm is able to correctly extract the correct IROD solution using the same dynamics and measurement equations that the IROD

solution itself is derived from. This is a valuable step to implement before introducing nonlinearities in the form of nonlinear dynamics and using nonlinear measurement models for the LOS measurements. Once the IROD algorithm shows that it consistently and accurately finds the correct initial relative states, we can say that the IROD solution works in the environment that it was derived in and then the IROD algorithm can be tested in a nonlinear environment. A number of cases are shown below where the variables can be listed as:

- Trajectory type - Leader-Follower, Flyby, Football Orbits
- Downrange Separation: 0.5 km , 5 km , 50 km , 500 km
- J_2 Perturbations are ON
- Cross-track Separation: 0%, 10%
- Iterative Improvement Algorithm (ON or OFF)
- Orbital Elements - inclination (0° , 10° , 45° , 60°) and eccentricity (0, 0.01, 0.1)

For the cases where only three observations (three azimuth, three elevation angles) are used, it is necessary to introduce some cross-track separation into each trajectory. Without any cross-track motion, all of the trajectories are in-plane and the problem becomes unobservable (four observations are required when in-plane trajectories are considered). Although the J_2 perturbation does introduce some cross-track motion, the motion is small and the total time from the first to the last measurement is typically not long enough for J_2 perturbations to cause precessions that would make the problem observable without more angle measurements.

Three relative motion trajectories are simulated with other varying parameters. Figures A through C show how each of these cases are initialized. Each figure shows the relative motion of a deputy vehicle with respect to a chief vehicle in a LVLH frame with LOS vectors pointing from the deputy to the chief at each measurement time. These figures show how each of the simulation cases presented in the following tables are initialized.

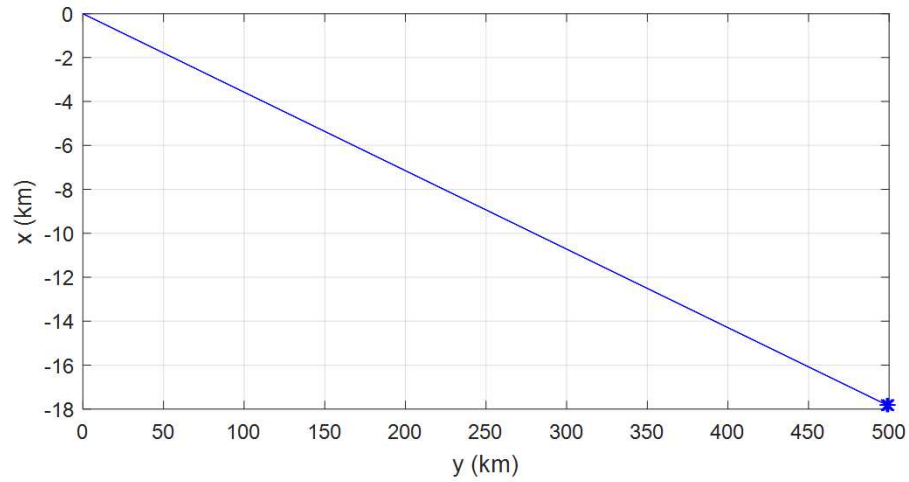


Fig. 5.2: Leader-Follower Relative Motion Simulation, 500 km Separation, LEO, $N = 4$ Observations, $T_f = 3000 \text{ sec}$

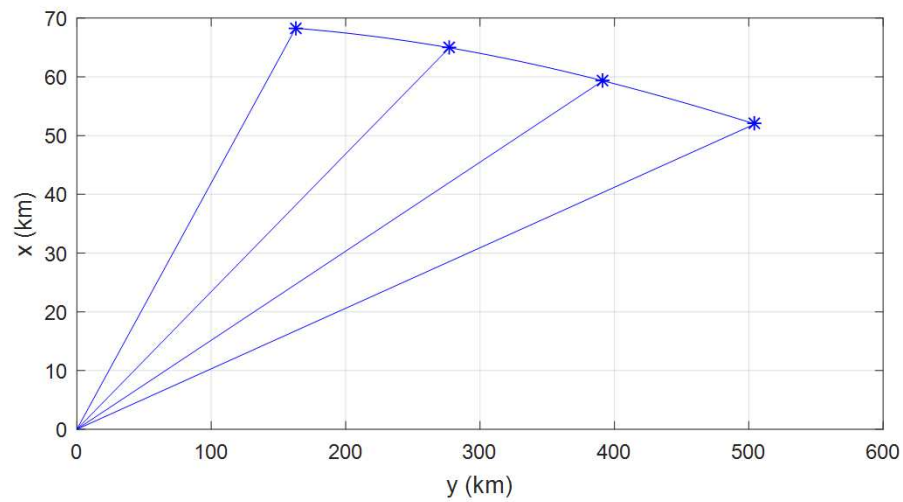


Fig. 5.3: Flyby Relative Motion Simulation, 500 km DownrangeSeparation, 70 km LEO, $N = 4$ Observations, $T_f = 3000 \text{ sec}$

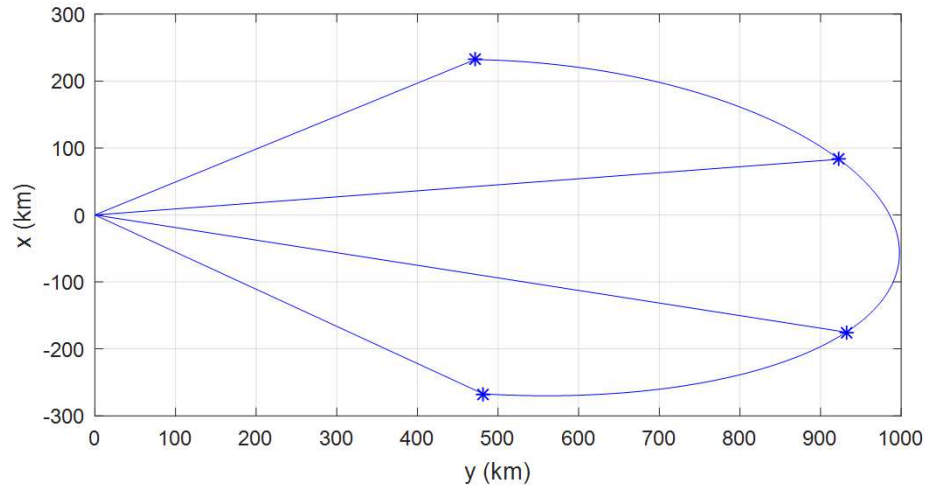


Fig. 5.4: Football Relative Motion Simulation, 500 km Downrange Separation, LEO, $N = 4$ Observations, $T_f = 3000 \text{ sec}$

As a reminder, the IROD algorithm determines an approximate solution to six quadratic equations with six unknowns. So, a simple iterative improvement method is used (a Simple Newton Raphson method) to arrive at the exact solution to the six quadratic equations with six unknowns (to numerical precision). In the tables below, the iterative improvement method is labeled in columns with a “Q”. So, each case has listed two numbers or solutions; the IROD algorithm comes up with an approximate solution and then the Q method finds the exact solution (to numerical precision).

For most of the cases shown below, the percent position errors are the preferred metric displayed because these are all simulation results where the true relative position of the deputy is known and it provides the best metric of the accuracy of the IROD algorithm in these simulation cases. When implemented in an actual, on-board mission, the true initial relative states are not known so some sort of LOS residual would be preferred to determine the accuracy of the IROD solutions. Each table also includes a column that notes the number of feasible solutions the IROD algorithm generated (labeled as Num.). For all of the cases below, the IROD solution with the lowest percent position error was chosen as the “best” solution. The problem of disambiguation, choosing which of multiple IROD solutions is the most accurate or “best” is a non-trivial but separate problem that is not

Table 5.4: Color-Code Categorization for Percent Position Tables

Percent Position Range	Highlighted Color
0-20% (good)	black
21-50% (poor)	blue
50% and up (bad)	red

Table 5.5: Percent Position Errors, Simplified Models, Leader-Follower, $N = 3$, $\Delta t = 1000 \text{ sec}$, $\Delta z = 10\%$

inc	Dwn. Sep.	$e = 0$			$e = 0.01$			$e = 0.1$		
		Num.	IROD	Q	Num.	IROD	Q	Num.	IROD	Q
0°	0.5 km	2	1.0e-6	9.1e-10	2	8.9e-5	1.2e-9	2	9.2e-4	1.8e-9
	5 km	2	1.0e-4	1.4e-10	2	7.9e-4	7.2e-11	2	9.1e-3	1.7e-10
	50 km	2	1.0e-2	2.2e-12	2	1.5e-3	1.1e-11	2	8.2e-2	1.8e-11
	500 km	2	1.2	3.2e-12	2	1.1	2.3e-13	2	2.6e-1	4.5e-12
10°	0.5 km	3	2.7e-4	8.7e-10	3	3.8e-4	3.9e-9	3	2.0e-3	7.3e-9
	5 km	3	2.5e-3	6.8e-11	3	3.6e-3	3.0e-10	3	2.0e-2	1.5e-9
	50 km	3	6.3e-3	1.9e-11	3	1.6e-2	4.4e-11	3	1.8e-1	3.7e-11
	500 km	3	4.8e2	3.5e-12	3	4.5e2	2.4e-12	3	1.2	8.6e-12
45°	0.5 km	3	4.2e-2	3.7e-9	3	7.2e-2	5.6e-8	2	1.1e-2	5.1e-10
	5 km	3	4.3e-1	2.1e-9	3	7.3e-1	1.5e-9	2	1.1e-1	3.6e-10
	50 km	3	4.5	4.6e-11	3	8.1	2.8e-10	2	1.1	5.0e-11
	500 km	3	62	52	3	54	3.8e-11	2	9.1	3.1e-13
60°	0.5 km	3	1.0e5	4.3e-9	2	7.0e5	1.5e-7	2	1.4e-2	6.3e-9
	5 km	3	1.7	2.2e-9	2	9.0	4.6e-9	2	1.4e-1	4.8e-10
	50 km	3	17	4.5e-12	2	65	5.4e-10	2	1.4	9.7e-12
	500 km	3	94	94	2	1.2e2	1.5e-7	2	15	4.e-13

addressed or included in this work. For the following cases the final time is $T_f = 2000 \text{ sec}$ with $\Delta t = 1000 \text{ sec}$ for $N = 3$ observations and the propagation time step is 10 sec . Table 5.4 shows a color-coding categorization of the percent position errors shown in the following tables.

The Leader-Follower cases above show very good agreement between the best IROD solution from the IROD algorithm and the true relative position. Even if the approximate IROD solution is unable to accurately estimate the initial relative states, the iterative improvement (the Q column) on the IROD solution is able to iterate to a more accurate estimate of the initial relative states and decrease the percent position error of the estimate. For the most part, an increase in downrange separation of the leader-follower configuration will increase the percent position error of the initial IROD estimate (in the IROD column) but ultimately decrease the percent position error of the iteratively-improved IROD solution

Table 5.6: Percent Position Errors, Simplified Models, Flyby, $N = 3$, $\Delta t = 1000 \text{ sec}$, $\Delta z = 10\%$

inc	Dwn. Sep.	$e = 0$			$e = 0.01$			$e = 0.1$		
		Num.	IROD	Q	Num.	IROD	Q	Num.	IROD	Q
0°	0.5 km	2	1.0e-3	6.5e-9	2	1.1e-3	5.8e-9	2	5.7e-3	2.0e-8
	5 km	2	1.0e-2	2.2e-10	2	1.1e-2	5.0e-10	2	5.7e-2	2.5e-9
	50 km	2	9.2e-2	4.6e-11	2	1.0e-1	7.2e-11	2	5.9e-1	8.8e-11
	500 km	2	2.8e-2	2.2e-12	2	1.2e-1	1.3e-12	2	10	9.3e-11
10°	0.5 km	2	5.4e-3	3.5e-9	2	9.2e-3	9.1e-8	1	2.1e-3	1.4e-9
	5 km	2	5.4e-2	3.9e-9	2	9.3e-2	3.8e-9	1	2.1e-2	3.5e-9
	50 km	2	5.5e-1	3.6e-10	2	1.0	6.2e-10	1	2.0e-1	3.8e-11
	500 km	2	8.1	1.3e-10	2	6.8	1.7e-10	1	1.6	5.8e-12
45°	0.5 km	2	6.9e-3	4.7e-9	2	6.1e-3	7.4e-10	2	2.6e-3	6.1e-9
	5 km	2	6.9e-2	6.5e-10	2	6.1e-2	9.3e-10	2	2.6e-2	5.1e-10
	50 km	2	6.8e-1	9.4e-11	2	6.0e-1	3.5e-11	2	2.7e-1	2.9e-11
	500 km	2	6.4	6.7e-12	2	5.8	2.1e-12	2	3.1	6.5e-12
60°	0.5 km	2	1.3e-2	1.3e-9	2	1.1e-2	6.9e-9	2	1.6e6	2.3e-9
	5 km	2	1.3e-1	2.6e-10	2	1.1e-1	6.9e-10	2	4.7e-2	3.2e-10
	50 km	2	1.3	2.6e-11	2	1.1	6.9e-11	2	4.7e-1	1.8e-11
	500 km	2	13	6.1e-12	2	12	3.3e-12	2	1.4e3	4.8e-13

(in the Q column). The percent position errors are low enough that they validate the accuracy of the IROD solution. There are only two cases, where the separation is large (500 km) and the inclination is large, where the IROD algorithm is not able to accurately estimate the initial relative motion states.

The Flyby cases above show good agreement between the best IROD solution and the true initial relative position. Even if the initial IROD solution does not get an accurate estimate, the iterative improvement of that IROD solution is able to decrease the percent position error and show good agreement between truth and the IROD estimate. The same trend of decreasing percent position error for increasing downrange separation is also apparent in these flyby cases.

The Football cases above show good agreement between the best IROD solution and the true initial relative position. For several of the cases above, the initial IROD estimates (in the IROD column) are very poor (the percent position errors are very large) so the neglected second order terms are significant. Including them in the iterative improvement then reduces the percent position error and shows that the IROD algorithm is able to find good estimates for the initial relative states. The same trend of decreasing percent position

Table 5.7: Percent Position Errors, Simplified Models, Football, $N = 3$, $\Delta t = 1000 \text{ sec}$, $\Delta z = 10\%$

inc	Dwn. Sep.	$e = 0$			$e = 0.01$			$e = 0.1$		
		Num.	IROD	Q	Num.	IROD	Q	Num.	IROD	Q
0°	0.5 km	3	1.1e-3	3.6e-10	3	1.1e-3	1.0e-9	1	5.4e-4	8.8e-10
	5 km	3	9.6e5	1.7e-11	3	1.3e6	3.5e-11	1	5.8e-3	9.8e-11
	50 km	3	1.5e-1	2.0e-12	3	8.0e4	7.2e-12	1	1.1e-1	1.2e-11
	500 km	2	1.0e3	2.3e-13	2	9.6e2	6.4e-13	2	5.7e2	1.5e-12
10°	0.5 km	4	7.3e4	3.0e-9	4	6.9e-4	2.6e-9	4	7.6e-5	7.0e-11
	5 km	4	2.1e4	1.1e-10	4	8.3e-3	1.2e-11	4	3.0e-3	4.9e-11
	50 km	4	1.5e5	3.4e-13	4	2.4e-1	1.2e-12	4	2.9e-1	1.3e-11
	500 km	4	13	4.0e-13	4	14	6.1e-13	2	33	4.3e-11
45°	0.5 km	2	1.5e-1	1.1e-8	2	3.4e-1	6.5e-9	1	3.2e-2	3.0e-9
	5 km	2	1.5	6.7e-10	2	3.8	5.0e-9	1	3.2e-1	3.0e-10
	50 km	2	22	6.1e-10	2	50	1.5e-2	1	2.7	2.6e-11
	500 km	3	9.1e-1	6.8e-12	3	5.1e-1	6.3e-12	3	3.1	7.8e-14
60°	0.5 km	1	1.1	7.4e-8	1	2.6e-1	7.8e-9	1	3.4e-2	3.2e-9
	5 km	1	10	1.9e-9	1	2.6	5.8e-10	1	3.4e-1	4.2e-10
	50 km	1	44	1.5e-10	1	20	1.3e-10	1	3.3	5.4e-12
	500 km	3	1.3e3	2.3e-11	3	25	1.2e-11	3	27	8.9e-12

error for increasing downrange separation is also apparent in these football cases.

This section outlined an approximate Initial Relative Orbit Determination algorithm that uses three line-of-sight observations (six angle measurements) to determine an estimate for the initial relative states. A simple iterative improvement algorithm is also derived, which takes into account the previously-neglected second-order terms of the measurement equations and provides a better estimate of the initial relative states. Several example relative motion cases are presented above where the dynamics are linearized and the measurement equations are second-order. Cases are presented for a variety of inclinations, eccentricities and relative motion configurations. For almost all of these cases tabulated above, the IROD algorithm is able to accurately extract the correct initial relative states, validating that in this simplified environment, the IROD algorithm functions well.

CHAPTER 6

INITIAL RELATIVE ORBIT DETERMINATION PROBLEM, $N > 3$ OBSERVATIONS**6.1 Approximate Angles-Only IROD Solution, $N > 3$ Observations**

An approximate solution to the IROD problem can be formulated for more than three observations. Most satellite tracking mission are not restricted to only three observations of neighboring satellites. Since more observations may be available, this algorithm makes use of those observations, with the idea that more observations over a longer period of time will provide a better estimate of the initial relative states. The derivation with $N > 3$ is very similar to the $N = 3$ derivation.

From the first order expansion of the measurement equation, Eq. 5.20 can be used where instead of three observations, N observations are available

$$b_i^\alpha \mathbf{X}_0 \approx 0, \quad b_i^\beta \mathbf{X}_0 \approx 0 \quad i = 0, 1, 2, \dots, n-1 \quad (6.1)$$

With N observations, the B matrix is formed as

$$B_{2n \times 6} = \begin{bmatrix} b_0^\alpha \\ b_0^\beta \\ \vdots \\ b_{n-1}^\alpha \\ b_{n-1}^\beta \end{bmatrix} \quad (6.2)$$

where the dimensions of B are $2n \times 6$ where n is the number of observations. Taking the singular value decomposition of this B matrix will yield $B = U\Sigma V^*$ where

$$U_{2n \times 2n} = [\mathbf{u}_0, \mathbf{u}_1, \dots, \mathbf{u}_{2n-1}] \quad (6.3)$$

$$V_{6 \times 6} = [\mathbf{v}_0, \mathbf{v}_1, \dots, \mathbf{v}_5] \quad (6.4)$$

And Σ still provides 6 singular values, σ_i , $i = 0, 1, 2, 3, 4, 5$ where σ_0 is a singular value and \mathbf{v}_0 is the right-singular vector that is associated with σ_0 which satisfies

$$B\mathbf{v}_0 = \sigma_0\mathbf{u}_0 \approx 0 \quad (6.5)$$

The selection of the correct right-singular vector is not trivial. The correct right singular vector is in the same direction as the first LOS measurement. The selection of the correct eigenvector and its associated eigenvalue is the same process with $N > 3$ as it is when $N = 3$. The proposed structure of the solution is now written as

$$\mathbf{X}_0 = k_0\mathbf{v}_0 + \delta k_1\mathbf{v}_1 + \delta k_2\mathbf{v}_2 + \delta k_3\mathbf{v}_3 + \delta k_4\mathbf{v}_4 + \delta k_5\mathbf{v}_5 = k_0\mathbf{v}_0 + V_5\delta\mathbf{k} \quad (6.6)$$

where $V_5 = [\mathbf{v}_1, \mathbf{v}_2, \mathbf{v}_3, \mathbf{v}_4, \mathbf{v}_5]$ and $\delta\mathbf{k} = [\delta k_1, \delta k_2, \delta k_3, \delta k_4, \delta k_5]^T$. The six unknown parameters, k_0 and $\delta\mathbf{k}$ can be determined by first substituting Eq.6.6 into

$$\begin{aligned} \mathbf{X}_0^T A_i^\alpha \mathbf{X}_0 + b_i^\alpha \mathbf{X}_0 &\approx 0 \quad i = 0, 1, 2, \dots, n-1 \\ \mathbf{X}_0^T A_i^\beta \mathbf{X}_0 + b_i^\beta \mathbf{X}_0 &\approx 0 \quad i = 0, 1, 2, \dots, n-1 \end{aligned} \quad (6.7)$$

This produces

$$k_0^2 \mathbf{v}_0^T A_i^\alpha \mathbf{v}_0 + 2k_0 \mathbf{v}_0^T A_i^\alpha V_5 \delta\mathbf{k} + \delta\mathbf{k}^T V_5^T A_i^\alpha V_5 \delta\mathbf{k} + k_0 b_i^\alpha \mathbf{v}_0 + b_i^\alpha V_5 \delta\mathbf{k} \approx 0, \quad i = 0, 1, 2, \dots, n-1 \quad (6.8)$$

$$k_0^2 \mathbf{v}_0^T A_i^\beta \mathbf{v}_0 + 2k_0 \mathbf{v}_0^T A_i^\beta V_5 \delta\mathbf{k} + \delta\mathbf{k}^T V_5^T A_i^\beta V_5 \delta\mathbf{k} + k_0 b_i^\beta \mathbf{v}_0 + b_i^\beta V_5 \delta\mathbf{k} \approx 0, \quad i = 0, 1, 2, \dots, n-1 \quad (6.9)$$

If the second-order term, $\delta\mathbf{k}^T V_5^T A_i^\alpha V_5 \delta\mathbf{k}$, is assumed to be small, Eq. 6.8 can be rewritten as

$$\left(k_0^2 \mathbf{v}_0^T A_i^\alpha \mathbf{v}_0 + k_0 b_i^\alpha \mathbf{v}_0 \right) + \left(2k_0 \mathbf{v}_0^T A_i^\alpha + b_i^\alpha \right) V_5 \delta\mathbf{k} \approx 0, \quad i = 0, 1, 2, \dots, n-1 \quad (6.10)$$

$$\left(k_0^2 \mathbf{v}_0^T A_i^\beta \mathbf{v}_0 + k_0 b_i^\beta \mathbf{v}_0 \right) + \left(2k_0 \mathbf{v}_0^T A_i^\beta + b_i^\beta \right) V_5 \delta\mathbf{k} \approx 0, \quad i = 0, 1, 2, \dots, n-1 \quad (6.11)$$

At this point, we have $2n$ equations and 6 unknowns, k_0 and $\delta\mathbf{k}$. The last $2n - 1$ equations can be written in the compact form

$$\left(k_0^2 C_{2n-1} + k_0 B_{2n-1} \mathbf{v}_0\right) + (k_0 D_{2n-1} + B_{2n-1}) V_5 \delta\mathbf{k} = N + M \delta\mathbf{k} \approx 0 \quad (6.12)$$

where

$$B_{2n-1} = \begin{bmatrix} b_0^\beta \\ b_1^\alpha \\ \vdots \\ b_{n-1}^\alpha \\ b_{n-1}^\beta \end{bmatrix}, \quad C_{2n-1} = \begin{bmatrix} \mathbf{v}_0^T A_0^\beta \mathbf{v}_0 \\ \mathbf{v}_0^T A_1^\alpha \mathbf{v}_0 \\ \vdots \\ \mathbf{v}_0^T A_{n-1}^\alpha \mathbf{v}_0 \\ \mathbf{v}_0^T A_{n-1}^\beta \mathbf{v}_0 \end{bmatrix}, \quad D_{2n-1} = \begin{bmatrix} 2\mathbf{v}_0^T A_0^\beta \\ 2\mathbf{v}_0^T A_1^\alpha \\ \vdots \\ 2\mathbf{v}_0^T A_{n-1}^\alpha \\ 2\mathbf{v}_0^T A_{n-1}^\beta \end{bmatrix} \quad (6.13)$$

Applying a pseudo-inverse, least squares method, the value of $\delta\mathbf{k}$ that minimizes the sum of the squares of the residuals of the last $2n - 1$ equations is written as

$$\begin{aligned} \delta\mathbf{k} &= -\left(M^T M\right)^{-1} M^T N \\ &= -\left[V_5^T (k_0 D_{2n-1} + B_{2n-1})^T (k_0 D_{2n-1} + B_{2n-1}) V_5\right]^{-1} \\ &\quad \times V_5^T (k_0 D_{2n-1} + B_{2n-1})^T \left(k_0^2 C_{2n-1} + k_0 B_{2n-1} \mathbf{v}_0\right) \end{aligned} \quad (6.14)$$

This solution for $\delta\mathbf{k}$ can then be substituted into Eq. 6.10 to produce a single scalar equation in terms of the last unknown k_0

$$\left(k_0^2 \mathbf{v}_0^T A_0^\alpha \mathbf{v}_0 + k_0 b_0^\alpha \mathbf{v}_0\right) - \left(2k_0 \mathbf{v}_0^T A_0^\alpha + b_0^\alpha\right) V_5 \left(M^T M\right)^{-1} M^T N \approx 0 \quad (6.15)$$

Dividing both sides by $\left(k_0^2 \mathbf{v}_0^T A_0^\alpha \mathbf{v}_0 + k_0 b_0^\alpha \mathbf{v}_0\right)$ produces

$$1 - \frac{(k_0 \mathbf{d}_0 + b_0^\alpha) V_5 \left(M^T M\right)^{-1} M^T N}{(k_0^2 c_0 + k_0 b_0^\alpha \mathbf{v}_0)} \approx 0 \quad (6.16)$$

where

$$c_0 = \mathbf{v}_0^T A_0^\alpha \mathbf{v}_0 \quad (6.17)$$

$$\mathbf{d}_0 = 2\mathbf{v}_0^T A_0^\alpha \quad (6.18)$$

Letting

$$P = (k_0 \mathbf{d}_0 + b_0^\alpha) V_5 \quad (6.19)$$

$$Q = M^T M = V_5^T (k_0 D_{2n-1} + B_{2n-1})^T (k_0 D_{2n-1} + B_{2n-1}) V_5 \quad (6.20)$$

$$R = \frac{M^T N}{k_0^2 c_0 + b_0^\alpha k_0 \mathbf{v}_0} = V_5^T (k_0 D_{2n-1} + B_{2n-1})^T (k_0^2 C_{2n-1} + k_0 B_{2n-1} \mathbf{v}_0) \quad (6.21)$$

The same simplification process is followed as shown in the previous derivation, and it yields

$$\text{Det} \left[(k_0^2 c_0 + k_0 b_0^\alpha \mathbf{v}_0) M^T M - M^T N (k_0 \mathbf{d}_0 + b_0^\alpha) V_5 \right] = 0 \quad (6.22)$$

which can be simplified to

$$\begin{aligned} \text{Det} [V_5^T \{ (k_0 D_{2n-1} + B_{2n-1})^T [(k_0^2 c_0 + k_0 b_0^\alpha \mathbf{v}_0) (k_0 D_{2n-1} + B_{2n-1}) \\ - (k_0^2 C_{2n-1} + k_0 B_{2n-1} \mathbf{v}_0) (k_0 \mathbf{d}_0 + b_0^\alpha)] \} V_5] = 0 \end{aligned} \quad (6.23)$$

A single k_0 can be factored out of this equation to arrive at

$$\begin{aligned} \text{Det} [V_5^T \{ (k_0 D_{2n-1} + B_{2n-1})^T [(k_0 c_0 + b_0^\alpha \mathbf{v}_0) (k_0 D_{2n-1} + B_{2n-1}) \\ - (k_0 C_{2n-1} + B_{2n-1} \mathbf{v}_0) (k_0 \mathbf{d}_0 + b_0^\alpha)] \} V_5] = 0 \end{aligned} \quad (6.24)$$

This results in a 15th-order polynomial (maximum) in k_0 . This means that there are a maximum of 15 roots to the above polynomial equation. Since the order of the polynomial equation is often less than 15, there are often less than the maximum amount of roots. Again, the roots of this polynomial are substituted back into Eq. 6.14 to find $\delta \mathbf{k}$. The solution for the initial relative state is determined from Eq. 6.6

$$\mathbf{X}_0 = k_0 \mathbf{v}_0 + V_5 \delta \mathbf{k} \quad (6.25)$$

6.2 Improving the IROD Solution, $N > 3$ Observations

Once an approximate solution to the IROD problem is obtained, a simple iterative algorithm can be applied to improve the solution. The approximate solution in Eq. 6.25 will not exactly satisfy the $2n$ quadratic equations in Eq. 6.7 because the problem is overdetermined (and there are residuals) and, more importantly, the second-order terms in $\delta\mathbf{k}$ have been neglected. The objective of the following iterative scheme is to recover these second-order terms and determine a more accurate solution to the $2n$ quadratic equations using the approximate solution as a starting point. It is important to point out that although an exact solution is typically found in a few iterations, this will not be the best solution to the original 2-body relative motion problem (with or without J_2). It is only the best solution to the problem modeled by the second-order measurement equations and the linearized equations of relative motion in spherical coordinates.

The objective function to be minimized can be written as a sum

$$J = \sum_{i=1}^n \left(\mathbf{X}_0^T A_i^\alpha \mathbf{X}_0 + B_i^\alpha \mathbf{X}_0 \right)^2 + \sum_{i=1}^n \left(\mathbf{X}_0^T A_i^\beta \mathbf{X}_0 + B_i^\beta \mathbf{X}_0 \right)^2 \quad (6.26)$$

To find the minimum, take the partial of J with respect to \mathbf{X}_0 and set it to zero

$$\begin{aligned} \frac{\partial J}{\partial \mathbf{X}_0} &= \sum_{i=1}^n \left(\mathbf{X}_0^T A_i^\alpha \mathbf{X}_0 + B_i^\alpha \mathbf{X}_0 \right) \left[2 (A_i^\alpha)^T \mathbf{X}_0 + (B_i^\alpha)^T \right] \\ &+ \sum_{i=1}^n \left(\mathbf{X}_0^T A_i^\beta \mathbf{X}_0 + B_i^\beta \mathbf{X}_0 \right) \left[2 (A_i^\beta)^T \mathbf{X}_0 + (B_i^\beta)^T \right] = 0 \end{aligned} \quad (6.27)$$

Starting with the initial approximate solution \mathbf{X}_0^* , let the best solution be given by $\mathbf{X}_0 = \mathbf{X}_0^* + \delta\mathbf{X}_0$. Substitute \mathbf{X}_0 into Eq. 6.27 which yields

$$\begin{aligned} 0 &= \sum_{i=1}^n \left((\mathbf{X}_0^* + \delta\mathbf{X}_0)^T A_i^\alpha (\mathbf{X}_0^* + \delta\mathbf{X}_0) + B_i^\alpha (\mathbf{X}_0^* + \delta\mathbf{X}_0) \right) \\ &\times \left[2 (A_i^\alpha)^T (\mathbf{X}_0^* + \delta\mathbf{X}_0) + (B_i^\alpha)^T \right] \\ &+ \sum_{i=1}^n \left((\mathbf{X}_0^* + \delta\mathbf{X}_0)^T A_i^\beta (\mathbf{X}_0^* + \delta\mathbf{X}_0) + B_i^\beta (\mathbf{X}_0^* + \delta\mathbf{X}_0) \right) \\ &\times \left[2 (A_i^\beta)^T (\mathbf{X}_0^* + \delta\mathbf{X}_0) + (B_i^\beta)^T \right] \end{aligned} \quad (6.28)$$

which, after neglecting second-order terms in $\delta\mathbf{X}_0$, simplifies to

$$\begin{aligned}
0 &= \sum_{i=1}^n \left(\mathbf{X}_0^{*T} A_i^\alpha \mathbf{X}_0^* + B_i^\alpha \mathbf{X}_0^* \right) \left[2(A_i^\alpha)^T \mathbf{X}_0^* + (B_i^\alpha)^T \right] \\
&+ \sum_{i=1}^n \left(\mathbf{X}_0^{*T} A_i^\beta \mathbf{X}_0^* + B_i^\beta \mathbf{X}_0^* \right) \left[2(A_i^\beta)^T \mathbf{X}_0^* + (B_i^\beta)^T \right] \\
&+ \sum_{i=1}^n \left[2 \left(\mathbf{X}_0^{*T} A_i^\alpha \mathbf{X}_0^* + B_i^\alpha \mathbf{X}_0^* \right) (A_i^\alpha)^T + \left(2(A_i^\alpha)^T \mathbf{X}_0^* + B_i^\alpha \right) \left(2\mathbf{X}_0^{*T} A_i^\alpha + B_i^\alpha \right) \right] \delta\mathbf{X}_0 \\
&+ \sum_{i=1}^n \left[2 \left(\mathbf{X}_0^{*T} A_i^\beta \mathbf{X}_0^* + B_i^\beta \mathbf{X}_0^* \right) (A_i^\beta)^T + \left(2(A_i^\beta)^T \mathbf{X}_0^* + B_i^\beta \right) \left(2\mathbf{X}_0^{*T} A_i^\beta + B_i^\beta \right) \right] \delta\mathbf{X}_0
\end{aligned} \tag{6.29}$$

Or $0 = N + M\delta\mathbf{X}_0$ where M and N are defined as

$$\begin{aligned}
N &= \sum_{i=1}^n \left(\mathbf{X}_0^{*T} A_i^\alpha \mathbf{X}_0^* + B_i^\alpha \mathbf{X}_0^* \right) \left[2(A_i^\alpha)^T \mathbf{X}_0^* + (B_i^\alpha)^T \right] \\
&+ \sum_{i=1}^n \left(\mathbf{X}_0^{*T} A_i^\beta \mathbf{X}_0^* + B_i^\beta \mathbf{X}_0^* \right) \left[2(A_i^\beta)^T \mathbf{X}_0^* + (B_i^\beta)^T \right]
\end{aligned} \tag{6.30}$$

$$\begin{aligned}
M &= \sum_{i=1}^n \left[2 \left(\mathbf{X}_0^{*T} A_i^\alpha \mathbf{X}_0^* + B_i^\alpha \mathbf{X}_0^* \right) (A_i^\alpha)^T \right. \\
&+ \left. \left(2(A_i^\alpha)^T \mathbf{X}_0^* + B_i^\alpha \right) \left(2\mathbf{X}_0^{*T} A_i^\alpha + B_i^\alpha \right) \right] \\
&+ \sum_{i=1}^n \left[2 \left(\mathbf{X}_0^{*T} A_i^\beta \mathbf{X}_0^* + B_i^\beta \mathbf{X}_0^* \right) (A_i^\beta)^T \right. \\
&+ \left. \left(2(A_i^\beta)^T \mathbf{X}_0^* + B_i^\beta \right) \left(2\mathbf{X}_0^{*T} A_i^\beta + B_i^\beta \right) \right]
\end{aligned} \tag{6.31}$$

The value of $\delta\mathbf{X}_0$ that best satisfies these equations is

$$\delta\mathbf{X}_0 = -M^{-1}N \tag{6.32}$$

The value of $\mathbf{X}_0 = \mathbf{X}_0^* + \delta\mathbf{X}_0$ is then used as a starting point for the next iteration, i.e., set $\mathbf{X}_0 = \mathbf{X}_0 + \delta\mathbf{X}_0$ and repeat Eq. 6.32. This is equivalent to a simple, semi-analytic, nonlinear least-squares procedure applied to a set of $2n$ equations in 6 unknowns. The

algorithm is simple and typically converges in a few iterations.

6.3 IROD Performance Tables (Simplified Models)

To verify that the IROD algorithm is able to extract the initial relative states from LOS measurements, the algorithm is tested for a range of relative motion cases. The IROD algorithm above is derived using linearized dynamics and second-order measurement equations. To test that the IROD algorithm is working properly, LOS measurements are generated using the same environment of linearized dynamics and second-order measurement equations and then inserted into the IROD algorithm. IROD performance tables are generated for a variety of relative motion cases, inclinations, eccentricities and number of observations. The range of cases are shown below where the variables can be listed as:

- Trajectory type - Leader-Follower, Flyby, Football Orbits
- Downrange Separation: 0.5 km, 5 km, 50 km, 500 km
- J_2 Perturbations are ON
- Cross-track Separation: 0%, 10%
- Iterative Improvement Algorithm (ON or OFF)
- Orbital Elements - inclination (0° , 10° , 45° , 60°) and eccentricity (0, 0.01, 0.1)

The final time remains the same for all number of observations, $T_f = 3000 \text{ sec}$, but the time between measurements changes inversely proportional to the number of measurements. For $N = 4$, the measurement time interval is $\Delta t = 1000 \text{ sec}$, for $N = 13$ the measurement time interval is $\Delta t = 250 \text{ sec}$ and for $N = 25$ the measurement time interval is $\Delta t = 125 \text{ sec}$. The propagation time step is 10 sec for the $N = 4$ and $N = 13$ measurement cases and 5 sec for the $N = 25$ measurement cases. Reducing the time interval from 10 sec to 5 sec for the $N = 4$ and $N = 13$ measurement cases has no effect on the position errors of the IROD algorithm.

Table 6.1: Percent Position Errors, Simplified Models, Leader-Follower, $N = 4$, $\Delta t = 1000 \text{ sec}$, $\Delta z = 0\%$

inc	Dwn. Sep.	$e = 0$			$e = 0.01$			$e = 0.1$		
		Num.	IROD	Q	Num.	IROD	Q	Num.	IROD	Q
0°	0.5 km	2	2.7e-4	2.9e-11	2	1.6e-3	6.1e-9	1	1.6e-2	8.2e-9
	5 km	4	3.2e-2	2.5e-11	2	6.3e-3	5.3e-10	1	1.6e-1	9.6e-10
	50 km	4	4.8	4.8	2	5.4	5.4	5	1.2	1.7e-10
	500 km	4	2.6	2.0e-12	4	20	20	2	9.4e-1	3.4e-12
10°	0.5 km	2	3.2e-3	8.8e-9	2	1.9e-3	1.9e-3	1	1.7e-2	1.7e-2
	5 km	2	1.8	1.5	2	2.1e-3	2.1e-3	1	1.6e-1	1.6e-1
	50 km	4	14	14	2	3.6	3.6	1	1.3	1.3
	500 km	4	10	10	4	6.3	6.4	2	1.5	1.8
45°	0.5 km	2	1.5e-3	7.8e-7	1	3.4e-3	3.4e-3	1	1.2e-2	1.2e-2
	5 km	2	1.0e-1	1e-1	1	1.4e-2	1.4e-2	1	1.2e-1	1.2e-1
	50 km	4	1.3	1.3	1	5.4e-1	5.4e-1	1	1.0	1.0
	500 km	3	7.9	7.8	3	6.9	7.4	1	4.7	4.7
60°	0.5 km	4	2.7e-3	2.1e-7	3	4.0e-3	4.0e-3	1	1.3e-2	1.3e-2
	5 km	4	3.4e-2	3.4e-2	3	2.6e-2	2.6e-2	1	1.3e-1	1.3e-1
	50 km	6	3.1	3.1	3	5.4e-1	5.4e-1	1	1.2	1.2
	500 km	6	18	17	6	13	13	1	5.6	6.1

6.3.1 $N=4$ Observations, Simplified Models

For the Leader-Follower cases shown, the IROD algorithm works very well. The measurements are calculated using linearized dynamics and the measurement equations are expanded to second order. This is a simplified framework to validate the IROD algorithm in the same framework in which the IROD solution was derived. It is interesting to note that in many cases, as the downrange separation increases, the percent position error also increases.

The IROD algorithm is able to find good solutions for the above Flyby cases. Again, in this simplified framework, the IROD algorithm is able to accurately extract the correct relative states and get answers that yield low percent position errors.

For the Football cases shown in the table above, the IROD algorithm is able to find good solutions for a variety of orbital inclinations, eccentricities and downrange separations. These results validate that the IROD algorithm works well in the simplified framework (linearized dynamics and 2nd-order measurement equations) from which is was derived.

For the cases shown above where $N = 4$, the IROD algorithm performed very well. The IROD algorithm was able to find the correct relative motion states in virtually every case

Table 6.2: Percent Position Errors, Simplified Models, Flyby, $N = 4$, $\Delta t = 1000 \text{ sec}$, $\Delta z = 0\%$

inc	Dwn. Sep.	$e = 0$			$e = 0.01$			$e = 0.1$		
		Num.	IROD	Q	Num.	IROD	Q	Num.	IROD	Q
0°	0.5 km	1	3.7e-6	8.1e-10	1	1.3e-4	9.5e-9	1	1.3e-3	1.4e-8
	5 km	5	6.6e-5	6.2e-10	5	1.3e-3	1.0e-9	5	1.3e-1	6.7e-11
	50 km	5	3.5e-3	3.8e-11	5	1.5e-2	9.2e-11	5	1.3e-1	1.3e-10
	500 km	5	3.7e-1	3.3e-12	5	4.2e-1	1.0e-11	5	1.0	4.8e-12
10°	0.5 km	1	3.2e-4	3.2e-4	1	9.4e-5	9.4e-5	1	1.7e-3	1.7e-3
	5 km	1	3.6e-3	3.6e-3	1	1.3e-3	1.3e-3	1	1.6e-2	1.6e-2
	50 km	1	7.8e-2	7.8e-2	1	5.1e-2	5.2e-2	1	1.4e-1	1.4e-1
	500 km	1	5.7	5.4	1	4.6	5.5	1	2.9e-1	2.6e-1
45°	0.5 km	1	1.1e-3	1.1e-3	1	8.8e-4	8.8e-4	1	1.2e-3	1.2e-3
	5 km	1	1.1e-2	1.1e-2	1	8.9e-3	8.9e-3	1	1.2e-2	1.2e-2
	50 km	1	1.2e-1	1.2e-1	1	1.0e-1	1.0e-1	1	1.1e-1	1.1e-1
	500 km	1	2.4	2.5	1	2.2	2.2	2	2.2	2.2
60°	0.5 km	1	2.3e-3	2.3e-3	1	2.1e-3	2.1e-3	1	2.5e-4	2.5e-4
	5 km	1	2.3e-2	2.3e-2	1	2.1e-2	2.1e-2	1	2.8e-3	2.8e-3
	50 km	1	2.5e-1	2.5e-1	1	2.4e-1	2.4e-1	1	5.8e-2	5.9e-2
	500 km	1	4.8	4.9	1	4.8	4.9	2	11	11

Table 6.3: Percent Position Errors, Simplified Models, Football, $N = 4$, $\Delta t = 1000 \text{ sec}$, $\Delta z = 0\%$

inc	Dwn. Sep.	$e = 0$			$e = 0.01$			$e = 0.1$		
		Num.	IROD	Q	Num.	IROD	Q	Num.	IROD	Q
0°	0.5 km	1	9.4e-2	9.7e-9	1	7.3e-2	5.1e-1	1	2.3e-2	7.0e-9
	5 km	1	9.2e-1	3.9e-10	1	7.2e-1	4.3e-9	1	2.3e-1	6.5e-10
	50 km	1	7.1	8.8e-11	1	5.8	3.0e-10	1	2.0	1.8e-10
	500 km	6	27	58	6	25	18	6	21	19
10°	0.5 km	1	9.6e-2	9.6e-2	1	7.3e-2	7.3e-2	1	1.8e-2	1.8e-2
	5 km	1	9.4e-1	9.3e-1	1	7.2e-1	7.2e-1	1	1.9e-1	1.9e-1
	50 km	1	7.3	7.3	1	5.8	5.8	1	1.8	1.8
	500 km	2	15	20	2	12	17	2	11	9.1
45°	0.5 km	1	1.5e-1	1.5e-1	1	1.1e-1	1.1e-1	1	3.1e-2	3.1e-2
	5 km	1	1.5	1.5	1	1.1	1.1	1	3.1e-1	3.1e-1
	50 km	1	13	13	1	10	10	1	2.9	2.9
	500 km	2	7.9	11	2	7.1	10	2	3.6	5e-1
60°	0.5 km	1	1.4e-1	1.4e-1	1	1.1e-1	1.1e-1	1	2.7e-2	2.7e-2
	5 km	1	1.4	1.4	1	1.1	1.1	1	2.6e-1	2.6e-1
	50 km	1	13	13	1	10	10	1	2.5	2.5
	500 km	3	20	26	3	18	24	1	4	10

Table 6.4: Percent Position Errors, Simplified Models, Leader-Follower, $N = 13$, $\Delta t = 250 \text{ sec}$, $\Delta z = 0\%$

inc	Dwn. Sep.	$e = 0$			$e = 0.01$			$e = 0.1$		
		Num.	IROD	Q	Num.	IROD	Q	Num.	IROD	Q
0°	0.5 km	2	2.5e-4	2.2e-11	2	1.3e-3	5.9e-9	2	2.9e-2	4.8e-11
	5 km	4	2.9e-2	3.3e-11	2	4.2e-3	2.5e-10	2	3.0e-1	1.e-10
	50 km	4	2.8	2.8	2	7.3	7.3	2	3.9	7.4e-11
	500 km	4	20	2.1e-12	4	18	2.1e-12	2	6.0	2.6e-12
10°	0.5 km	6	1.2e-3	3.1e-8	6	1.4e-3	1.8e-8	2	1.0e-1	1.3e-8
	5 km	4	1.7e-1	1.7e-9	6	4.4e-3	1.9e-9	2	1.2	2.8e-9
	50 km	4	7.1	7.1	8	1.8	1.8	2	10	2.1e-10
	500 km	8	19	20	8	9.4	5.6e-1	4	8.4	2.0e-12
45°	0.5 km	6	3.2e-4	2.7e-7	6	1.1e-3	1.9e-7	2	8.8e-3	2.8e-9
	5 km	8	8.0e-2	1.4e-8	6	2.6e-2	1.0e-8	2	9.0e-2	5.8e-12
	50 km	7	8.2e-1	7.8e-10	6	1.0	1.3e-9	2	26	1.2e-11
	500 km	7	4.5	5.8e-12	9	72	1.5e-11	2	7.2	6.7
60°	0.5 km	6	3.5e-3	1.4e-7	4	1.2e-3	4.4e-8	2	2.0e-3	1.5e-9
	5 km	6	1.2e-1	7.6e-8	4	1.8e-2	7.9e-10	2	2.0e-2	5.8e-10
	50 km	8	5.0e-1	4.3e-10	4	6.9	3.2e-11	2	1.9e-1	4.0e-11
	500 km	11	3.1e2	1.6e-12	11	3.6e2	1.8e-11	2	2.2e-1	2.3e-12

and the percent position errors are tabulated to show how far off the best IROD solution was to the true relative motion states. The number of solutions are also tabulated, though there is no correlataion between the number of solutions and the accuracy of the IROD solutions.

6.3.2 N=13 Observations, Simplified Models

The IROD algorithm is also tested when more observations are taken ($N = 13$) but the final time remains constant at $T_{final} = 3000 \text{ sec}$. These results show that the IROD solution performs well when more than three or four measurements are taken.

The Leader-Follower cases above show that the IROD solution is able to extract the correct solution when $N = 13$. With more measurements, the number of polynomial equations increases and the number of feasible roots and consequentially, solutions, also increases.

The IROD algorithm is able to find good solutions for the flyby cases when $N = 13$. For these flyby cases, an increase in separation yields to a better IROD solution and thus lower percent position errors.

Table 6.5: Percent Position Errors, Simplified Models, Flyby, $N = 13$, $\Delta t = 250 \text{ sec}$, $\Delta z = 0\%$

inc	Dwn. Sep.	$e = 0$			$e = 0.01$			$e = 0.1$		
		Num.	IROD	Q	Num.	IROD	Q	Num.	IROD	Q
0°	0.5 km	1	8.8e-7	2.6e-9	3	1.2e-4	6.1e-9	1	1.7e-3	9.9e-9
	5 km	5	3.7e-5	5.5e-10	5	1.2e-3	6.3e-10	5	1.7e-2	5.6e-11
	50 km	5	5.0e-3	7.4e-11	5	1.6e-2	3.7e-11	5	1.7e-1	6.2e-11
	500 km	7	5.5e-1	5.6e-12	5	6.3e-1	8.5e-12	5	1.8	5.7e-3
10°	0.5 km	1	2.4e-3	8.8e-9	1	2.4e-3	5.1e-9	1	2.8e-3	1.0e-7
	5 km	1	2.3e-2	5.5e-10	1	2.3e-2	1.1e-9	1	2.7e-2	1.3e-8
	50 km	5	1.3e-1	2.2e-10	5	1.5e-1	2.0e-10	5	2.0e-1	1.5e-9
	500 km	9	2.8e2	9.7e-12	9	3.2	1.1e-11	5	2.0	7.3e-11
45°	0.5 km	1	9.6e-3	2.7e-9	1	1e-2	7.0e-8	2	2.9e-2	1.2e-10
	5 km	1	9.5e-2	6.1e-9	1	1.0e-1	5.3e-9	2	3.0e-1	5.4e-10
	50 km	5	8.5e-1	6.5e-11	5	9.2e-1	5.0e-10	2	3.2	2.5e-10
	500 km	5	4.3	1.0e-11	5	4.6	2.8e-11	2	1.6	6.1e-11
60°	0.5 km	2	1.4e5	1.9e-9	2	1.4e5	8.3e-9	2	3.1e-3	1.3e-8
	5 km	2	4.2e-2	5.8e-10	2	4.1e-2	1.6e-10	2	3.1e-2	1.5e-9
	50 km	2	1.2e3	4.0e-11	2	1.3e3	9.4e-11	2	1.9e3	1.6e-10
	500 km	2	6.8e-1	9.7e-12	2	5.1	5.8e-12	2	7.9e-1	2.6e-11

Table 6.6: Percent Position Errors, Simplified Models, Football, $N = 13$, $\Delta t = 250 \text{ sec}$, $\Delta z = 0\%$

inc	Dwn. Sep.	$e = 0$			$e = 0.01$			$e = 0.1$		
		Num.	IROD	Q	Num.	IROD	Q	Num.	IROD	Q
0°	0.5 km	2	3.3e-2	2.8e-9	2	3.5e-2	2.9e-9	2	9.0e-2	2.3e-10
	5 km	6	3.3e-1	2.5e-10	6	3.5e-1	2.2e-10	6	9.0e-1	4.3e-11
	50 km	6	3.1	7.1e-11	6	3.3	6.5e-11	6	8.5	1.7e-2
	500 km	6	19	1.4e-12	8	1.4e2	4.0e-12	6	26	24
10°	0.5 km	4	1.1	2.0e-9	3	7e-1	9.9e-9	3	4.3e-2	5.2e-8
	5 km	4	180	1.9e-9	3	8.1	1.7e-10	3	4.4e-1	4.8e-9
	50 km	6	71	1.6e-10	6	48	1.3e-10	1	5.4	6.0e-10
	500 km	8	16	1.9e-11	8	16	4.4e-11	8	11	1.1e-10
45°	0.5 km	6	2.5e4	5.7e-9	4	1.3e4	1.1e-8	3	7.1e-2	4.1e-9
	5 km	6	5.8e3	2.7e-10	6	2.2e3	7.1e-10	3	7e-1	2.9e-10
	50 km	10	7.4	2.4e-11	10	1.4e2	1e-10	5	5.5	2.8e-11
	500 km	6	24	6.8e-12	6	25	1.8e-11	6	26	4.1e-12
60°	0.5 km	6	4.3e-2	3.3e-11	6	4.9e-2	8.6e-10	3	1.5e-1	6.2e-9
	5 km	10	2.8e3	1.4e-10	10	4.9e-1	1.7e-10	3	1.4	6.4e-10
	50 km	10	4.0	4.2e-12	10	4.6	1.1e-11	5	8.8	4.6e-11
	500 km	8	31	6.5e-12	8	32	9.6e-12	6	35	34

Table 6.7: Percent Position Errors, Simplified Models, Leader-Follower, $N = 25$, $\Delta t = 125 \text{ sec}$, $\Delta z = 0\%$

inc	Dwn. Sep.	$e = 0$			$e = 0.01$			$e = 0.1$		
		Num.	IROD	Q	Num.	IROD	Q	Num.	IROD	Q
0°	0.5 km	2	2.4e-4	3.3e-11	2	1.3e-3	1.6e-8	2	2.e-2	1.0e-8
	5 km	4	2.9e-2	2.8e-11	2	3.5e-3	4.7e-9	2	2.2e-1	2.2e-1
	50 km	4	2.5	2.5	2	6.9	6.9	2	2.7	1.1e-10
	500 km	4	19	2.9e-12	4	17	5.7e-12	2	7.8	6.4e-12
10°	0.5 km	6	9.6e-4	3.6e-8	6	1.4e-3	2.6e-8	2	4.4e-2	1.9e-8
	5 km	4	1.8e-1	3.1e-9	6	4.4e-3	5.1e-9	2	4.7e-1	1.0e-9
	50 km	4	7.1	7.0	8	1.4	1.4e-12	2	10	4.8e-10
	500 km	8	19	21	8	8.2	3.4e-1	4	7.6	1.6e-11
45°	0.5 km	6	3.2e-4	2.4e-7	6	1.1e-3	2.1e-7	2	7.0e-3	3.2e-9
	5 km	8	7.7e-2	5.9e-9	6	2.4e-2	2.3e-8	2	7.1e-2	1.4e-10
	50 km	7	7.9e-1	8.5e-10	6	1.0	1.7e-9	2	8.8e-1	1.9e-11
	500 km	9	4.4	1.8e-11	9	4.7	1.8e-11	2	9.8	9.3
60°	0.5 km	6	3.5e-3	1.7e-7	6	1.2e-3	9.1e-9	2	1.8e-3	3.9e-9
	5 km	6	1.1e-1	7.6e-10	6	1.7e-2	9.4e-9	2	1.8e-2	2.7e-10
	50 km	8	4.7e-1	1.9e-9	4	6.1	1.4e-11	2	1.8e-1	1.5e-11
	500 km	11	3.0e2	3.0e-12	11	3.5	4.1e-13	2	48	3.2e-12

For the Football cases tabulated above, the IROD algorithm is able to find good solutions for $N = 13$ observations. For many of the cases, an increase in downrange separation yields a decrease in the percent position error. Also, there are several cases where the initial IROD solution is bad but after implementing the iterative improvement method, the IROD solution is much better. The iterative improvement method reduces the residual of the original quadratic equation.

For these cases, increasing the number of measurements from four to thirteen still yields good results and the IROD algorithm is able to find good solutions for the relative motion states.

6.3.3 $N=25$ Observations, Simplified Models

The IROD algorithm is also tested when more observations are taken ($N = 25$) but the final time remains constant at $T_{final} = 3000 \text{ sec}$ (the time between measurements gets smaller). These results show that the IROD solution performs well when 25 measurements are taken.

For the Leader-Follower cases shown above where $N = 25$, the IROD algorithm is

Table 6.8: Percent Position Errors, Simplified Models, Leader-Follower, $N = 25$, $\Delta t = 125 \text{ sec}$, $\Delta z = 0\%$

inc	Dwn. Sep.	$e = 0$			$e = 0.01$			$e = 0.1$		
		Num.	IROD	Q	Num.	IROD	Q	Num.	IROD	Q
0°	0.5 km	1	1.3e-6	1.2e-8	1	1.2e-4	9.4e-9	1	1.8e-3	4.6e-9
	5 km	5	3.4e-5	1.2e-9	5	1.2e-3	6.4e-10	5	1.8e-2	2.9e-10
	50 km	5	5.1e-3	1.3e-10	5	1.6e-2	1.1e-10	5	1.8e-1	6.5e-11
	500 km	7	5.7e-11	1.3e-11	5	6.5e-1	8.4e-11	5	1.8	3.6e-3
10°	0.5 km	1	2.3e-3	3.9e-9	1	2.3e-3	1.2e-8	1	2.5e-3	1.3e-7
	5 km	1	2.2e-2	2.7e-11	1	2.2e-2	1.3e-9	1	2.4e-2	1.4e-8
	50 km	5	1.3e-1	1.8e-11	5	1.4e-1	2.7e-10	5	1.8e-1	2.1e-9
	500 km	9	4.8	2.1e-12	9	3.2	1.3e-11	5	2.2	1.1e-10
45°	0.5 km	1	9.9e-3	1.3e-8	1	1.0e-2	2.5e-8	2	1.9e-2	3.8e-9
	5 km	1	9.8e-2	1.8e-9	1	1.0e-1	6.2e-10	2	1.9e-1	2.1e-9
	50 km	5	8.8e-1	1.2e-10	5	9.6e-1	4.6e-11	2	1.9	9.2e-11
	500 km	5	4.2	1.2e-11	5	4.6	2.7e-12	2	2.6e-1	1.4e-11
60°	0.5 km	2	1.4e5	6.0e-9	2	4.0e-3	7.2e-9	2	2.1e5	1.5e-9
	5 km	2	4.1e-2	1.9e-11	2	4.1e-2	3.9e-10	2	3.0e-2	1.1e-10
	50 km	2	4.6e-1	8.6e-11	2	1.4e3	3.0e-11	2	2.0e3	4.6e-11
	500 km	2	5.8	2.3e-11	2	10	4.8e-12	2	4.5e-2	6.8e-12

able to find good solutions for the relative states. Even when the approximate solution to the IROD problem (the percent position error in the IROD column) is poor, the iterative improvement method can find a good solution with only a few iterations. With the linearized propagation and second-order measurement equations, varying the inclination or the eccentricity does not seem to effect the accuracy of the IROD solutions.

For the Flyby cases shown above, the IROD algorithm is able to consistently find an accurate estimate of the initial relative states when $N = 25$. Even though the approximate IROD estimates are good, the iterative improvement improves the estimate and reduces the percent position errors. Varying the inclination and eccentricity of the relative motion cases has no effect on the accuracy of the IROD solution.

For the Football cases shown above, the IROD algorithm is able to estimate the initial relative states very well. Out of all of these football cases, the IROD solution was not able to find a “good” solution in two cases (highlighted in blue). Even when the initial estimate of the IROD algorithm was bad (highlighted in red), the iterative improvement on the polynomial equations was able to get good IROD solutions.

This chapter showed the derivation of an IROD algorithm that is able to take more

Table 6.9: Percent Position Errors, Simplified Models, Leader-Follower, $N = 25$, $\Delta t = 125 \text{ sec}$, $\Delta z = 0\%$

inc	Dwn. Sep.	$e = 0$			$e = 0.01$			$e = 0.1$		
		Num.	IROD	Q	Num.	IROD	Q	Num.	IROD	Q
0°	0.5 km	2	2.7e-2	2.7e-9	2	2.9e-2	3.3e-9	4	5.7e-2	5.4e-9
	5 km	6	2.7e-1	3.8e-10	8	2.9e-1	4.4e-11	6	5.7e-1	1.1e-10
	50 km	6	2.5	4.3e-11	6	2.7	3.5e-11	6	5.4	1.8e-9
	500 km	6	16	2.8e-11	6	17	8.5e-2	6	24	22
10°	0.5 km	4	1.5e-1	2.9e-9	4	2.3e-1	4.8e-8	3	6.1e-2	6.2e-8
	5 km	4	1.4	1.6e-9	4	7.1e2	4.1e-9	3	3.2e3	6.6e-9
	50 km	6	8.9	1.7e-10	6	1.1e2	3.9e-10	3	7.8	8.7e-10
	500 km	8	18	1.2e-11	8	18	9.3e-11	8	13	1.3e-10
45°	0.5 km	4	4.0e-2	1.8e-9	4	4.4e-2	8.8e-10	4	3.4e4	5.6e-9
	5 km	8	3.3e3	1.0e-9	8	3.0e3	2.3e-10	4	1.4e2	4.1e-11
	50 km	10	3.0e2	3.2e-11	10	1.6e3	3.8e-11	10	3.3e2	4.5e-11
	500 km	6	23	2.0e-11	6	23	1.3e-11	6	24	1.5e-12
60°	0.5 km	4	2.5e-2	7.4e-9	4	2.7e-2	2.5e-10	4	1.7e4	5.5e-9
	5 km	10	2.5e-1	7.8e-10	8	2.7e-1	4.0e-11	8	7.5e-1	5.8e-10
	50 km	10	3.4e2	4.4e-11	10	3.4e2	3.1e-12	10	1.3e2	4.8e-11
	500 km	8	29	7.1e-12	8	29	1.6e-12	6	33	31

than three observations (more than six LOS angle measurements) and process them to get an estimate of the initial relative states. After the derivation of the approximate IROD algorithm, and iterative improvement scheme was derived that seeks to minimize the residual of the set of polynomial equations and account for the previously neglected second-order terms in the approximate IROD derivation. The $N > 3$ IROD algorithm was then tested for a variety of relative motion cases, eccentricities, inclinations, and number of measurements when the measurements are calculated using linearized propagation and second-order measurement equations. Testing the IROD algorithm in this simplified environment validates that the IROD algorithm is correctly estimating the initial estimates because it is being fed measurements from the same simplified environment from which the IROD algorithm was derived. The results show that the IROD algorithm is working properly and can estimate the initial relative states for a wide variety of relative motion cases.

CHAPTER 7

LOW EARTH ORBIT RESULTS

This chapter shows how the IROD algorithm performs when testing relative motion trajectories at LEO with nonlinear dynamics (2-body + J_2 perturbations) and the measurement equations are the exact nonlinear expressions for the LOS measurements. The results are presented in the same table format as in previous chapters. The number of measurements, cross-track separation, relative motion trajectories, downrange separation, inclination and eccentricity are all varied to provide a basis for how well the IROD algorithm performs in a number of different relative motion scenarios in LEO. The percent position errors of the IROD estimates of the initial relative states are presented for these cases.

7.1 N=4 Observations, Nonlinear Dynamics, $\Delta t = 1000 \text{ sec}$

The Leader-Follower cases with $N = 4$ observations, nonlinear dynamics, and nonlinear LOS measurement equations are shown in Table 7.1. In all the cases, the out-of-plane motion is small (only due to differential J_2). The time between measurements is $\Delta t = 1000 \text{ sec}$. The total measurement period is 3000 sec . It is seen that the IROD algorithm cannot accurately estimate the correct initial relative states. When the eccentricity or the inclination is large, the IROD algorithm struggles to find an estimate close to the true relative states. In several cases, the IROD algorithm is not able to even find a solution (marked with NS for No Solution). However, when the inclinations are small and the eccentricities are small, the IROD algorithm performs well and the percent position errors are low.

Table 7.2 shows the performance of the IROD algorithm when considering Flyby cases with nonlinear dynamics and nonlinear measurement equations. The Flyby cases performed better than the Leader-Follower cases in terms of percent position errors (the errors were lower). The Flyby cases performed well even at high eccentricities but not very well at

Table 7.1: Percent Position Errors, Nonlinear, Leader-Follower, $N = 4$, $\Delta t = 1000 \text{ sec}$, $\Delta z = 0\%$

inc	Dwn. Sep.	$e = 0$			$e = 0.01$			$e = 0.1$		
		Num.	IROD	Q	Num.	IROD	Q	Num.	IROD	Q
0°	0.5 km	2	2.0e-4	4.8e-4	2	1.0	1.0	1	25	25
	5 km	4	3.2e-2	1.3e-4	2	1.1	1.1	1	25	25
	50 km	4	4.8	4.8	2	9.5	9.5	1	22	23
	500 km	4	2.6	4.2e-2	4	20	20	2	12	13
10°	0.5 km	2	1.0e-1	1.0e-1	2	13	13	1	31	31
	5 km	4	1.0	8.1e-1	2	16	16	1	31	31
	50 km	4	11	11	2	1.0e-1	1.0e-1	1	28	28
	500 km	4	17	17	4	33	33	2	13	12
45°	0.5 km	2	11	11	0	NS	NS	1	72	72
	5 km	2	1.6	1.6	0	NS	NS	1	72	72
	50 km	4	41	41	2	35	35	1	73	73
	500 km	4	27	27	4	18	18	2	59	59
60°	0.5 km	4	31	31	2	1.8e6	1.4e6	0	NS	NS
	5 km	4	7.0	7.0	2	1.8e5	1.4e5	1	80	80
	50 km	4	52	52	4	51	51	1	82	82
	500 km	6	34	33	6	28	29	2	74	74

Table 7.2: Percent Position Errors, Nonlinear, Flyby, $N = 4$, $\Delta t = 1000 \text{ sec}$, $\Delta z = 0\%$

inc	Dwn. Sep.	$e = 0$			$e = 0.01$			$e = 0.1$		
		Num.	IROD	Q	Num.	IROD	Q	Num.	IROD	Q
0°	0.5 km	1	4.5	4.5	1	4.9	4.9	1	9.8	9.8
	5 km	5	4.5	4.5	5	4.9	4.9	5	9.8	9.8
	50 km	5	4.4	4.4	5	4.8	4.8	5	9.6	9.7
	500 km	5	3.3	3.3	5	3.6	4.0	5	8.1	9.0
10°	0.5 km	1	5.4	5.4	1	5.8	5.8	1	9.9	9.9
	5 km	1	5.4	5.4	1	5.8	5.8	1	9.9	9.9
	50 km	1	5.4	5.4	1	5.7	5.7	1	9.7	9.7
	500 km	1	10	9.3	1	9.4	8.9	1	9.1	9.1
45°	0.5 km	1	19	19	1	19	19	1	7.6	7.6
	5 km	1	18	18	1	19	19	1	7.6	7.6
	50 km	1	18	18	1	18	18	1	7.1	7.1
	500 km	1	16	16	1	16	16	1	3.3	3.3
60°	0.5 km	1	21	21	1	21	21	1	8.8	8.8
	5 km	1	21	21	1	21	21	1	9.0	9.0
	50 km	1	21	21	1	21	21	1	10	10
	500 km	1	18	18	1	17	17	1	22	22

Table 7.3: Percent Position Errors, Nonlinear, Football, $N = 4$, $\Delta t = 1000 \text{ sec}$, $\Delta z = 0\%$

inc	Dwn. Sep.	$e = 0$			$e = 0.01$			$e = 0.1$		
		Num.	IROD	Q	Num.	IROD	Q	Num.	IROD	Q
0°	0.5 km	1	8.2	8.3	1	13	13	1	25	25
	5 km	1	7.8	8.5	1	12	13	1	24	25
	50 km	1	5.0	10	1	9.8	14	1	23	24
	500 km	6	20	15	6	21	16	1	25	23
10°	0.5 km	1	7.7	7.7	1	12	12	1	24	24
	5 km	1	7.3	7.3	1	12	12	1	24	24
	50 km	1	4.7	4.7	1	9.5	9.5	1	23	23
	500 km	2	19	18	2	20	19	1	25	25
45°	0.5 km	1	22	22	1	26	26	1	33	33
	5 km	1	22	22	1	25	25	1	33	33
	50 km	1	18	18	1	22	22	1	32	32
	500 km	2	22	21	2	23	22	1	29	28
60°	0.5 km	1	57	57	1	60	60	1	63	63
	5 km	1	57	57	1	60	60	1	63	63
	50 km	1	55	55	1	58	58	1	63	63
	500 km	3	35	34	3	40	40	2	61	60

high inclination angles. In the Leader-Follower cases, there is no relative motion between the chief and deputy vehicle because they are at the same orbital radius and separated by a nearly constant true anomaly. In the Flyby cases, although they have the same initial downrange separation as the Leader-Follower cases, the deputy vehicle (the vehicle being observed) is moving *towards* the chief vehicle. So, the deputy vehicle is spending more time closer to the chief vehicle, thus more time in an environment that is better approximated as linear. The linearized equations in the IROD algorithm are able to more accurately estimate the initial relative states of these Flyby cases when compared to the Leader-Follower cases.

Table 7.3 shows the IROD performance for a range of Football cases using nonlinear dynamics and nonlinear measurement equations. Similar to the Leader-Follower cases, as the eccentricity and inclination of the two satellites increases, the IROD algorithm performs poorly, unable to get a good estimate of the relative states.

The cases above are repeated with an out-of-plane separation equal to 10% of the initial separation (i.e. $\Delta z = 10\%$). Tables 7.4-7.6 show the results for the Leader-Follower, Flyby, and Football orbit cases, respectively.

For the Leader-Follower cases in Table 7.4, an increase in the cross-track motion does

Table 7.4: Percent Position Errors, Nonlinear, Leader-Follower, $N = 4$, $\Delta t = 1000 \text{ sec}$, $\Delta z = 10\%$

inc	Dwn. Sep.	$e = 0$			$e = 0.01$			$e = 0.1$		
		Num.	IROD	Q	Num.	IROD	Q	Num.	IROD	Q
0°	0.5 km	2	2.1e-2	2.0e-2	2	1.6	1.6	1	27	27
	5 km	2	7.5e-2	9.5e-2	2	1.9	1.9	1	26	26
	50 km	4	4.0	4.0	2	6.7	6.7	1	22	22
	500 km	4	3.5	4.0	4	22	22	2	23	23
10°	0.5 km	2	8.9e-1	8.9e-1	2	8.6	8.6	1	39	39
	5 km	2	2.8	2.8	2	9.2	9.2	1	39	39
	50 km	4	6.2	6.2	2	9.5	9.4	1	35	35
	500 km	4	11	11	4	15	14	2	12	12
45°	0.5 km	2	11	11	0	NS	NS	1	76	76
	5 km	2	21	21	0	NS	NS	1	76	76
	50 km	2	45	45	2	32	32	1	77	77
	500 km	4	28	29	4	18	19	2	66	66
60°	0.5 km	4	25	25	2	1.7e6	1.3e6	0	NS	NS
	5 km	4	8.1	8.2	2	1.7e5	1.2e5	1	82	82
	50 km	4	50	50	4	48	48	1	83	83
	500 km	6	43	44	6	29	29	2	83	83

not seem to improve the IROD solutions. At high inclinations and high eccentricities, the IROD algorithm is again unable to find accurate solutions.

For the Flyby cases in Table 7.5, an increase in the cross-track motion results in some increase in the percent position errors. However, the IROD algorithm is able to get good reasonable estimates for high eccentricity cases, and for high inclination cases.

For the Football cases in Table 7.6, the IROD algorithm once again cannot find good estimates for the relative states at high inclinations and eccentricities. At low inclinations and low eccentricities ($i = 0 - 10^\circ$, $e = 0 - 0.01$), the IROD algorithm performs well.

The IROD algorithm has a difficult time at higher inclinations because of the unique reference orbit that is chosen to accommodate the J_2 perturbations. In previous formulations of linearized relative motion equations without the J_2 perturbation, the reference orbit is the chief orbit. This is not the case in the linearized equations with J_2 that are used in the IROD algorithm. Since the acceleration due to the J_2 perturbation is a function of the latitude of the spacecraft with respect to the equatorial plane, the inclination of the chief and deputy vehicle now affects the relative satellite motion of these objects where before the inclination had no affect on the relative motion. In short, as the inclination of the neigh-

Table 7.5: Percent Position Errors, Nonlinear, Flyby, $N = 4$, $\Delta t = 1000 \text{ sec}$, $\Delta z = 10\%$

inc	Dwn. Sep.	$e = 0$			$e = 0.01$			$e = 0.1$		
		Num.	IROD	Q	Num.	IROD	Q	Num.	IROD	Q
0°	0.5 km	1	3.5	3.5	1	3.8	3.8	1	7.7	7.7
	5 km	5	3.5	3.5	5	3.8	3.8	5	7.7	7.7
	50 km	5	3.9	3.7	5	4.3	4.0	5	9.7	8.6
	500 km	5	2.5	2.6	5	2.9	2.9	5	7.4	7.4
10°	0.5 km	1	5.8	5.8	1	6.3	6.3	1	12	12
	5 km	1	5.8	5.8	1	6.3	6.3	1	12	12
	50 km	1	5.8	5.8	1	6.3	6.3	1	12	12
	500 km	1	10	9.4	1	9.7	9.1	1	11	11
45°	0.5 km	1	23	23	1	24	24	1	30	30
	5 km	1	23	23	1	24	24	1	29	29
	50 km	1	23	23	1	23	23	1	29	29
	500 km	1	20	20	1	21	21	1	24	24
60°	0.5 km	1	28	28	1	29	29	1	31	31
	5 km	1	28	28	1	29	29	1	31	31
	50 km	1	28	28	1	28	28	1	30	30
	500 km	1	24	24	1	25	25	1	19	19

Table 7.6: Percent Position Errors, Nonlinear, Football, $N = 4$, $\Delta t = 1000 \text{ sec}$, $\Delta z = 10\%$

inc	Dwn. Sep.	$e = 0$			$e = 0.01$			$e = 0.1$		
		Num.	IROD	Q	Num.	IROD	Q	Num.	IROD	Q
0°	0.5 km	1	8.4	8.5	1	13	13	1	25	25
	5 km	1	8.0	8.7	1	13	13	1	24	25
	50 km	1	15	9.7	1	7.4	10	1	23	23
	500 km	6	20	15	6	21	17	1	25	22
10°	0.5 km	1	15	15	1	18	18	1	25	25
	5 km	1	14	14	1	18	18	1	25	25
	50 km	1	10	10	1	14	14	1	24	24
	500 km	2	20	19	2	20	20	1	27	25
45°	0.5 km	1	42	42	1	41	41	1	38	38
	5 km	1	42	42	1	41	41	1	37	37
	50 km	1	37	37	1	37	37	1	36	36
	500 km	4	29	28	2	29	29	1	32	32
60°	0.5 km	1	67	67	1	67	67	1	66	66
	5 km	1	67	67	1	67	67	1	66	66
	50 km	1	66	66	1	67	67	1	66	66
	500 km	3	38	38	3	44	44	2	65	64

Table 7.7: Percent Position Errors, Nonlinear, Leader-Follower, $N = 13$, $\Delta t = 250 \text{ sec}$, $\Delta z = 0\%$

<i>inc</i>	Dwn. Sep.	$e = 0$			$e = 0.01$			$e = 0.1$		
		Num.	IROD	Q	Num.	IROD	Q	Num.	IROD	Q
0°	0.5 km	2	1.1e-2	5.1e-3	2	1.9	1.9	2	23	25
	5 km	4	2.9e-2	1.9e-4	2	2.2	9.3e-2	2	23	25
	50 km	4	2.8	2.8	2	1.4e-1	8.5	2	28	28
	500 km	4	5.8e-1	4.2e-2	4	18	1.4e-1	2	6.1	8.6
10°	0.5 km	6	4.2e-2	3.6e-2	6	7.1e-1	7.1e-1	2	10	10
	5 km	4	1.7e-2	8.4e-2	6	7.9e-1	1.6e-1	2	12	12
	50 km	4	4.7	4.7	8	5.4	5.4	2	10	30
	500 km	8	14	17	6	13	3.8	4	21	13
45°	0.5 km	6	6.7	6.2	6	51	51	1	3.5e4	3.6e4
	5 km	8	4.7	4.7	6	48	48	2	90	90
	50 km	4	30	12	6	12	26	2	3.5e2	7.2e1
	500 km	8	12	8.5	4	13	13	2	62	71
60°	0.5 km	6	17	17	3	1.7e4	3.8e3	1	1.1e5	1.1e5
	5 km	6	48	27	4	77	94	2	97	100
	50 km	4	99	100	6	1.0e2	36	2	95	100
	500 km	6	2.1e2	99	4	91	100	2	73	73

As the inclination of the boring vehicles increases, the dynamics in spherical coordinates become more nonlinear, the linearized relative motion equations are less accurate, and the IROD algorithm is unable to find a good solution for the initial relative states.

7.2 $N=13$ Observations, Nonlinear Dynamics, $\Delta t = 250 \text{ sec}$

The cases in the previous section are repeated with $N = 13$ observations, the measurement time interval is $\Delta t = 250 \text{ sec}$, and the measurement period is 3000 sec . The results are shown in Tables 7.7-7.9.

For the Football cases shown above, the same trends are present. The $N = 4$ cases show better percent position errors than the $N = 13$ cases, and the IROD algorithm works well when the inclinations and eccentricities are small. At larger inclinations and eccentricities the IROD algorithm only gets bad estimates of the relative states. The above cases are repeated for some cross-track motion and the results are similar to the above results for $N = 13$. The $N = 13$ cases show the same general trends as the $N = 4$ cases, however, overall performance is seen to be better for the $N = 4$ cases.

The above cases were repeated for some out-of-plane motion ($\Delta z = 10\%$), i.e. 10% of

Table 7.8: Percent Position Errors, Nonlinear, Flyby, $N = 13$, $\Delta t = 250 \text{ sec}$, $\Delta z = 0\%$

inc	Dwn. Sep.	$e = 0$			$e = 0.01$			$e = 0.1$		
		Num.	IROD	Q	Num.	IROD	Q	Num.	IROD	Q
0°	0.5 km	1	4.1	4.6	1	4.3	5.0	1	6.2	11
	5 km	5	4.1	4.6	5	4.3	5.0	5	6.2	11
	50 km	5	4.0	4.5	7	4.2	4.9	5	6.0	11
	500 km	5	2.8	3.7	7	2.9	2.9	5	4.3	4.3
10°	0.5 km	1	4.3	4.9	1	4.3	5.1	1	2.9	5.9
	5 km	1	4.3	4.9	1	4.3	4.3	1	2.9	5.9
	50 km	5	4.3	4.8	5	4.3	4.9	5	3.0	5.8
	500 km	9	1.6e2	3.6	9	6.0e2	3.8	7	2.3e-1	4.7
45°	0.5 km	1	1.4e2	100	1	1.5e2	100	1	2.0e4	2.0e4
	5 km	1	1.4e2	1.4e2	1	1.4e2	1.4e2	1	2.2e3	2.2e3
	50 km	5	98	98	5	98	98	5	99	100
	500 km	5	98	98	5	98	98	5	99	100
60°	0.5 km	1	1.4e5	99	1	1.4e5	100	1	2.0e5	100
	5 km	1	1.4e4	100	1	1.4e4	100	1	2.0e4	100
	50 km	5	98	98	5	98	98	5	99	100
	500 km	5	98	98	5	98	98	5	99	100

Table 7.9: Percent Position Errors, Nonlinear, Football, $N = 13$, $\Delta t = 250 \text{ sec}$, $\Delta z = 0\%$

inc	Dwn. Sep.	$e = 0$			$e = 0.01$			$e = 0.1$		
		Num.	IROD	Q	Num.	IROD	Q	Num.	IROD	Q
0°	0.5 km	2	6.7	7.3	2	3.9	7.7	2	64	14
	5 km	6	6.9	7.3	6	4.0	7.7	6	68	14
	50 km	6	8.0	7.4	6	4.2e2	7.8	6	63	72
	500 km	6	26	10	6	27	11	6	39	38
10°	0.5 km	4	1.3e3	23	3	51	51	3	1.9e4	37
	5 km	4	1.3e3	25	3	1.4e3	46	3	1.6e3	42
	50 km	6	9.5	27	2	15	28	1	50	41
	500 km	6	35	25	6	37	26	6	43	38
45°	0.5 km	5	2.5e4	84	3	2.6e4	84	3	2.6e4	86
	5 km	4	2.5e3	97	3	2.5e3	98	3	36	100
	50 km	8	93	93	4	96	100	3	26	100
	500 km	8	97	100	8	98	100	8	99	100
60°	0.5 km	5	2.5e5	98	5	1.8e5	98		21	100
	5 km	5	2.9e3	100	5	2.6e3	100	3	22	100
	50 km	10	96	96	6	98	100	3	27	100
	500 km	8	97	100	8	98	100	8	99	100

Table 7.10: Percent Position Errors, Nonlinear, Leader-Follower, $N = 13$, $\Delta t = 250 \text{ sec}$, $\Delta z = 10\%$

inc	Dwn. Sep.	$e = 0$			$e = 0.01$			$e = 0.1$		
		Num.	IROD	Q	Num.	IROD	Q	Num.	IROD	Q
0°	0.5 km	5	5.0e-2	7.4e-2	3	10	4.1	4	45	33
	5 km	5	3.4e-2	2.0e-3	5	12	12	4	1.5e2	96
	50 km	4	3.2	4.6e-1	4	13	13	4	3.1	26
	500 km	6	18	1.9e-1	6	18	6.3e-1	4	25	28
10°	0.5 km	4	5.8e-3	5.7e-2	4	1.4	1.4	4	18	18
	5 km	4	2.3	3.8e-1	4	3.7	3.4	4	21	21
	50 km	8	13	14	6	10	6.6	4	49	36
	500 km	8	17	8.9e-1	8	19	1.0	4	5.8	52
45°	0.5 km	3	1.8	1.2	4	61	61	1	3.8e4	2.5e3
	5 km	5	3.8	3.4	4	58	58	1	3.8e3	1.7e2
	50 km	8	5.7	5.8	4	16	23	2	3.9e2	65
	500 km	8	14	18	0	37	74	2	72	72
60°	0.5 km	3	8.9	8.9	3	1.4e4	3.0e3	1	1.2e5	58
	5 km	3	19	20	4	82	98	1	1.2e4	83
	50 km	8	1.6e2	11	4	41	56	1	1.1e3	1.2e3
	500 km	8	95	100	8	1.3e2	97	2	83	83

the initial separation. Once again, the $N = 13$ cases show the same general trends as the $N = 4$ cases, however, the overall performance is seen to be better for the $N = 4$ cases.

The general trend shows that the $N = 4$ observation cases are more accurate than the $N = 13$ cases shown above.

7.3 $N=25$ Observations, Nonlinear Dynamics, $\Delta t = 125 \text{ sec}$

The cases in the previous sections are repeated with $N = 25$ observations, the measurement time interval is $\Delta t = 125 \text{ sec}$, and the measurement period is 3000 sec . The results are shown in Tables 7.13-7.15.

The key conclusion from these results is that the $N = 25$ results are very similar to the $N = 13$ results. The above cases are repeated for some out-of-plane motion ($\Delta z = 10\%$), i.e. 10% of the initial separation. Once again, the $N = 25$ cases show the same general trends as the $N = 4$ and $N = 13$ cases, however, the overall performance is better for the $N = 4$ cases.

The key conclusion is the $N = 25$ cases show the same general trends as the $N = 4$ and $N = 13$ cases, however, the overall performance is better for the $N = 4$ cases, even for

Table 7.11: Percent Position Errors, Nonlinear, Flyby, $N = 13$, $\Delta t = 250 \text{ sec}$, $\Delta z = 10\%$

inc	Dwn. Sep.	$e = 0$			$e = 0.01$			$e = 0.1$		
		Num.	IROD	Q	Num.	IROD	Q	Num.	IROD	Q
0°	0.5 km	1	4.5	4.8	1	4.8	5.2	1	11	13
	5 km	5	4.6	4.9	5	4.9	5.4	5	12	14
	50 km	5	6.3	4.8	5	6.8	5.3	5	19	14
	500 km	5	5.0e2	1e2	5	2.7e4	4.5	5	1.6e2	100
10°	0.5 km	5	2.7	2.9	5	2.5	2.8	5	12	12
	5 km	5	2.7	2.9	5	2.5	2.8	5	12	7.7
	50 km	9	2.8	2.8	9	8.5e3	1.6	7	11	7.9
	500 km	9	1.2e2	1.9	9	15	1.8	9	11	6.1
45°	0.5 km	1	4.3e3	4.3e3	1	1.5e4	2.9e2	1	2.6e5	2.6e5
	5 km	1	1.3e3	90	1	2.2e3	69	2	96	100
	50 km	5	99	100	5	99	100	2	96	100
	500 km	9	80	79	5	84	89	5	99	100
60°	0.5 km	1	3.1e5	99	1	3.2e5	99	1	5.1e5	5.1e5
	5 km	1	3.1e4	2.8e4	1	3.2e4	100	1	5.1e4	5.2e4
	50 km	5	99	100	5	99	100	1	5.1e3	5.1e3
	500 km	5	99	100	5	99	100	5	99	100

Table 7.12: Percent Position Errors, Nonlinear, Football, $N = 13$, $\Delta t = 250 \text{ sec}$, $\Delta z = 10\%$

inc	Dwn. Sep.	$e = 0$			$e = 0.01$			$e = 0.1$		
		Num.	IROD	Q	Num.	IROD	Q	Num.	IROD	Q
0°	0.5 km	2	18	27	2	6.8	7.1	4	82	100
	5 km	6	29	30	6	4.1	7.1	6	6.5e2	22
	50 km	6	92	31	6	1.1e2	32	10	4.4e3	2.5e3
	500 km	10	4.2e3	1.8e3	10	3.1e6	3.3e3	10	6.5e6	2.8e4
10°	0.5 km	6	48	48	6	44	44	5	54	54
	5 km	8	4.4e3	19	8	4.3e3	10	7	8.0e3	29
	50 km	10	3.3e2	27	10	28	27	3	51	40
	500 km	6	28	21	6	30	23	6	40	34
45°	0.5 km	6	5.6e5	29	6	5.1e5	35	5	1.1e5	71
	5 km	6	5.5e4	85	6	5.0e4	86	6	9.8e2	86
	50 km	10	4.1e3	99	10	98	98	8	1.0e2	86
	500 km	8	22	85	8	20	86	8	7.5	88
60°	0.5 km	6	1.1e6	93	6	1.0e6	94	6	2.8e5	97
	5 km	10	97	100	10	97	100	6	77	100
	50 km	10	97	100	10	97	100	10	98	100
	500 km	10	95	100	10	95	100	8	97	100

Table 7.13: Percent Position Errors, Nonlinear, Leader-Follower, $N = 25$, $\Delta t = 125 \text{ sec}$, $\Delta z = 0\%$

inc	Dwn. Sep.	$e = 0$			$e = 0.01$			$e = 0.1$		
		Num.	IROD	Q	Num.	IROD	Q	Num.	IROD	Q
0°	0.5 km	2	6.7e-3	7.7e-3	2	2.4	2.4	2	23	25
	5 km	4	2.9e-2	2.3e-4	2	2.4	8.7e-2	2	24	25
	50 km	4	2.5	2.5	2	1.3	7.4	2	27	25
	500 km	4	9.3e-2	4.5e-2	4	17	6.8e-1	2	10	18
10°	0.5 km	6	6.9e-2	6.7e-2	6	1.0	1.0	2	12	12
	5 km	4	8.3e-3	9.0e-2	6	1.2	1.1e-1	2	12	12
	50 km	4	4.6	4.7	8	5.2	5.2	2	52	26
	500 km	8	14	17	6	13	4.8	4	17	14
45°	0.5 km	6	7.2	6.1	6	50	50	1	4.6e4	2.0e3
	5 km	8	13	13	6	48	48	2	84	100
	50 km	4	31	10	6	14	24	2	4.5e2	66
	500 km	8	43	38	4	13	14	2	62	62
60°	0.5 km	6	17	17	6	79	94	1	1.3e5	1.3e5
	5 km	6	50	28	6	76	94	2	95	100
	50 km	2	1.1e3	2.2e2	6	1.2e2	30	2	93	100
	500 km	6	2.3e2	98	4	92	100	2	73	73

Table 7.14: Percent Position Errors, Nonlinear, Flyby, $N = 25$, $\Delta t = 125 \text{ sec}$, $\Delta z = 0\%$

inc	Dwn. Sep.	$e = 0$			$e = 0.01$			$e = 0.1$		
		Num.	IROD	Q	Num.	IROD	Q	Num.	IROD	Q
0°	0.5 km	1	4.0	4.6	1	4.2	5.0	1	5.5	11
	5 km	5	4.0	4.6	5	4.2	5.0	5	5.5	11
	50 km	5	3.9	4.5	5	4.1	4.9	5	5.4	11
	500 km	5	2.7	3.7	5	2.8	4.1	5	3.7	3.7
10°	0.5 km	1	4.1	4.9	1	4.1	5.1	1	1.5	6.4
	5 km	1	4.1	4.9	1	4.1	4.1	1	1.5	6.4
	50 km	5	4.1	4.8	5	4.1	5.0	5	1.6	6.3
	500 km	9	2.0e2	3.7	9	3.8	3.8	7	9.4e2	5.2
45°	0.5 km	1	1.5e2	100	1	1.7e2	100	1	3.1e4	3.2e4
	5 km	1	1.5e2	1.5e2	1	1.6e2	1.6e2	1	3.3e3	3.4e3
	50 km	5	98	100	5	98	100	5	99	99
	500 km	5	98	100	5	98	100	5	99	99
60°	0.5 km	1	1.4e5	99	1	1.5e5	100	1	2.1e5	100
	5 km	1	1.4e4	100	1	1.5e4	100	1	2.1e4	100
	50 km	5	98	100	5	98	100	5	99	99
	500 km	5	98	100	5	98	100	5	99	100

Table 7.15: Percent Position Errors, Nonlinear, Football, $N = 25$, $\Delta t = 125 \text{ sec}$, $\Delta z = 0\%$

inc	Dwn. Sep.	$e = 0$			$e = 0.01$			$e = 0.1$		
		Num.	IROD	Q	Num.	IROD	Q	Num.	IROD	Q
0°	0.5 km	2	7.2	7.1	2	5.0	7.5	4	36	14
	5 km	6	7.3	7.1	6	5.1	7.5	8	37	14
	50 km	6	8.2	7.2	6	5.8	7.7	6	1.7e2	15
	500 km	6	22	10	6	23	10	6	35	34
10°	0.5 km	4	30	28	4	18	29	3	64	64
	5 km	4	2.8e3	2.2	4	2.8e3	1.8	3	3.3e3	39
	50 km	8	70	27	8	38	29	3	20	40
	500 km	6	45	25	6	47	27	6	61	37
45°	0.5 km	3	3.3e4	81	3	3.2e4	82	3	3.4e4	83
	5 km	4	3.3e3	95	4	87	87	3	3.4e3	99
	50 km	8	99	100	8	99	100	3	66	100
	500 km	8	26	93	8	96	100	8	98	100
60°	0.5 km	3	4.2e4	100	3	4.2e4	100	3	1.7e4	100
	5 km	4	92	100	4	93	100	3	1.7e3	100
	50 km	8	99	100	8	99	100	3	2.2e2	100
	500 km	8	96	100	8	96	100	8	98	98

Table 7.16: Percent Position Errors, Nonlinear, Leader-Follower, $N = 25$, $\Delta t = 125 \text{ sec}$, $\Delta z = 10\%$

inc	Dwn. Sep.	$e = 0$			$e = 0.01$			$e = 0.1$		
		Num.	IROD	Q	Num.	IROD	Q	Num.	IROD	Q
0°	0.5 km	5	9.8e-2	5.4e-2	3	10	4.0	2	43	32
	5 km	5	3.2e-2	2.0e-3	5	12	12	4	63	75
	50 km	4	3.2	5.7e-1	4	13	13	4	23	40
	500 km	6	18	1.9e-1	6	18	6.4e-1	4	25	29
10°	0.5 km	4	9.7e-2	5.2e-2	4	2.8	2.8	4	27	27
	5 km	4	2.6	5.5e-1	4	6.7	6.8	4	28	28
	50 km	8	12	12	6	9.9	6.7	4	100	12
	500 km	8	17	9.3e-1	8	19	9.0e-1	4	11	45
45°	0.5 km	3	2.2	1.5	4	68	68	1	4.6e4	3.1e3
	5 km	5	5.4	3.4	4	64	64	1	4.6e3	2.3e2
	50 km	8	6.8	6.8	4	15	24	2	4.6e2	59
	500 km	8	13	16	8	29	26	2	72	72
60°	0.5 km	3	9.2	9.2	3	1.3e4	2.6e3	1	1.3e5	76
	5 km	3	19	22	4	86	99	1	1.3e4	84
	50 km	8	1.6e2	14	4	57	57	1	1.3e3	98
	500 km	8	1.3e2	100	8	1.4e2	97	2	83	83

Table 7.17: Percent Position Errors, Nonlinear, Flyby, $N = 25$, $\Delta t = 125 \text{ sec}$, $\Delta z = 10\%$

inc	Dwn. Sep.	$e = 0$			$e = 0.01$			$e = 0.1$		
		Num.	IROD	Q	Num.	IROD	Q	Num.	IROD	Q
0°	0.5 km	1	4.4	4.7	1	4.6	5.2	1	10	13
	5 km	5	4.4	4.9	5	4.7	5.4	5	11	14
	50 km	5	5.2	4.8	5	5.5	5.4	5	15	14
	500 km	5	3.7e2	4.1	5	2.4e4	4.5	5	1.2e3	12
10°	0.5 km	5	2.6	2.9	5	2.4	2.8	5	12	12
	5 km	5	2.6	2.9	5	2.4	2.8	5	12	6.7
	50 km	9	7.0e3	1.8	9	2.4	2.7	7	11	6.9
	500 km	9	25	1.9	9	98	1.8	9	11	5.7
45°	0.5 km	1	9.6e2	9.6e2	1	2.7e3	2.7e3	1	2.4e5	2.4e5
	5 km	1	7.2e2	7.2e2	1	1.2e3	97	1	2.4e4	2.4e4
	50 km	5	98	98	5	98	98	1	2.4e3	2.4e3
	500 km	9	98	98	5	82	85	5	99	100
60°	0.5 km	1	2.9e5	2.9e5	1	3.0e5	3.0e5	1	4.9e5	4.6e5
	5 km	1	2.9e4	2.9e4	1	3.0e4	3.0e4	1	4.9e4	4.6e4
	50 km	5	98	98	5	98	100	1	4.9e3	4.6e3
	500 km	5	98	100	5	98	100	5	99	100

Table 7.18: Percent Position Errors, Nonlinear, Football, $N = 25$, $\Delta t = 125 \text{ sec}$, $\Delta z = 10\%$

inc	Dwn. Sep.	$e = 0$			$e = 0.01$			$e = 0.1$		
		Num.	IROD	Q	Num.	IROD	Q	Num.	IROD	Q
0°	0.5 km	2	22	27	2	16	28	2	2.5e2	56
	5 km	6	29	30	6	20	32	6	3.1e2	44
	50 km	6	85	23	6	41	32	8	9.2e2	96
	500 km	10	2.9e2	4.1e3	10	99	2.7e3	10	8.6e3	3.9e3
10°	0.5 km	8	37	28	8	32	28	7	69	69
	5 km	8	1.6e3	11	8	1.2e3	20	7	9.6e3	10
	50 km	8	1.3e2	27	8	4.8e2	27	3	4.6e2	39
	500 km	6	40	22	6	42	23	6	57	34
45°	0.5 km	6	1.8e5	48	6	1.4e5	55	4	4.8e4	78
	5 km	10	1.7e4	88	10	1.3e4	89	4	4.7e3	88
	50 km	10	97	97	10	97	97	8	98	100
	500 km	6	39	86	8	37	87	8	18	89
60°	0.5 km	6	7.8e5	94	6	7.0e5	94	6	6.1e4	99
	5 km	10	96	100	10	96	100	10	97	97
	50 km	10	95	100	10	96	100	10	97	100
	500 km	10	92	100	10	92	100	8	94	100

some cross-track motion. For most of the cases presented above, the IROD algorithm is able to find good estimates for the initial relative states when the inclination and eccentricity are low. Although the inclinations and eccentricities of LEO objects vary greatly, a better potential application for this IROD algorithm may be GEO objects where the inclinations and eccentricity of all GEO objects are low and fall into a small range. The IROD algorithm may perform much better and find accurate IROD estimates if tested on GEO objects where the inclinations and eccentricities are small. Chapter 10 tests the IROD algorithm against a range of GEO cases, presenting the percent position errors while varying the relative motion trajectories, inclination, eccentricity, downrange separations, and cross-track motion.

CHAPTER 8

EFFECT OF EXCLUDING J_2 FROM IROD ALGORITHM FOR LEO

This chapter shows the importance of including the J_2 perturbation in the IROD algorithm models when the measurements include J_2 effects. One of the main motivations of this new formulation of the IROD algorithm was to include J_2 perturbation effects. Previous research has shown that the J_2 perturbation has a large effect on relative motion at LEO [57]. In LEO, the J_2 perturbation is a more dominant effect than other spherical harmonic perturbations or perturbations due to third-bodies [7]. The question that this section seeks to answer is: How does the IROD algorithm perform when J_2 perturbations are excluded from the IROD algorithm but included the dynamics of the deputy and chief? The test cases shown below vary the number of measurements, relative motion trajectories, separation between chief and deputy, inclination and eccentricity. The dynamics are propagated using 2-body and J_2 perturbations, but the J_2 perturbations are turned off in the IROD algorithm. The percent position errors are tabulated for these cases in Tables 8.1-8.3.

8.1 N=4 Observations, Nonlinear Dynamics, $\Delta t = 1000 \text{ sec}$

This section presents a range of LEO relative motion cases where the IROD algorithm does not include perturbations due to J_2 but the dynamics used to generate the four LOS measurements have J_2 included. Some cross-track motion is also added.

Several interesting trends are evident in these Leader-Follower cases. For many of the cases, the IROD algorithm cannot find a solution (noted with NS) or the solution error is large (marked in red). From these results, it is evident that including the J_2 perturbations in the IROD algorithm is vital for arriving at a good initial estimate when the measurements are generated using J_2 perturbations.

The exception is when the vehicle separation is large. In the cases, the IROD algorithm without J_2 is able to find better estimates than at smaller vehicle separations. This can

Table 8.1: Percent Position Errors, Nonlinear, Leader-Follower, $N = 4$, $\Delta t = 1000 \text{ sec}$, $\Delta z = 0\%$, NO IROD J_2

<i>inc</i>	Dwn. Sep.	$e = 0$			$e = 0.01$			$e = 0.1$		
		Num.	IROD	Q	Num.	IROD	Q	Num.	IROD	Q
0°	0.5 km	4	1.6e-2	7.2e-4	2	46	100	0	NS	NS
	5 km	4	3.3	1.0e-3	2	27	100	0	NS	NS
	50 km	4	1.7	4.2e-4	2	26	100	0	NS	NS
	500 km	4	2.0	4.2e-2	4	25	25	2	44	54
10°	0.5 km	2	9.3e7	3.0e6	2	56	69	0	NS	NS
	5 km	2	5.6e2	99	2	25	28	0	NS	NS
	50 km	4	23	23	2	16	16	0	NS	NS
	500 km	4	15	15	4	33	33	2	44	45
45°	0.5 km	2	1.9e3	1.0e3	0	NS	NS	0	NS	NS
	5 km	4	4.8e4	3.5e4	0	NS	NS	0	NS	NS
	50 km	2	18	18	2	44	44	0	NS	NS
	500 km	4	4.0	4.3	4	23	23	2	60	60
60°	0.5 km	2	1.4e4	1.1e3	0	NS	NS	0	NS	NS
	5 km	5	1.9e4	1.5e4	0	NS	NS	0	NS	NS
	50 km	4	18	18	2	65	65	0	NS	NS
	500 km	6	10	10	6	20	20	2	74	74

be explained by considering the effect that the J_2 perturbation has on the relative motion of the satellites. At small separations the effect of the J_2 perturbation on relative motion is relatively large where a small change in the relative motion due to the J_2 is much more apparent when the vehicles are closer than when they are further apart. At larger separations the effect of the J_2 perturbation on the LOS angle measurements is smaller, so the J_2 perturbation has a much smaller effect on the relative motion at larger separations. Since the effect of relative J_2 is small at larger separations, the LOS measurements at larger separations are similar with or without the including of J_2 perturbations. Since the LOS measurements are similar with or without the J_2 perturbations at large satellite separations, the IROD algorithm is able to find better estimates at larger separations.

The Flyby cases above reinforce the previous trends. When compared to the previous tables, where the J_2 perturbation is included, these cases show that the IROD algorithm finds worse estimates when the J_2 perturbation is not included. The majority of the cases show that the percent position errors are worse in the cases above where the J_2 perturbations are not included in the algorithm. Also, the IROD algorithm finds better estimates at larger satellite separations since the relative J_2 effect is smaller at larger separations.

Table 8.2: Percent Position Errors, Nonlinear, Flyby, $N = 4$, $\Delta t = 1000 \text{ sec}$, $\Delta z = 0\%$, NO IROD J_2

inc	Dwn. Sep.	$e = 0$			$e = 0.01$			$e = 0.1$		
		Num.	IROD	Q	Num.	IROD	Q	Num.	IROD	Q
0°	0.5 km	0	NS	NS	0	NS	NS	0	NS	NS
	5 km	0	NS	NS	0	NS	NS	0	NS	NS
	50 km	5	20	20	5	23	23	5	44	44
	500 km	5	2.0	5.2	5	5.5	5.9	5	11	12
10°	0.5 km	0	NS	NS	0	NS	NS	0	NS	NS
	5 km	0	NS	NS	0	NS	NS	0	NS	NS
	50 km	1	23	23	1	27	27	1	46	46
	500 km	1	11	11	1	11	11	1	12	12
45°	0.5 km	0	NS	NS	0	NS	NS	0	NS	NS
	5 km	0	NS	NS	0	NS	NS	0	NS	NS
	50 km	1	65	65	1	67	67	1	59	59
	500 km	1	21	21	1	21	21	1	8.3	8.3
60°	0.5 km	0	NS	NS	0	NS	NS	0	NS	NS
	5 km	0	NS	NS	0	NS	NS	0	NS	NS
	50 km	1	80	80	1	80	80	1	47	47
	500 km	1	24	24	1	23	23	1	17	17

Table 8.3: Percent Position Errors, Nonlinear, Football, $N = 4$, $\Delta t = 1000 \text{ sec}$, $\Delta z = 0\%$, NO IROD J_2

inc	Dwn. Sep.	$e = 0$			$e = 0.01$			$e = 0.1$		
		Num.	IROD	Q	Num.	IROD	Q	Num.	IROD	Q
0°	0.5 km	4	77	100	0	NS	NS	1	1.3e3	1.3e3
	5 km	0	NS	NS	0	NS	NS	1	1.0e2	1.0e2
	50 km	1	28	32	1	22	26	1	10	12
	500 km	6	21	15	6	22	16	1	25	22
10°	0.5 km	0	NS	NS	1	3.9e2	3.9e2	1	1.8e3	1.8e3
	5 km	1	37	37	1	28	28	1	1.6e2	1.6e2
	50 km	1	66	66	1	5.9	5.9	1	5.0	5.0
	500 km	2	19	18	2	20	19	1	24	24
45°	0.5 km	1	1.5e4	1.5e4	1	1.3e4	1.3e4	1	6.7e3	6.7e3
	5 km	1	1.5e3	1.5e3	1	1.3e3	1.3e3	1	6.4e2	6.4e2
	50 km	1	1.2e2	1.2e2	1	1.1e2	1.1e2	1	35	35
	500 km	2	15	14	2	16	15	1	24	24
60°	0.5 km	1	1.3e4	1.3e4	1	1.1e4	1.1e4	1	4.5e3	4.5e3
	5 km	1	1.3e3	1.3e3	1	1.1e3	1.1e3	1	4.0e2	4.0e2
	50 km	1	94	94	1	68	68	1	15	15
	500 km	3	24	23	3	29	28	2	54	54

Table 8.4: Percent Position Errors, Nonlinear, Leader-Follower, $N = 4$, $\Delta t = 1000 \text{ sec}$, $\Delta z = 10\%$, NO IROD J_2

inc	Dwn. Sep.	$e = 0$			$e = 0.01$			$e = 0.1$		
		Num.	IROD	Q	Num.	IROD	Q	Num.	IROD	Q
0°	0.5 km	2	5.5	4.5	2	9.4e2	9.3e2	0	NS	NS
	5 km	4	8.3	8.3	2	69	77	0	NS	NS
	50 km	4	2.2	2.1	2	18	17	0	NS	NS
	500 km	4	3.0	3.3	4	28	25	2	46	45
10°	0.5 km	4	3.8e6	1.4e5	2	8.2e2	7.8e2	0	NS	NS
	5 km	2	55	49	2	60	60	0	NS	NS
	50 km	4	16	17	2	9.0	10	0	NS	NS
	500 km	4	10	10	4	14	13	2	44	44
45°	0.5 km	2	2.8e3	5.5e2	0	NS	NS	0	NS	NS
	5 km	4	3.2e4	1.1e5	0	NS	NS	0	NS	NS
	50 km	2	5.9	6.5	2	41	41	0	NS	NS
	500 km	4	3.0	3.3	4	24	24	2	66	66
60°	0.5 km	4	1.2e4	1.5e3	0	NS	NS	0	NS	NS
	5 km	4	1.0e4	85	0	NS	NS	0	NS	NS
	50 km	4	9.0	9.2	2	60	60	0	NS	NS
	500 km	6	10	10	6	21	20	2	82	82

The Football cases above are still consistent with the previous trends. The percent position errors are worse in the cases above where the J_2 perturbations are not included in the algorithm. As in the previous cases, the IROD algorithm finds better estimates at larger satellite separations since the relative J_2 effect is smaller at larger separations.

The above cases were repeated for some out-of-plane motion ($\Delta z = 10\%$), i.e. 10% of the initial separation. These cases are shown in Tables 8.5-8.7.

These cross-track results in Tables 8.4-8.6 show the same trends.

8.2 N=13 Observations, Nonlinear Dynamics, $\Delta t = 250 \text{ sec}$

The following section re-runs the previous cases where now there are $N = 13$ observations taken within the same total time frame.

Increasing the number of observations for these Leader-Follower cases does not improve the results. The IROD algorithm performs worse when the J_2 perturbations are not included in the algorithm but are used in generating the measurements. For the close separation cases, the IROD algorithm performs poorly and often cannot find a solution at all.

These Flyby cases do not improve the results when more observations of the deputy

Table 8.5: Percent Position Errors, Nonlinear, Flyby, $N = 4$, $\Delta t = 1000 \text{ sec}$, $\Delta z = 10\%$, NO IROD J_2

inc	Dwn. Sep.	$e = 0$			$e = 0.01$			$e = 0.1$		
		Num.	IROD	Q	Num.	IROD	Q	Num.	IROD	Q
0°	0.5 km	0	NS	NS	0	NS	NS	0	NS	NS
	5 km	0	NS	NS	0	NS	NS	0	NS	NS
	50 km	5	20	19	5	23	23	5	46	44
	500 km	5	4.1	4.2	5	4.7	4.8	5	10	10
10°	0.5 km	0	NS	NS	0	NS	NS	0	NS	NS
	5 km	0	NS	NS	0	NS	NS	0	NS	NS
	50 km	1	18	18	1	21	21	1	37	37
	500 km	1	11	10	1	11	10	1	13	14
45°	0.5 km	2	1.3e5	1.2e6	0	NS	NS	0	NS	NS
	5 km	2	1.3e5	1.2e5	0	NS	NS	0	NS	NS
	50 km	1	59	59	1	61	61	1	51	51
	500 km	1	24	24	1	25	25	1	27	27
60°	0.5 km	0	NS	NS	0	NS	NS	0	NS	NS
	5 km	0	NS	NS	0	NS	NS	0	NS	NS
	50 km	1	80	80	1	81	81	1	64	64
	500 km	1	30	30	1	30	30	1	23	23

Table 8.6: Percent Position Errors, Nonlinear, Football, $N = 4$, $\Delta t = 1000 \text{ sec}$, $\Delta z = 10\%$, NO IROD J_2

inc	Dwn. Sep.	$e = 0$			$e = 0.01$			$e = 0.1$		
		Num.	IROD	Q	Num.	IROD	Q	Num.	IROD	Q
0°	0.5 km	4	77	77	0	NS	NS	1	2.5e3	2.1e3
	5 km	0	NS	NS	0	NS	NS	1	1.1e2	1.0e2
	50 km	1	28	28	1	2.9e2	1.8e2	1	10	11
	500 km	6	21	16	6	21	17	1	24	22
10°	0.5 km	0	NS	NS	1	34	34	1	1.7e3	1.7e3
	5 km	1	94	94	1	13	13	1	1.5e2	1.5e2
	50 km	1	17	17	1	14	14	1	7.2	7.4
	500 km	2	20	19	2	20	20	1	26	24
45°	0.5 km	1	1.4e4	1.4e4	1	1.3e4	1.3e4	1	6.6e3	6.6e3
	5 km	1	1.4e3	1.4e3	1	1.2e3	1.2e3	1	6.2e2	6.2e2
	50 km	1	1.1e2	1.1e2	1	97	97	1	30	30
	500 km	2	21	20	2	22	21	1	27	27
60°	0.5 km	1	1.5e4	1.5e4	1	1.2e4	1.2e4	1	4.6e3	4.6e3
	5 km	1	1.4e3	1.4e3	1	1.2e3	1.2e3	1	4.0e2	4.0e2
	50 km	1	1.0e2	1.0e2	1	74	74	1	17	17
	500 km	3	26	25	3	31	30	2	57	57

Table 8.7: Percent Position Errors, Nonlinear, Leader-Follower, $N = 13$, $\Delta t = 250 \text{ sec}$, $\Delta z = 0\%$, NO IROD J_2

inc	Dwn. Sep.	$e = 0$			$e = 0.01$			$e = 0.1$		
		Num.	IROD	Q	Num.	IROD	Q	Num.	IROD	Q
0°	0.5 km	4	7.7e-1	4.1e-1	2	1.4e2	100	4	7.2e3	100
	5 km	4	1.5e-1	1.3e-3	2	8.0	100	2	6.9e2	100
	50 km	4	1.5	4.2e-4	2	24	100	4	58	99
	500 km	4	4.1e-2	4.2e-2	4	22	3.8	2	22	36
10°	0.5 km	3	67	79	4	2.5e2	100	4	5.8e2	100
	5 km	3	12	42	6	50	100	4	30	100
	50 km	8	10	3.4	6	17	88	2	25	100
	500 km	8	18	17	6	14	8.1	4	40	42
45°	0.5 km	4	4.8e2	100	6	2.0e3	100	2	1.8e4	100
	5 km	6	95	56	6	1.6e2	100	2	1.7e3	100
	50 km	7	97	97	6	28	100	2	1.3e2	100
	500 km	8	21	17	4	4.9	6.0e-1	2	24	100
60°	0.5 km	6	62	100	6	7.4e3	100	2	2.7e4	2.7e4
	5 km	10	1.4e2	100	6	6.5e2	100	2	2.6e3	2.6e3
	50 km	7	35	93	6	12	100	2	1.7e2	1.7e2
	500 km	6	2.0e2	99	4	67	98	2	36	36

Table 8.8: Percent Position Errors, Nonlinear, Flyby, $N = 13$, $\Delta t = 250 \text{ sec}$, $\Delta z = 0\%$, NO IROD J_2

inc	Dwn. Sep.	$e = 0$			$e = 0.01$			$e = 0.1$		
		Num.	IROD	Q	Num.	IROD	Q	Num.	IROD	Q
0°	0.5 km	0	NS	NS	0	NS	NS	0	NS	NS
	5 km	0	NS	NS	2	2.6e4	48	0	NS	NS
	50 km	7	1.1e3	15	7	5.1e3	17	5	48	45
	500 km	5	4.3	5.4	7	4.7	4.7	5	8.4	8.4
10°	0.5 km	0	NS	NS	0	NS	NS	1	1.5e3	1.5e3
	5 km	1	82	84	1	85	100	1	1.5e2	1.5e2
	50 km	5	12	12	5	12	13	5	9.9	8.9
	500 km	9	2.1e2	4.5	9	2.9	4.7	5	5.8e-1	4.8
45°	0.5 km	1	2.5e3	2.5e3	1	2.3e3	2.3e3	5	66	100
	5 km	5	97	100	5	97	100	5	96	100
	50 km	5	98	98	5	98	98	5	99	99
	500 km	5	98	98	5	98	98	5	99	100
60°	0.5 km	5	61	100	5	63	100	5	54	100
	5 km	5	95	100	5	95	100	5	95	100
	50 km	5	98	98	5	98	98	5	99	100
	500 km	5	98	98	5	98	98	5	99	99

Table 8.9: Percent Position Errors, Nonlinear, Football, $N = 13$, $\Delta t = 250 \text{ sec}$, $\Delta z = 0\%$, NO IROD J_2

inc	Dwn. Sep.	$e = 0$			$e = 0.01$			$e = 0.1$		
		Num.	IROD	Q	Num.	IROD	Q	Num.	IROD	Q
0°	0.5 km	6	3.9e3	100	6	4.0e3	100	6	1.5e2	100
	5 km	6	49	49	6	51	51	6	1.0e3	51
	50 km	6	37	10	6	42	10	6	71	1.3
	500 km	6	26	8.9	6	27	10	6	39	37
10°	0.5 km	8	74	100	6	80	100	3	8.8e2	8.8e2
	5 km	8	7.0e2	12	8	7.4e2	65	3	40	40
	50 km	6	21	14	6	39	16	1	41	27
	500 km	6	42	24	6	42	26	6	45	37
45°	0.5 km	3	2.9e4	100	3	2.7e4	100	3	1.2e4	100
	5 km	3	2.9e3	100	3	2.7e3	100	3	1.2e3	100
	50 km	3	2.8e2	100	3	2.5e2	100	3	93	100
	500 km	8	98	98	8	98	98	8	99	100
60°	0.5 km	5	3.9e4	100	5	3.6e4	100	3	1.5e4	100
	5 km	5	3.9e3	100	5	3.6e3	100	3	1.5e3	100
	50 km	5	4.0e2	100	5	3.7e2	100	3	1.4e2	100
	500 km	8	98	100	8	98	98	8	99	100

vehicle are used for an IROD estimate. The results continue to be much poorer when the J_2 effects are not accounted for in the IROD algorithm.

These Football cases continue to be poor without the inclusion of J_2 effects. Larger separation cases get slightly better percent position errors but still not acceptable.

The above cases were repeated for some out-of-plane motion ($\Delta z = 10\%$), i.e. 10% of the initial separation. These cases are shown in Tables 8.10-8.12.

8.3 Summarizing Remarks

These results support the fact that the IROD algorithm needs to include the effects of J_2 for LEO when the J_2 perturbation is included in creating the LOS measurements. When J_2 is not included, the IROD algorithm generally performs more poorly than with the J_2 term. The exception is when there are large relative separations, where the effect of differential J_2 perturbation on LOS angles is small.

Table 8.10: Percent Position Errors, Nonlinear, Leader-Follower, $N = 13$, $\Delta t = 250 \text{ sec}$, $\Delta z = 10\%$, NO IROD J_2

inc	Dwn. Sep.	$e = 0$			$e = 0.01$			$e = 0.1$		
		Num.	IROD	Q	Num.	IROD	Q	Num.	IROD	Q
0°	0.5 km	5	9.6	3.4	4	5.6e2	90	2	6.8e3	3.2e3
	5 km	5	17	16	4	57	40	2	6.2e2	2.8e2
	50 km	5	6.5	4.3	4	18	21	4	44	23
	500 km	6	18	4.0e-1	6	17	9.7e-1	4	29	26
10°	0.5 km	2	48	100	4	2.8e2	100	4	3.1e2	100
	5 km	8	25	28	4	12	100	4	8.0	100
	50 km	8	1.7	6.5	8	2.6e2	33	4	22	100
	500 km	8	17	2.7e-1	8	19	2.7	4	32	37
45°	0.5 km	0	NS	NS	6	1.6e3	100	2	1.9e4	100
	5 km	4	59	100	4	1.2e2	100	2	1.9e3	100
	50 km	6	85	18	6	21	100	2	1.4e2	100
	500 km	8	67	67	8	39	68	2	25	100
60°	0.5 km	0	NS	NS	4	6.2e3	100	2	9.8e4	100
	5 km	4	6.0e2	100	4	5.4e2	100	2	9.7e3	100
	50 km	6	1.9e2	28	4	2.5e3	100	2	9.2e2	100
	500 km	8	94	100	8	1.1e2	96	2	48	48

Table 8.11: Percent Position Errors, Nonlinear, Flyby, $N = 13$, $\Delta t = 250 \text{ sec}$, $\Delta z = 10\%$, NO IROD J_2

inc	Dwn. Sep.	$e = 0$			$e = 0.01$			$e = 0.1$		
		Num.	IROD	Q	Num.	IROD	Q	Num.	IROD	Q
0°	0.5 km	0	NS	NS	0	NS	NS	1	3.5e3	2.3e2
	5 km	2	1.2e2	100	2	1.4e2	99	1	4.3e2	72
	50 km	5	21	14	5	26	15	5	39	20
	500 km	5	1.5e2	2.0e2	5	2.6e4	5.9e2	5	7.0	5.5e2
10°	0.5 km	4	8.2e5	3.5e3	4	9.2e5	3.7e3	3	4.1e3	4.1e3
	5 km	5	90	100	5	91	100	3	4.2e2	100
	50 km	9	7.5e3	10	9	8.9e3	8.8	9	48	8.8
	500 km	9	1.2e2	2.8	9	12	4.1e3	9	12	7.3
45°	0.5 km	5	76	100	5	74	100	5	98	100
	5 km	5	96	100	5	96	100	5	91	100
	50 km	5	98	98	5	98	98	5	99	99
	500 km	7	81	68	5	86	89	5	99	100
60°	0.5 km	5	36	100	5	32	100	5	85	100
	5 km	5	93	100	5	92	100	5	90	100
	50 km	5	98	100	5	98	100	5	98	100
	500 km	5	99	100	5	99	100	5	99	100

Table 8.12: Percent Position Errors, Nonlinear, Football, $N = 13$, $\Delta t = 250 \text{ sec}$, $\Delta z = 10\%$, NO IROD J_2

inc	Dwn. Sep.	$e = 0$			$e = 0.01$			$e = 0.1$		
		Num.	IROD	Q	Num.	IROD	Q	Num.	IROD	Q
0°	0.5 km	6	2.7e3	99	6	2.6e3	99	6	1.1e3	99
	5 km	6	1.5e3	46	6	1.4e3	21	6	1.3e2	99
	50 km	6	2.4e3	1.5e2	6	2.5e3	2.7e2	10	7.8e3	2.6e3
	500 km	10	1.2e5	1.7e4	10	5.8e3	3.7e3	10	3.6e4	3.1e4
10°	0.5 km	12	65	100	12	3.2e3	41	7	8.8e2	8.8e2
	5 km	12	4.7e2	78	12	96	100	7	38	38
	50 km	8	11	10	8	2.4e2	11	3	2.0e2	25
	500 km	6	34	20	6	35	22	6	41	34
45°	0.5 km	5	5.4e4	100	5	5.1e4	100	5	2.5e4	100
	5 km	5	5.4e3	100	5	5.1e3	100	5	2.5e3	100
	50 km	5	5.1e2	100	5	4.9e2	100	3	2.3e2	100
	500 km	8	23	87	8	23	87	8	98	100
60°	0.5 km	5	8.2e4	100	5	7.9e4	100	5	4.6e4	100
	5 km	5	8.2e3	100	5	7.9e3	100	5	4.6e3	100
	50 km	5	8.1e2	100	5	7.8e2	100	5	4.6e2	100
	500 km	10	95	100	10	95	100	8	97	96

CHAPTER 9

MEASUREMENT ERROR ANALYSIS

All of the previous IROD solutions have been generated assuming no LOS measurement error. In the real world, LOS measurement error is a real and important issue for IROD algorithms and navigation problems in general. Measurement error is closely linked with the accuracy of a camera where, the higher the accuracy, the lower the measurement error but also the higher the cost. This chapter seeks to present several case studies that compare IROD results with varying amounts of measurement error, specifically, measurement noise. In future work, these results can be expanded to include a much more in-depth study of measurement error effects including LOS measurement noise, bias, misalignment, and other sources of error.

9.1 Measurement Error Analysis at LEO

Previous research shows that measurement noise can have a crippling effect in implementing an IROD algorithm with noisy data [58]. Geller conducted a preliminary performance analysis for an IROD algorithm, finding a clear dependence of orbit estimation performance on the geometry of the relative orbits. The results from Geller's performance analysis can also be compared with the performance of the newly derived IROD algorithm (with measurement noise) in the following subsections. There are several LEO cases presented below with varying amounts of Gaussian white noise injected into the LOS measurements to simulate varying amounts of camera noise when observing a nearby satellite. For brevity, when the LOS measurements are generated using the Linearized dynamics and 2nd-order measurement equations, it will be abbreviated as L2O (Linearized and 2nd-Order).

Data is collected based on a Monte-Carlo analysis ($N = 100$ samples) with various levels of measurement noise injected into the 2nd-order measurement model or measurement noise injected into the nonlinear models and shown in Tables .

Table 9.1: Azimuth and Elevation Angles from L2O environment and Nonlinear Dynamics for a Leader-Follower 5 km LEO case.

	L2O	Full Nonlinear
Azimuth Angles (rad)	-0.000354957494077	-0.000354957509879
	0.008527848817372	0.008524923708307
	0.007995402447650	0.007986820364862
	-0.001306718487425	-0.001317752198797
Elevation Angles (rad)	0.087266455160634	0.087266462599716
	0.039836567170945	0.039837171338920
	-0.049958816940329	-0.049957209379231
	-0.086795814296264	-0.086796085830501

9.1.1 Leader-Follower 5 km

As a starting point, the angle measurements for a Leader-Follower 5 km relative motion configuration ($i = 5^\circ$, $e = 0.01$, $\Delta z = 0$, J_2 ON, $\Delta t = 1000 \text{ sec}$) with $N = 4$ observations for L2O models and full nonlinear models are provided in Table 9.1.

Differencing the Azimuth and Elevation angles between the L2O environment and Nonlinear environment yields

$$\Delta\alpha = \begin{bmatrix} 0.000000158016979 \\ 0.029251090656827 \\ 0.085820827883769 \\ 0.110337113713500 \end{bmatrix} \times 10^{-4} \text{ rad}$$

$$\Delta\beta = \begin{bmatrix} -0.000743908272482 \\ -0.060416797487139 \\ -0.160756109734289 \\ 0.027153423697024 \end{bmatrix} \times 10^{-5} \text{ rad}$$

Notice that the initial angle difference is very small in both the azimuth and elevation direction. As the two simulations are propagated, the difference between the nonlinear and linearized/2nd Order LOS angles grow.

The following data in Table 9.2 was collected based on Monte-Carlo Analysis ($N = 100$ samples) with various levels of measurement noise injected into the 2nd-order measurement model.

Table 9.2: Percent Position Errors and Standard Deviation with varying magnitudes of measurement noise added to L2O LOS angles for 100 Monte Carlo Runs (Leader-Follower 5 km LEO)

	$\sigma \approx 10^{-4}$	$\sigma \approx 10^{-5}$	$\sigma \approx 10^{-6}$	$\sigma \approx 10^{-7}$	$\sigma \approx 10^{-8}$	L2O
Avg. Pos. Err (%)	1774	543	198.3	24.4	2.41	1.6×10^{-2}
Std. Dev. (%)	2192	437	175.2	22.3	1.55	

Table 9.3: Percent Position Errors and Standard Deviation with varying magnitudes of measurement noise added to Nonlinear LOS angles for 100 Monte Carlo Runs (Leader-Follower 5 km LEO)

	$\sigma \approx 10^{-4}$	$\sigma \approx 10^{-5}$	$\sigma \approx 10^{-6}$	$\sigma \approx 10^{-7}$	$\sigma \approx 10^{-8}$	Nonlinear
Avg. Pos. Err (%)	1772	508	217	27.9	4.55	4.4
Std. Dev. (%)	2406	432	174	25.1	2.57	

The following data in Table 9.3 was collected based on Monte-Carlo Analysis ($N = 100$ samples) with various levels of measurement noise injected into the nonlinear angle measurements.

These tables show that in this case (Leader-Follower, 5 km) the IROD algorithm works well with small amounts of measurement noise (when $\sigma \approx 10^{-7} - 10^{-8}$ rad) but measurement noise higher than this results in large percent position errors from the IROD algorithm. No current camera exists with this kind of fidelity. Most cameras used for space applications can be expected to have a measurement noise level around $\sigma \approx 10^{-3} - 10^{-5}$ rad. (For Reference, the Hubble Space Telescope has a resolution of 2×10^{-7} rad).

9.1.2 Leader-Follower 10 km

The angle measurements for a Leader-Follower 10 km relative motion configuration ($i = 5^\circ$, $e = 0.01$, $\Delta z = 0$, J_2 ON, $\Delta t = 1000$ sec) with $N = 4$ observations are provided in Table 9.4.

Differencing the Azimuth and Elevation angles between the L2O environment and Nonlinear environment yields

Table 9.4: Azimuth and Elevation Angles from L2O environment and Nonlinear Dynamics for a Leader-Follower 10 km LEO case.

	L2O	Full Nonlinear
Azimuth Angles (rad)	-0.000709914894280	-0.000709915021044
	0.008178849956370	0.008172998009809
	0.007655549716292	0.007638375808699
	-0.001643491942979	-0.001665578643751
Elevation Angles (rad)	0.087266432843388	0.087266462599716
	0.039835957551602	0.039837173363867
	-0.049960411870646	-0.049957203973071
	-0.086795527841964	-0.086796086686815

Table 9.5: Percent Position Errors and Standard Deviation with varying magnitudes of measurement noise added to L2O LOS angles for 100 Monte Carlo Runs (Leader-Follower 10 km LEO)

	$\sigma \approx 10^{-4}$	$\sigma \approx 10^{-5}$	$\sigma \approx 10^{-6}$	$\sigma \approx 10^{-7}$	$\sigma \approx 10^{-8}$	L2O
Avg. Pos. Err (%)	1135	205	67	15.8	1.2	7.4e-2
Std. Dev. (%)	1899	207	56	13.6	1.0	

$$\Delta\alpha = \begin{bmatrix} 0.000001267642974 \\ 0.058519465609471 \\ 0.171739075929753 \\ 0.220867007717396 \end{bmatrix} \times 10^{-4} \text{ rad}$$

$$\Delta\beta = \begin{bmatrix} -0.002975632870661 \\ -0.121581226539269 \\ -0.320789757534551 \\ 0.055884485142266 \end{bmatrix} \times 10^{-5} \text{ rad}$$

The following data in Table 9.5 was collected based on Monte-Carlo Analysis ($N = 100$ samples) with various levels of measurement noise injected into the 2nd-order measurement model.

The following data in Table 9.6 was collected based on Monte-Carlo Analysis ($N = 100$ samples) with various levels of measurement noise injected into the nonlinear angle measurements.

The tables show that the IROD algorithm provides acceptable percent position errors

Table 9.6: Percent Position Errors and Standard Deviation with varying magnitudes of measurement noise added to Nonlinear LOS angles for 100 Monte Carlo Runs (Leader-Follower 10 km LEO)

	$\sigma \approx 10^{-4}$	$\sigma \approx 10^{-5}$	$\sigma \approx 10^{-6}$	$\sigma \approx 10^{-7}$	$\sigma \approx 10^{-8}$	Nonlinear
Avg. Pos. Err (%)	785.4	223.8	73.7	16.6	5.6	5.4
Std. Dev. (%)	953.8	214.8	66.5	13.5	1.7	

Table 9.7: Azimuth and Elevation Angles from L2O environment and Nonlinear Dynamics for a Leader-Follower 100 km LEO case.

	L2O	Full Nonlinear
Azimuth Angles (rad)	-0.007252919596027	-0.007253043391941
	-0.006934363476905	-0.007153748311630
	-0.006482032457115	-0.007139600751983
	-0.006393095043842	-0.007254569698305
Elevation Angles (rad)	0.174526933197219	0.174532925199433
	0.082923180174327	0.082924991999720
	-0.098004619477766	-0.098007439653141
	-0.173574907842882	-0.173581920075426

for measurement noise less than or equal to $\sigma \approx 10^{-7} \text{ rad}$. For higher measurement noise levels, the IROD algorithm produces unacceptable estimation errors. Thus for 10 km separation, there are no cameras currently available that can be used to accurately estimate the initial relative states.

9.1.3 Leader-Follower 100 km

The angle measurements for a Leader-Follower 100 km relative motion configuration ($i = 10^\circ$, $e = 0$, $\Delta z = 0$, J_2 ON, $\Delta t = 1000 \text{ sec}$) with $N = 4$ observations are provided in Table 9.7.

Differencing the Azimuth and Elevation angles between the L2O environment and Nonlinear Dynamics yields

$$\Delta\alpha = \begin{bmatrix} 0.000123795913763 \\ 0.219384834724863 \\ 0.657568294867322 \\ 0.861474654463804 \end{bmatrix} \times 10^{-3} \text{ rad}$$

Table 9.8: Percent Position Errors and Standard Deviation with varying magnitudes of measurement noise added to L2O LOS angles for 100 Monte Carlo Runs (Leader-Follower 100 km LEO)

	$\sigma \approx 10^{-3}$	$\sigma \approx 10^{-4}$	$\sigma \approx 10^{-5}$	$\sigma \approx 10^{-6}$	$\sigma \approx 10^{-7}$	L2O
Avg. Pos. Err (%)	673.5	22.8	17.0	8.43	6.69	6.7
Std. Dev. (%)	4181.3	16.2	6.6	5.7	0.59	

Table 9.9: Percent Position Errors and Standard Deviation with varying magnitudes of measurement noise added to Nonlinear LOS angles for 100 Monte Carlo Runs (Leader-Follower 100 km LEO)

	$\sigma \approx 10^{-3}$	$\sigma \approx 10^{-4}$	$\sigma \approx 10^{-5}$	$\sigma \approx 10^{-6}$	$\sigma \approx 10^{-7}$	Nonlinear
Avg. Pos. Err (%)	217.1	22.2	13.2	7.14	6.39	6.4
Std. Dev. (%)	703.3	23.0	5.93	4.94	0.71	

$$\Delta\beta = \begin{bmatrix} -0.599200221382268 \\ -0.181182539295277 \\ 0.282017537472923 \\ 0.701223254356842 \end{bmatrix} \times 10^{-5} \text{ rad}$$

The following data in Table 9.8 was collected based on Monte-Carlo Analysis ($N = 100$ samples) with various levels of measurement noise injected into the 2nd-order measurement model.

The following data in Table 9.9 was collected based on Monte-Carlo Analysis ($N = 100$ samples) with various levels of measurement noise injected into the nonlinear angle measurements.

The table above shows the IROD algorithm produces acceptable position errors when the measurement noise is smaller than $\sigma \approx 10^{-3} \text{ rad}$. For larger magnitudes of measurement noise, the IROD algorithm is unable to accurately estimate the relative states. The results shown above are consistent with the expected position errors from [58]. Comparing these results with those found in Ref. [58] reiterate the fact that at larger separations the noise on the LOS measurements has a smaller effect on the IROD solution estimate. At close range, having even a small amount of measurement noise on the on-board camera can make the problem of relative orbit determination infeasible. These results are encouraging. They

Table 9.10: Azimuth and Elevation Angles from L2O environment and Nonlinear Dynamics for a Leader-Follower 500 km LEO case.

	L2O	Full Nonlinear
Azimuth Angles (rad)	-0.035480102265438	-0.035495935055422
	-0.025990322791439	-0.026305443180980
	-0.025582450030790	-0.026500164607881
	-0.034545050860747	-0.035753994896742
Elevation Angles (rad)	0.087192090776899	0.087266462599716
	0.039741339890699	0.039837382669864
	-0.050080028255630	-0.049956666971505
	-0.086691010329626	-0.086796173110891

show that at separations of 100 km or greater, the IROD algorithm can accurately estimate the initial relative states when the LOS measurements have noise levels found in current cameras used on-board spacecraft. At smaller separations, current cameras are not accurate enough to be used in initial relative orbit determination applications.

9.1.4 Leader-Follower 500 km

The angle measurements for a Leader-Follower 500 km relative motion configuration ($i = 5^\circ$, $e = 0.01$, $\Delta z = 0$, J_2 ON, $\Delta t = 1000 \text{ sec}$) with $N = 4$ observations are provided in Table 9.10.

Differencing the Azimuth and Elevation angles between the L2O environment and Nonlinear environment yields

$$\Delta\alpha = \begin{bmatrix} 0.000015832789984 \\ 0.000315120389541 \\ 0.000917714577090 \\ 0.001208944035995 \end{bmatrix} \text{ rad}$$

$$\Delta\beta = \begin{bmatrix} -0.074371822817249 \\ -0.096042779165639 \\ -0.123361284124844 \\ 0.105162781264725 \end{bmatrix} \times 10^{-3} \text{ rad}$$

The following data in Table 9.11 was collected based on Monte-Carlo Analysis ($N = 100$

Table 9.11: Percent Position Errors and Standard Deviation with varying magnitudes of measurement noise added to L2O LOS angles for 100 Monte Carlo Runs (Leader-Follower 500 km LEO)

	$\sigma \approx 10^{-3}$	$\sigma \approx 10^{-4}$	$\sigma \approx 10^{-5}$	$\sigma \approx 10^{-6}$	$\sigma \approx 10^{-7}$	L2O
Avg. Pos. Err (%)	56.2	18.5	18.5	18.4	18.4	18
Std. Dev. (%)	83.3	9.3	2.99	0.2	0.02	

Table 9.12: Percent Position Errors and Standard Deviation with varying magnitudes of measurement noise added to Nonlinear LOS angles for 100 Monte Carlo Runs (Leader-Follower 500 km LEO)

	$\sigma \approx 10^{-3}$	$\sigma \approx 10^{-4}$	$\sigma \approx 10^{-5}$	$\sigma \approx 10^{-6}$	$\sigma \approx 10^{-7}$	Nonlinear
Avg. Pos. Err (%)	56.5	33.8	36.5	36.5	36.5	36.5
Std. Dev. (%)	71.8	10.9	0.11	0.01	0.002	

samples) with various levels of measurement noise injected into the 2nd-order measurement model.

The following data in Table 9.12 was collected based on Monte-Carlo Analysis ($N = 100$ samples) with various levels of measurement noise injected into the nonlinear angle measurements.

The above tables show that the IROD algorithm can reliably determine the initial estimate when the measurement noise is below $\sigma \approx 10^{-3} \text{ rad}$. Larger magnitudes of error result in larger percent position errors for the IROD estimates.

9.2 Measurement Error Analysis for GEO

This section provides a few case studies of the performance of the IROD algorithm in GEO when the LOS measurements are injected with varying magnitudes of Gaussian white noise. Only a few cases are presented to test the IROD algorithm and investigate whether current camera technology used for on-board spacecraft imaging applications can be implemented for relative orbit determination. Cases similar to those in Section 9.1 are presented in this section except that the satellites are positioned at GEO. For each case, the azimuth and elevation angles are presented using the L2O environment and the full nonlinear environment, the angles differences are presented, and varying levels of Gaussian white noise measurement error are injected into LOS measurements in a Monte Carlo analysis. The

Table 9.13: Azimuth and Elevation Angles from L2O environment and Nonlinear Dynamics for a Leader-Follower 5 km GEO case.

	L2O	Full Nonlinear
Azimuth Angles (rad)	$\begin{bmatrix} -0.595187740938 \\ -0.591855231793 \\ -0.584025293028 \\ -0.577584843028 \end{bmatrix} \times 10^{-4}$	$\begin{bmatrix} -0.595187736121 \\ -0.593961709231 \\ -0.591446559617 \\ -0.591052348348 \end{bmatrix} \times 10^{-4}$
Elevation Angles (rad)	$\begin{bmatrix} 0.087266462394 \\ 0.066811070715 \\ 0.014853847558 \\ -0.044163040825 \end{bmatrix}$	$\begin{bmatrix} 0.087266462599 \\ 0.066811070746 \\ 0.014853847305 \\ -0.044163041161 \end{bmatrix}$

performance analysis completed in Ref. [58] is restricted to Low-Earth-Orbits only.

9.2.1 Leader-Follower 5 km

First, the angle measurements are tabulated for a Leader-Follower 5 km relative motion configuration ($i = 5^\circ$, $e = 0$, $\Delta z = 0$, J_2 ON, $\Delta t = 9600$ sec) with $N = 4$ observations.

Differencing the Azimuth and Elevation angles between the L2O environment and Nonlinear Dynamics yields

$$\Delta\alpha = \begin{bmatrix} -0.000000048175172 \\ 0.021064774377036 \\ 0.074212665894140 \\ 0.134675053195348 \end{bmatrix} \times 10^{-5} \text{ rad}$$

$$\Delta\beta = \begin{bmatrix} -0.205036806977255 \\ -0.030843980147743 \\ 0.253208589512388 \\ 0.335255295746961 \end{bmatrix} \times 10^{-9} \text{ rad}$$

The following data in Table 9.14 was collected based on Monte-Carlo Analysis ($N = 100$ samples) with various levels of measurement noise injected into the 2nd-order measurement model.

The following data in Table 9.15 was collected based on Monte-Carlo Analysis ($N = 100$ samples) with various levels of measurement noise injected into the nonlinear angle

Table 9.14: Percent Position Errors and Standard Deviation with varying magnitudes of measurement noise added to L2O LOS angles for 100 Monte Carlo Runs (Leader-Follower 5 km GEO)

	$\sigma \approx 10^{-7}$	$\sigma \approx 10^{-8}$	$\sigma \approx 10^{-9}$	$\sigma \approx 10^{-10}$	$\sigma \approx 10^{-11}$	L2O
Avg. Pos. Err (%)	798.4	65.7	4.8	6.81	2.16	8.9e-1
Std. Dev. (%)	1734.2	59.2	4.0	5.70	2.57	

Table 9.15: Percent Position Errors and Standard Deviation with varying magnitudes of measurement noise added to Nonlinear LOS angles for 100 Monte Carlo Runs (Leader-Follower 5 km GEO)

	$\sigma \approx 10^{-7}$	$\sigma \approx 10^{-8}$	$\sigma \approx 10^{-9}$	$\sigma \approx 10^{-10}$	$\sigma \approx 10^{-11}$	Nonlinear
Avg. Pos. Err (%)	1773	51.8	4.09	5.67	4.77	3.7
Std. Dev. (%)	3028	54.4	4.29	5.78	4.47	

measurements.

These tables show that the IROD algorithm produces acceptable percent position errors for measurement errors less than $\sigma \approx 10^{-8} \text{ rad}$. Any measurement errors larger than this, result in unacceptably large errors on the initial estimate.

9.2.2 Leader-Follower 10 km

Next, the angle measurements for a Leader-Follower 10 km relative motion configuration ($i = 5^\circ, e = 0, \Delta z = 0, J_2 \text{ ON}, \Delta t = 9600 \text{ sec}$) with $N = 4$ observations are provided in Table 9.16.

Differencing the Azimuth and Elevation angles between the L2O environment and Nonlinear Dynamics yields

Table 9.16: Azimuth and Elevation Angles from L2O environment and Nonlinear Dynamics for a Leader-Follower 10 km GEO case.

	L2O	Full Nonlinear
Azimuth Angles (rad)	$\begin{bmatrix} -0.119037547765 \\ -0.118399740991 \\ -0.116959124092 \\ -0.115761570102 \end{bmatrix} \times 10^{-3}$	$\begin{bmatrix} -0.119037548387 \\ -0.118821027592 \\ -0.118443398215 \\ -0.118455247318 \end{bmatrix} \times 10^{-3}$
Elevation Angles (rad)	$\begin{bmatrix} 0.087266461779 \\ 0.066811070375 \\ 0.014853847741 \\ -0.044163040308 \end{bmatrix}$	$\begin{bmatrix} 0.087266462599 \\ 0.066811070746 \\ 0.014853847304 \\ -0.044163041159 \end{bmatrix}$

Table 9.17: Percent Position Errors and Standard Deviation with varying magnitudes of measurement noise added to L2O LOS angles for 100 Monte Carlo Runs (Leader-Follower 10 km GEO)

	$\sigma \approx 10^{-7}$	$\sigma \approx 10^{-8}$	$\sigma \approx 10^{-9}$	$\sigma \approx 10^{-10}$	$\sigma \approx 10^{-11}$	L2O
Avg. Pos. Err (%)	139.0	19.5	5.24	4.90	4.39	4.7
Std. Dev. (%)	203.9	13.7	2.76	1.58	1.15	

Table 9.18: Percent Position Errors and Standard Deviation with varying magnitudes of measurement noise added to Nonlinear LOS angles for 100 Monte Carlo Runs (Leader-Follower 10 km GEO)

	$\sigma \approx 10^{-7}$	$\sigma \approx 10^{-8}$	$\sigma \approx 10^{-9}$	$\sigma \approx 10^{-10}$	$\sigma \approx 10^{-11}$	Nonlinear
Avg. Pos. Err (%)	160.2	24.8	4.79	4.23	4.32	4.8
Std. Dev. (%)	350.8	18.6	2.69	1.63	1.14	

$$\Delta\alpha = \begin{bmatrix} 0.00000062146810 \\ 0.042128660088494 \\ 0.148427412307111 \\ 0.269367721650584 \end{bmatrix} \times 10^{-5} \text{ rad}$$

$$\Delta\beta = \begin{bmatrix} -0.820147297297957 \\ -0.371490019301923 \\ 0.436872205078487 \\ 0.850340062252819 \end{bmatrix} \times 10^{-9} \text{ rad}$$

The following data in Table 9.17 was collected based on Monte-Carlo Analysis ($N = 100$ samples) with various levels of measurement noise injected into the 2nd-order measurement model.

The following data in Table 9.18 was collected based on Monte-Carlo Analysis ($N = 100$ samples) with various levels of measurement noise injected into the nonlinear angle measurements.

The tables above show that the IROD algorithm can find acceptable estimates when the measurement errors are less than $\sigma \approx 10^{-7}$. Larger magnitudes of measurement error yields large position errors on the IROD estimates.

Table 9.19: Azimuth and Elevation Angles from L2O environment and Nonlinear Dynamics for a Leader-Follower 100 km GEO case.

	L2O	Full Nonlinear
Azimuth Angles (rad)	-0.001190374920754	-0.001190375478897
	-0.001184263947994	-0.001188468072306
	-0.001170976437346	-0.001185820670371
	-0.001159786245259	-0.001186755559581
Elevation Angles (rad)	0.087266380585009	0.087266462599716
	0.066811011133262	0.066811070745891
	0.014853838770885	0.014853847303974
	-0.044162999440064	-0.044163041158496

9.2.3 Leader-Follower 100 km

The angle measurements for a Leader-Follower 100 km relative motion configuration ($i = 5^\circ$, $e = 0$, $\Delta z = 0$, J_2 ON, $\Delta t = 9600 \text{ sec}$) with $N = 4$ observations are provided in Table 9.19.

Differencing the Azimuth and Elevation angles between the L2O environment and Nonlinear Dynamics yields

$$\Delta\alpha = \begin{bmatrix} 0.000005581429750 \\ 0.042041243121956 \\ 0.148442330253483 \\ 0.269693143215299 \end{bmatrix} \times 10^{-4} \text{ rad}$$

$$\Delta\beta = \begin{bmatrix} -0.820147074837019 \\ -0.596126291524390 \\ -0.085330888691809 \\ 0.417184322504260 \end{bmatrix} \times 10^{-7} \text{ rad}$$

The following data in Table 9.20 was collected based on Monte-Carlo Analysis ($N = 100$ samples) with various levels of measurement noise injected into the 2nd-order measurement model.

The following data in Table 9.21 was collected based on Monte-Carlo Analysis ($N = 100$ samples) with various levels of measurement noise injected into the nonlinear angle measurements.

Table 9.20: Percent Position Errors and Standard Deviation with varying magnitudes of measurement noise added to L2O LOS angles for 100 Monte Carlo Runs (Leader-Follower 100 km GEO)

	$\sigma \approx 10^{-5}$	$\sigma \approx 10^{-6}$	$\sigma \approx 10^{-7}$	$\sigma \approx 10^{-8}$	$\sigma \approx 10^{-9}$	L2O
Avg. Pos. Err (%)	168.9	24.66	4.60	3.35	3.83	3.9
Std. Dev. (%)	167.3	25.08	3.46	0.971	0.047	

Table 9.21: Percent Position Errors and Standard Deviation with varying magnitudes of measurement noise added to Nonlinear LOS angles for 100 Monte Carlo Runs (Leader-Follower 100 km GEO)

	$\sigma \approx 10^{-5}$	$\sigma \approx 10^{-6}$	$\sigma \approx 10^{-7}$	$\sigma \approx 10^{-8}$	$\sigma \approx 10^{-9}$	Nonlinear
Avg. Pos. Err (%)	179.0	26.73	4.51	3.73	4.09	4.1
Std. Dev. (%)	180.0	26.81	3.36	0.77	0.06	

These tables show that measurement errors larger than $\sigma \approx 10^{-6} \text{ rad}$ yield unacceptable position errors. These measurement errors are still too large for current cameras to be used for IROD applications at GEO.

9.2.4 Leader-Follower 500 km

The angle measurements for a Leader-Follower 500 km relative motion configuration ($i = 5^\circ$, $e = 0$, $\Delta z = 0$, J_2 ON, $\Delta t = 9600 \text{ sec}$) with $N = 4$ observations are provided in Table 9.22.

Differencing the Azimuth and Elevation angles between the L2O environment and Nonlinear Dynamics yields

Table 9.22: Azimuth and Elevation Angles from L2O environment and Nonlinear Dynamics for a Leader-Follower 500 km GEO case.

	L2O	Full Nonlinear
Azimuth Angles (rad)	-0.005951807119753	-0.005951876881958
	-0.005921574560247	-0.005942454633564
	-0.005855414633048	-0.005929719609008
	-0.005799139640593	-0.005934756740968
Elevation Angles (rad)	0.087264412245892	0.087266462599716
	0.066809533442287	0.066811070745855
	0.014853522469069	0.014853847303952
	-0.044162090070610	-0.044163041158242

Table 9.23: Percent Position Errors and Standard Deviation with varying magnitudes of measurement noise added to L2O LOS angles for 100 Monte Carlo Runs (Leader-Follower 500 km GEO)

	$\sigma \approx 10^{-3}$	$\sigma \approx 10^{-4}$	$\sigma \approx 10^{-5}$	$\sigma \approx 10^{-6}$	$\sigma \approx 10^{-7}$	L2O
Avg. Pos. Err (%)	18871	60.58	23.2	7.84	8.21	8.2
Std. Dev. (%)	68451	38.89	19.2	1.65	0.10	

Table 9.24: Percent Position Errors and Standard Deviation with varying magnitudes of measurement noise added to Nonlinear LOS angles for 100 Monte Carlo Runs (Leader-Follower 500 km GEO)

	$\sigma \approx 10^{-3}$	$\sigma \approx 10^{-4}$	$\sigma \approx 10^{-5}$	$\sigma \approx 10^{-6}$	$\sigma \approx 10^{-7}$	Nonlinear
Avg. Pos. Err (%)	42232	60.75	24.8	8.78	9.07	9.2
Std. Dev. (%)	89001	42.35	18.6	1.45	0.15	

$$\Delta\alpha = \begin{bmatrix} 0.000069762205479 \\ 0.020880073317282 \\ 0.074304975960427 \\ 0.135617100375044 \end{bmatrix} \times 10^{-3} \text{ rad}$$

$$\Delta\beta = \begin{bmatrix} -0.205035382452867 \\ -0.153730356816650 \\ -0.032483488295043 \\ 0.095108763242119 \end{bmatrix} \times 10^{-5} \text{ rad}$$

The following data in Table 9.23 was collected based on Monte-Carlo Analysis ($N = 100$ samples) with various levels of measurement noise injected into the 2nd-order measurement model.

The following data in Table 9.24 was collected based on Monte-Carlo Analysis ($N = 100$ samples) with various levels of measurement noise injected into the nonlinear angle measurements.

These tables show that the IROD algorithm is able to find accurate estimates when the LOS measurement error is less than $\sigma \approx 10^{-4} \text{ rad}$. This is barely attainable with the best, most accurate cameras available for space imaging applications. Cameras that have noise magnitude at levels of $\sigma \approx 10^{-5} \text{ rad}$ are expensive but available currently.

From the GEO test cases above, it is evident that IROD applications are more sensitive to measurement noise at GEO than conducting IROD at LEO. Either a higher fidelity, more accurate and ultimately more expensive camera must be used for IROD at GEO or the distance of separation between satellites must be extended for more accurate and reliable results. Future research should include investigating the role of measurement errors on a wider range of relative motion cases, satellite separations and noise magnitudes. Special consideration should be prioritized for relative motion regimes where current camera technology can be used to find acceptable IROD estimates.

CHAPTER 10
GEOSTATIONARY ORBIT RESULTS

All of the previous relative motion analysis have been set at LEO. The utility of the IROD solution can be extended by implementing it in Geostationary orbits. For the cases shown in Table 10.1, the chief semi-major axis is $42,164 \text{ km}$ and the eccentricity is zero ($e = 0$). The effect of the J_2 perturbations is small at GEO and the data below include the J_2 perturbations in the dynamics and in the IROD algorithm.

Each of the tables below show three different relative motion trajectory configurations (Leader-Follower, Flyby, Football), at three different downrange separations, for a matrix of low inclination angles and low eccentricity values. The range of inclinations and eccentricities is smaller for GEO than LEO since most GEO satellites lie within this small range of inclinations and eccentricities. Some cross-track motion is also introduced (Δz) to the deputy vehicle. The tables below tabulate the number of feasible solutions found by the IROD algorithm (Num Sol. column), the percent position error of the best initial IROD estimate (IROD column) and the percent position error of the iteratively improved IROD estimate (Q column). The J_2 perturbations are turned on for all cases.

10.1 N=4 Observations, Nonlinear Dynamics, $\Delta t = 9600 \text{ sec}$

The IROD performance with no cross-track motion ($\Delta z = 0\%$) and $N = 4$ observations is shown in Tables 10.1-10.2. It can be seen that the IROD algorithm is able to accurately estimate the initial relative motion states for the cases considered at GEO.

The IROD performance with cross-track motion ($\Delta z = 10\%$) for a range of relative motion trajectories, inclinations and eccentricities acceptable for GEO satellites is shown in Tables 10.3-10.4. The performance is good for almost all of the relative motion cases.

Table 10.1: Percent Position Errors, $N = 4$, $\Delta t = 9600 s$, $\Delta z = 0\%$, $e = 0$

	Dwn. Sep.	$i = 0$			$i = 5^\circ$		
		Num Sol.	IROD	Q	Num Sol.	IROD	Q
Leader-Follower	5 km	4	3.7	3.7	4	3.7	3.7
	50 km	4	2.1e-1	7.1e-4	4	2.6	2.6
	500 km	4	1.9	1.2e-3	4	8.6	9.2
Flyby	5 km	1	3.1	3.1	1	3.7	3.7
	50 km	5	3	3	1	3.7	3.7
	500 km	5	2.9	2.9	1	5.2	5.2
Football	5 km	6	5.6	5.6	2	5.1	5.1
	50 km	6	5.6	5.5	2	5.1	5.1
	500 km	6	5.5	4.7	2	7.2e-1	7.3e-1

Table 10.2: Percent Position Errors, $N = 4$, $\Delta t = 9600 s$, $\Delta z = 0\%$, $e = 0.001$

	Dwn. Sep.	$i = 0$			$i = 5^\circ$		
		Num Sol.	IROD	Q	Num Sol.	IROD	Q
Leader-Follower	5 km	2	8.2	8.2	2	11	11
	50 km	2	3.0e-1	5.1e-1	2	1.7e-2	1.7e-2
	500 km	4	1.8	1.3e-1	4	17	17
Flyby	5 km	1	3.0	3.0	1	3.6	3.6
	50 km	5	3.0	3.0	1	3.6	3.6
	500 km	5	2.8	2.9	1	5.1	5.1
Football	5 km	6	5.5	5.5	2	5.0	5.0
	50 km	6	5.5	5.4	2	5.0	5.0
	500 km	6	5.4	4.6	2	6.5e-1	6.5e-1

Table 10.3: Percent Position Errors, $N = 4$, $\Delta t = 9600 s$, $\Delta z = 10\%$, $e = 0$

	Dwn. Sep.	$i = 0$			$i = 5^\circ$		
		Num Sol.	IROD	Q	Num Sol.	IROD	Q
Leader-Follower	5 km	3	4.7e-3	4.7e-3	3	46	44
	50 km	3	2.6e-2	3.4e-2	3	49	49
	500 km	7	3.4e-1	3.3e-1	3	23	23
Flyby	5 km	1	2.7	2.7	1	2.6	2.6
	50 km	5	2.7	2.7	1	2.6	2.6
	500 km	5	2.1	2.3	1	4.3	4.3
Football	5 km	6	5.8	5.8	2	5.7	5.7
	50 km	6	5.8	5.7	2	5.7	5.7
	500 km	6	4.6	4.9	2	1.5	1.5

Table 10.4: Percent Position Errors, $N = 4$, $\Delta t = 9600 s$, $\Delta z = 10\%$, $e = 0.001$

	Dwn. Sep.	$i = 0$			$i = 5^\circ$		
		Num Sol.	IROD	Q	Num Sol.	IROD	Q
Leader-Follower	5 km	3	3.6e-2	3.6e-2	1	1.8e-1	2.6e-1
	50 km	3	4.8e-2	5.6e-2	1	11	10
	500 km	7	3.1e-1	3.1e-1	3	29	29
Flyby	5 km	1	2.7	2.7	1	2.6	2.6
	50 km	5	2.6	2.6	1	2.6	2.6
	500 km	5	2.0	2.3	1	4.2	4.2
Football	5 km	6	5.7	5.7	2	5.6	5.6
	50 km	6	5.7	5.6	2	5.6	5.6
	500 km	6	4.5	4.9	2	1.4	1.5

Table 10.5: Percent Position Errors, $N = 13$, $\Delta t = 2400 s$, $\Delta z = 0\%$, $e = 0$

	Dwn. Sep.	$i = 0$			$i = 5^\circ$		
		Num Sol.	IROD	Q	Num Sol.	IROD	Q
Leader-Follower	5 km	4	1.8	1.8	4	6.6	6.7
	50 km	4	1.8e-1	1.4e-3	4	1.4e-1	1.4e-1
	500 km	4	1.7	7.2e-2	4	1.7	1.5e-1
Flyby	5 km	5	2.9	3.1	1	2.4	2.5
	50 km	5	2.9	3.1	1	2.5	2.5
	500 km	5	2.8	3.0	9	2.7	2.4
Football	5 km	6	7.6	6.4	3	22	22
	50 km	6	7.6	6.4	7	22	22
	500 km	6	7.6	5.9	7	87	19

10.2 $N=13$ Observations, Nonlinear Dynamics, $\Delta t = 2400 sec$

Now the same set of parameters that were tested with $N = 4$ observations are tested when $N = 13$ observations are available within the same time interval. The final time is kept constant and the measurement interval is decreased. The same relative motion trajectories are considered over the same range of inclinations and eccentricities. The IROD performance with no cross-track motion ($\Delta z = 0\%$) and $N = 13$ observations is shown in Tables 10.5-10.6. It can be seen that the IROD algorithm is able to accurately estimate the initial relative motion states for the cases considered at GEO.

The IROD performance with cross-track motion ($\Delta z = 10\%$) for a range of relative motion trajectories, inclinations and eccentricities acceptable for GEO satellites is shown in Tables 10.7-10.8. The performance is good for almost all of the relative motion cases.

Table 10.6: Percent Position Errors, $N = 13$, $\Delta t = 2400 s$, $\Delta z = 0\%$, $e = 0.001$

	Dwn. Sep.	$i = 0$			$i = 5^\circ$		
		Num Sol.	IROD	Q	Num Sol.	IROD	Q
Leader-Follower	5 km	2	9.3	9.3	4	6.6	6.7
	50 km	2	3.5e-1	4.9e-1	4	1.4e-1	1.3e-1
	500 km	4	1.6	8.3e-1	4	1.7	1.4e-1
Flyby	5 km	5	2.8	3.0	1	2.3	2.4
	50 km	5	2.7	2.9	1	2.3	2.4
	500 km	5	2.4	2.5	9	2.6	2.6
Football	5 km	6	7.5	6.3	3	21	22
	50 km	6	7.5	6.3	7	21	22
	500 km	6	7.4	5.7	7	83	19

Table 10.7: Percent Position Errors, $N = 13$, $\Delta t = 2400 s$, $\Delta z = 10\%$, $e = 0$

	Dwn. Sep.	$i = 0$			$i = 5^\circ$		
		Num Sol.	IROD	Q	Num Sol.	IROD	Q
Leader-Follower	5 km	5	2.4	2.4	7	14	11
	50 km	5	1.7e-1	3.8e-2	7	12	12
	500 km	9	1.7	6.5	8	4.5	4.3
Flyby	5 km	5	2.8	2.9	5	2.4	2.5
	50 km	5	2.8	2.9	5	2.5	2.5
	500 km	5	2.7	2.8	9	2.7	2.4
Football	5 km	5	30	30	5	20	21
	50 km	5	31	31	9	20	21
	500 km	5	1.4e2	31	7	20	22

Table 10.8: Percent Position Errors, $N = 13$, $\Delta t = 2400 s$, $\Delta z = 10\%$, $e = 0.001$

	Dwn. Sep.	$i = 0$			$i = 5^\circ$		
		Num Sol.	IROD	Q	Num Sol.	IROD	Q
Leader-Follower	5 km	5	9.0e-1	8.5e-2	7	1.3e-1	1.0e-2
	50 km	5	7.1e-1	7.1e-1	7	3.5	3.4e-2
	500 km	9	1.6	5.4e-1	8	12	12
Flyby	5 km	5	2.8	2.8	5	2.4	2.4
	50 km	5	2.8	2.8	5	2.4	2.4
	500 km	5	2.6	2.7	9	2.7	2.7
Football	5 km	5	30	30	5	20	21
	50 km	5	31	31	9	20	21
	500 km	5	1.4e2	31	7	20	22

Table 10.9: Percent Position Errors, $N = 25$, $\Delta t = 1200$ s, $\Delta z = 0\%$, $e = 0$

	Dwn. Sep.	$i = 0$			$i = 5^\circ$		
		Num Sol.	IROD	Q	Num Sol.	IROD	Q
Leader-Follower	5 km	4	1.5	1.5	4	6.9	7.1
	50 km	4	1.8e-1	6.8e-4	4	1.4e-1	1.4e-1
	500 km	4	1.7	1.8e-1	4	1.7	3.2e-1
Flyby	5 km	5	2.9	3.1	1	2.4	2.6
	50 km	5	2.8	3.1	1	2.4	2.5
	500 km	5	2.7	3.0	9	2.6	2.4
Football	5 km	6	7.8	6.2	3	21	22
	50 km	6	7.8	6.2	7	21	22
	500 km	6	7.7	5.6	7	1.5e2	1.3

Table 10.10: Percent Position Errors, $N = 25$, $\Delta t = 1200$ s, $\Delta z = 0\%$, $e = 0.001$

	Dwn. Sep.	$i = 0$			$i = 5^\circ$		
		Num Sol.	IROD	Q	Num Sol.	IROD	Q
Leader-Follower	5 km	2	11	11	4	6.1e-1	4.2e-1
	50 km	2	3.6e-1	5.0e-1	4	1.0	1.0
	500 km	4	1.6	1.1e-1	4	1.6	9.7e-1
Flyby	5 km	5	2.8	3.0	1	2.3	2.4
	50 km	5	2.7	3.0	1	2.3	2.4
	500 km	5	2.6	2.9	9	2.5	2.5
Football	5 km	6	7.7	6.1	3	21	22
	50 km	6	7.7	6.1	7	21	22
	500 km	6	7.6	5.5	7	1.4e2	1.4

10.3 $N=25$ Observations, Nonlinear Dynamics, $\Delta t = 1200$ sec

Next, the same set of relative motion cases is tested with more observations, $N = 25$. The total time is kept constant and the time interval between measurements is decreased. The same range of relative motion trajectories, inclinations and eccentricities are considered and the percent position errors are tabulated for these cases. The IROD performance with no cross-track motion ($\Delta z = 0\%$) and $N = 25$ observations is shown in Tables 10.9-10.10. It can be seen that the IROD algorithm is able to accurately estimate the initial relative motion states for the cases considered at GEO.

The IROD performance with cross-track motion ($\Delta z = 10\%$) for a range of relative motion trajectories, inclinations and eccentricities acceptable for GEO satellites is shown in Tables 10.11-10.12. The performance is good for almost all of the relative motion cases.

These GEO cases show that the IROD algorithm's capacity can be expanded to GEO

Table 10.11: Percent Position Errors, $N = 25$, $\Delta t = 1200 s$, $\Delta z = 10\%$, $e = 0$

	Dwn. Sep.	$i = 0$			$i = 5^\circ$		
		Num Sol.	IROD	Q	Num Sol.	IROD	Q
Leader-Follower	5 km	5	2.8e-1	9.7e-3	7	14	13
	50 km	5	1.4e-1	1.1e-2	7	12	12
	500 km	9	1.7	6.8e-1	8	4.4	4.4
Flyby	5 km	5	2.8	2.9	5	2.4	2.5
	50 km	5	2.8	2.9	5	2.4	2.5
	500 km	5	2.6	2.8	9	2.7	2.4
Football	5 km	5	30	30	5	20	21
	50 km	5	31	31	9	20	21
	500 km	5	41	31	7	20	22

Table 10.12: Percent Position Errors, $N = 25$, $\Delta t = 1200 s$, $\Delta z = 0\%$, $e = 0$

	Dwn. Sep.	$i = 0$			$i = 5^\circ$		
		Num Sol.	IROD	Q	Num Sol.	IROD	Q
Leader-Follower	5 km	5	5.2e-1	1.5e-1	7	1.2e-1	4.2e-2
	50 km	5	1.0	1.0	7	4.4	3.9e-2
	500 km	9	1.5	5.5e-1	8	12	12
Flyby	5 km	5	2.7	2.8	5	2.4	2.4
	50 km	5	2.7	2.8	5	2.4	2.4
	500 km	5	2.6	2.7	9	2.6	2.6
Football	5 km	5	30	30	5	20	21
	50 km	5	31	31	9	20	21
	500 km	5	41	31	7	20	22

satellites, determining relative states of debris and neighboring, unknown satellite bodies in the GEO region of space. When the IROD algorithm is restricted to small inclinations and eccentricities, the algorithm is able to find solutions with an acceptable level of error for almost all cases. These results show the utility of this algorithm for GEO initial relative orbit determination scenarios.

10.4 N=4 Observations, Nonlinear Dynamics, Excluding J_2 from IROD

As previously stated, one of the main motivations of this new formulation of the IROD algorithm was to include J_2 perturbation effects. Previous research has shown that the J_2 perturbation has a large effect on relative motion at LEO [57]. At LEO, the J_2 perturbation is a more dominant effect than other spherical harmonic perturbations or perturbations due to third-bodies [7] but is less significant as the radius of the orbit increases. Still the J_2 perturbation has some effect at GEO and if the IROD algorithm's main utility will be orbit determination at GEO, characterizing whether the J_2 effect is significant at GEO in this application is vital. The question to be answered in this section is: Does neglecting the inclusion of J_2 effects at GEO affect the performance of the IROD algorithm?

Relative motion cases are presented below, similar to the previously shown tables above, with varying downrange separations, inclinations, eccentricities, relative motion configurations and cross-track separations.

For the relative motion cases in Tables 10.13-10.16, several trends can be evident. Although not including the J_2 perturbation does increase the error in some solutions, the effect is not as stark as for the previously presented LEO cases. Out of all of the above cases, only one case results in a NO SOLUTION from the IROD algorithm with all of the other solutions being poor (marked in blue) or good (marked in black). It is also interesting to note that the same trend is evident in the LEO cases, namely the percent position errors decrease as the relative separation of the satellite increases, is also evident in the above tables. Once again, the effects of relative J_2 on LOS measurements are more significant at closer separations at GEO than at larger separations.

Table 10.13: Percent Position Errors, $N = 4$, $\Delta t = 9600 s$, $\Delta z = 0\%$, $e = 0$, NO IROD J_2

	Dwn. Sep.	$i = 0$			$i = 5^\circ$		
		Num Sol.	IROD	Q	Num Sol.	IROD	Q
Leader-Follower	5 km	4	2.5	2.5	0	NS	NS
	50 km	4	1.9e-1	6.4e-4	4	1.8	1.7
	500 km	4	1.9	1.2e-3	4	8.7	9.1
Flyby	5 km	1	26	26	1	28	28
	50 km	5	5.4	5.4	1	6.1	6.1
	500 km	5	3.2	3.2	1	5.5	5.4
Football	5 km	6	35	35	2	35	35
	50 km	6	1.5	1.4	2	1.1	1.1
	500 km	5	5.1	4.3	2	2.3e-1	2.4e-1

Table 10.14: Percent Position Errors, $N = 4$, $\Delta t = 9600 s$, $\Delta z = 0\%$, $e = 0.001$, NO IROD J_2

	Dwn. Sep.	$i = 0$			$i = 5^\circ$		
		Num Sol.	IROD	Q	Num Sol.	IROD	Q
Leader-Follower	5 km	2	20	20	2	21	22
	50 km	2	24	24	2	24	25
	500 km	4	2.1	2.7e-1	4	17	17
Flyby	5 km	1	26	26	1	28	28
	50 km	5	5.3	5.3	1	6.0	6.0
	500 km	5	3.1	3.1	1	5.3	5.3
Football	5 km	6	35	35	2	34	34
	50 km	6	1.4	1.3	2	1.0	1.0
	500 km	6	5.0	4.1	2	1.5e-1	1.7e-1

Table 10.15: Percent Position Errors, $N = 4$, $\Delta t = 9600 s$, $\Delta z = 10\%$, $e = 0$, NO IROD J_2

	Dwn. Sep.	$i = 0$			$i = 5^\circ$		
		Num Sol.	IROD	Q	Num Sol.	IROD	Q
Leader-Follower	5 km	3	4.2e-2	4.2e-2	3	51	49
	50 km	3	6.3e-2	7.1e-2	3	49	49
	500 km	7	3.1e-1	3.1e-1	3	24	24
Flyby	5 km	1	24	24	1	22	22
	50 km	5	4.9	4.9	1	4.6	4.6
	500 km	5	2.3	2.5	1	4.5	4.5
Football	5 km	6	34	34	2	33	33
	50 km	6	1.7	1.6	2	1.7	1.7
	500 km	6	4.3	4.5	2	1.0	1.0

Table 10.16: Percent Position Errors, $N = 4$, $\Delta t = 9600 s$, $\Delta z = 10\%$, $e = 0.001$, NO IROD J_2

	Dwn. Sep.	$i = 0$			$i = 5^\circ$		
		Num Sol.	IROD	Q	Num Sol.	IROD	Q
Leader-Follower	5 km	3	13	13	1	3.7	3.7
	50 km	3	1.2	1.2	1	9.8	9.2
	500 km	7	3.8e-1	3.8e-1	3	29	29
Flyby	5 km	1	25	25	1	23	23
	50 km	5	4.9	4.9	1	4.7	4.7
	500 km	5	2.3	2.6	1	4.4	4.4
Football	5 km	6	34	34	2	33	33
	50 km	6	1.7	1.5	2	1.6	1.6
	500 km	6	4.1	4.4	2	9.9e-1	1.0

Table 10.17: Percent Position Errors, $N = 13$, $\Delta t = 2400 s$, $\Delta z = 0\%$, $e = 0$, NO IROD J_2

	Dwn. Sep.	$i = 0$			$i = 5^\circ$		
		Num Sol.	IROD	Q	Num Sol.	IROD	Q
Leader-Follower	5 km	4	7.6e-1	7.6e-1	5	9.8	9.9
	50 km	4	1.6e-1	1.3e-3	4	3.6e-2	2.8e-2
	500 km	4	1.7	2.9e-3	4	1.6	1.1e-1
Flyby	5 km	5	22	26	1	9.8	11
	50 km	5	4.8	5.3	1	3.1	3.3
	500 km	5	2.9	3.1	9	2.7	2.5
Football	5 km	6	31	33	3	19	19
	50 km	6	3.6	2.3	7	17	18
	500 km	6	7.0	5.2	7	82	19

10.5 $N=13$ Observations, Nonlinear Dynamics, Excluding J_2 from IROD

The previous cases are re-run with $N = 13$ observations and J_2 perturbations turned off in the IROD algorithm but included when generating the LOS measurements.

Tables 10.17-10.20 show the percent position errors as more measurements are included in the IROD solution. The $N = 13$ cases shown above are consistent with the $N = 4$ cases (i.e. an increase in the number of observations does not mean a noticeable increase in the percent position error). Again, neglecting the J_2 perturbations in the IROD algorithm often yields incorrect solutions with high position errors compared to previous cases when the J_2 effects were modeled in the IROD algorithm. Also, the cases where the separation is close seem to be the worst cases in terms of percent position error and as the separation increases between satellites, the errors decrease in the IROD estimate.

Table 10.18: Percent Position Errors, $N = 13$, $\Delta t = 2400 s$, $\Delta z = 0\%$, $e = 0.001$, NO IROD J_2

	Dwn. Sep.	$i = 0$			$i = 5^\circ$		
		Num Sol.	IROD	Q	Num Sol.	IROD	Q
Leader-Follower	5 km	2	20	35	4	22	28
	50 km	2	24	24	4	7.6	9.8
	500 km	4	1.8	2.8e-1	4	2.5	1.9
Flyby	5 km	5	23	26	1	9.7	11
	50 km	5	4.8	5.3	1	3.1	3.3
	500 km	5	2.9	3.1	9	2.7	2.7
Football	5 km	6	31	33	3	19	20
	50 km	6	3.6	2.3	7	17	18
	500 km	6	7.0	5.2	7	79	20

Table 10.19: Percent Position Errors, $N = 13$, $\Delta t = 2400 s$, $\Delta z = 10\%$, $e = 0$, NO IROD J_2

	Dwn. Sep.	$i = 0$			$i = 5^\circ$		
		Num Sol.	IROD	Q	Num Sol.	IROD	Q
Leader-Follower	5 km	5	4.4	4.4	7	13	13
	50 km	5	8.2e-1	8.2e-1	7	12	12
	500 km	9	1.7	7.0e-1	8	4.5	4.5
Flyby	5 km	5	20	19	5	6.3	7.4
	50 km	5	4.2	4.4	5	2.8	3.0
	500 km	5	2.8	2.9	9	2.7	2.4
Football	5 km	5	32	12	5	22	22
	50 km	5	27	26	9	16	16
	500 km	5	1.4e2	31	7	20	21

Table 10.20: Percent Position Errors, $N = 13$, $\Delta t = 2400 s$, $\Delta z = 10\%$, $e = 0.001$, NO IROD J_2

	Dwn. Sep.	$i = 0$			$i = 5^\circ$		
		Num Sol.	IROD	Q	Num Sol.	IROD	Q
Leader-Follower	5 km	5	9.0	7.1	7	10	10
	50 km	5	5.7	5.4	7	7.0	1.6
	500 km	9	1.7	6.6e-1	8	12	12
Flyby	5 km	5	20	19	5	6.1	7.2
	50 km	5	4.2	4.4	5	2.8	2.9
	500 km	5	2.7	2.9	9	2.7	2.7
Football	5 km	5	31	12	5	22	22
	50 km	5	27	26	9	16	16
	500 km	5	1.4e2	31	7	20	21

Table 10.21: Percent Position Errors, $N = 25$, $\Delta t = 1200 s$, $\Delta z = 0\%$, $e = 0$, NO IROD J_2

	Dwn. Sep.	$i = 0$			$i = 5^\circ$		
		Num Sol.	IROD	Q	Num Sol.	IROD	Q
Leader-Follower	5 km	4	4.3e-1	4.3e-1	5	9.8	9.9
	50 km	4	1.6e-1	9.1e-4	4	4.0e-2	3.5e-2
	500 km	4	1.6	1.4e-1	4	1.6	3.0e-1
Flyby	5 km	5	22	26	1	9.4	11
	50 km	5	4.8	5.3	1	3.1	3.4
	500 km	5	2.9	3.1	9	2.6	2.5
Football	5 km	6	30	33	3	19	19
	50 km	6	3.9	2.1	7	17	18
	500 km	6	7.2	5.1	7	1.4e2	1.3

10.6 N=25 Observations, Nonlinear Dynamics, Excluding J_2 from IROD

Now the same cases are considered with more measurements. The same cases as above are re-run with $N = 25$ observations.

The results from Tables 10.21-10.24 are consistent with the previous trends. Increasing the number of observations does not noticeably decrease the performance of the IROD algorithm although these cases show that the IROD algorithm does perform worse when J_2 is not included in the algorithm. Also, the IROD algorithm is more accurate at larger satellite separations than at small separations due to the effect of relative J_2 on LOS measurements at GEO. Although the results are worse when the effects of J_2 are not included in the IROD algorithm for GEO objects, the percent position errors are acceptable compared to the LEO results where J_2 is neglected. This is consistent with the fact that J_2 is not as strong a perturbation on the relative motion at GEO than it is at LEO.

In previous chapters, the IROD algorithm was tested at LEO and results showed that the IROD algorithm was able to find good estimates of the initial relative states for cases with low eccentricity and low inclinations. Since most satellites at GEO have low inclination and low eccentricity, it seemed like the IROD algorithm would lend itself well when testing relative motion trajectories at GEO. So, this chapter presents a range of relative motion cases at GEO, varying the inclinations, eccentricities, relative separations. For almost every case, the IROD algorithm performs well, accurately estimating the initial relative states with small percent position errors. Although the effect of the J_2 perturbation is smaller at GEO

Table 10.22: Percent Position Errors, $N = 25$, $\Delta t = 1200 s$, $\Delta z = 0\%$, $e = 0.001$, NO IROD J_2

	Dwn. Sep.	$i = 0$			$i = 5^\circ$		
		Num Sol.	IROD	Q	Num Sol.	IROD	Q
Leader-Follower	5 km	2	20	34	4	22	28
	50 km	2	24	24	4	7.2	9.3
	500 km	4	1.8	2.8e-1	4	1.2	6.9e-1
Flyby	5 km	5	22	27	1	9.2	11
	50 km	5	4.8	5.4	1	3.0	3.3
	500 km	5	2.8	3.1	9	2.6	2.6
Football	5 km	6	30	33	3	19	19
	50 km	6	3.8	2.1	7	17	18
	500 km	6	7.2	5.1	7	1.4e2	1.4

Table 10.23: Percent Position Errors, $N = 25$, $\Delta t = 1200 s$, $\Delta z = 10\%$, $e = 0$, NO IROD J_2

	Dwn. Sep.	$i = 0$			$i = 5^\circ$		
		Num Sol.	IROD	Q	Num Sol.	IROD	Q
Leader-Follower	5 km	5	1.8	1.8	7	13	13
	50 km	5	7.8e-1	7.8e-1	7	12	12
	500 km	9	1.7	7.3e-1	8	4.4	4.4
Flyby	5 km	5	20	19	5	5.9	7.4
	50 km	5	4.1	4.4	5	2.8	3.0
	500 km	5	2.7	2.9	9	2.7	2.4
Football	5 km	5	31	12	5	22	22
	50 km	5	27	26	9	15	16
	500 km	5	40	31	7	20	21

Table 10.24: Percent Position Errors, $N = 25$, $\Delta t = 1200 s$, $\Delta z = 10\%$, $e = 0.001$, NO IROD J_2

	Dwn. Sep.	$i = 0$			$i = 5^\circ$		
		Num Sol.	IROD	Q	Num Sol.	IROD	Q
Leader-Follower	5 km	5	9.4	7.4	7	13	13
	50 km	5	5.5	5.5	7	6.6	1.5
	500 km	9	1.6	6.6e-1	8	12	12
Flyby	5 km	5	20	19	5	5.7	7.3
	50 km	5	4.1	4.4	5	2.7	2.9
	500 km	5	2.7	2.9	9	2.6	2.7
Football	5 km	5	31	12	5	22	22
	50 km	5	27	26	9	15	16
	500 km	5	40	31	7	19	21

than at LEO, the question of whether the IROD algorithm should include J_2 effects at GEO is important. Multiple relative motion cases are presented that show the importance of including J_2 perturbations in the IROD algorithm especially if the separation between the observer and observed satellite is small. The algorithm has shown its utility when applied to GEO initial relative orbit determination cases.

CHAPTER 11

SUMMARY AND CONCLUSIONS

With an increase in space debris in the recent years, the number of untracked space objects is increasing. Initial relative orbit determination can be used as a vital tool to characterize the orbits of neighboring objects to track satellites of interest and avoid collisions with debris. Previous research has shown that a spherical coordinate frame has definite advantages and improved accuracy when formulating relative motion equations over a Cartesian coordinate frame formulation.

Chapter 2 laid the groundwork for the previous research in orbital relative motion in Cartesian coordinates. This chapter also introduced many of the common relative motion trajectories that are referenced in orbital relative motion literature and used for test cases in the subsequent chapters. The Hill-Clohessy-Wiltshire equations were derived with special attention focused on the linearizing assumptions that are used to derive these relative motion equations in Cartesian Coordinates. In order to get a closed-form solution for the relative motion equations in Cartesian coordinates, the HCW equations make the linearizing assumption that the two neighboring satellites be close to each other. So, the relative position and velocity states are assumed to be small to first order and the chief orbit is assumed to be circular. The Tshauer-Hempel equations also formulate orbital relative motion equations in Cartesian coordinates but with the relaxation that the chief orbit can have arbitrary eccentricity. A derivation of these equations was also provided where all of the relative position and velocity states are assumed to be small to first order.

Chapter 3 provided the derivation of an IROD algorithm that utilizes the camera offset from the center-of-mass to determine the relative orbit of a close, neighboring satellite. The IROD algorithm uses three or more line-of-sight observations (six angle measurements) to determine the initial relative states of a neighboring satellite. A small change to the IROD camera algorithm also allows for a deputy satellite to use LOS observations to known

features on a neighboring chief satellite for relative orbit determination. This IROD solution takes the form of simple algebraic equations and requires the inversion of one matrix of dimension $3N-6$ when N is the number of observations. Results from this chapter show that the accuracy of the algorithm is dependent on the ratio of the camera offset to the deputy-chief separation distance, the time-interval between observations, and standard deviation of the measurement errors. The solution errors are proportional to the measurement error and inversely proportional to the ratio of the camera-offset to the vehicle-separation distance and for all cases examined, the solution accuracy depends on the magnitude of the camera offset or the magnitude of a known target feature offset from the center-of-mass.

Chapter 4 provided the background on previous work in relative orbital motion in a spherical coordinate frame and provides a derivation of new relative orbital motion models in spherical coordinates that take into account J_2 perturbation effects. Although the derivation for these equations in cylindrical coordinates is similar to the derivation for the Cartesian HCW equations, it is noted that there is a significant difference. Since the nonlinear equations of motion in cylindrical coordinates are not a function of $\delta\theta$ or $\delta\dot{z}$, the above linearized equations are valid for arbitrarily large $\delta\theta$ and $\delta\dot{z}$. This nuance of the linearization process in curvilinear coordinates was noted by Gobetz [45]. This is an important result of the linearization process that provides increased accuracy over the HCW equations even for arbitrarily large $\delta\theta$ (downrange separation) and $\delta\dot{z}$ (cross-track velocity). The same conclusions were drawn with the relative orbital motion equations derived in spherical coordinates. This chapter also provided a derivation of relative orbital motion equations in spherical coordinates with J_2 perturbation effects. An important caveat in this derivation is the choice of reference orbit when linearizing the nonlinear equations of motion. The reference orbit is chosen to lie in the equatorial orbital plane since expressions already exist for the J_2 perturbations in spherical coordinates as a function of the inclination from the equatorial orbital plane. Since the reference orbit is not coincident with the chief orbit, cases where the chief and deputy have large inclinations yield less accurate results. There is in fact a singularity in the relative motion equations when the orbit inclination of a satellite

approaches 90° .

Chapter 5 showed the derivation of an IROD algorithm that makes use of the previously derived relative orbital motion equations with J_2 effects from Chapter 4. The IROD algorithm uses three LOS observations (six angle measurements) and derives an approximate IROD algorithm which approximately solves a set of 6 quadratic equations in 6 unknowns. The algorithm is approximate because it neglects small, second-order terms in its derivation. A simple, iterative improvement method that re-introduces the small, second-order terms is also derived which, after a few iterations, is able to exactly solve the set of polynomial equations to numerical precision. Example cases are tested in an environment where the dynamics are linearized and the measurement equations are reduced to second-order that show that the IROD algorithm performs well when given LOS measurements that are consistent with the environment that the IROD algorithm was derived in.

Chapter 6 showed the derivation of a similar approximate IROD algorithm which makes use of more than three LOS observations to arrive at an estimate of the initial relative states. A new iterative improvement algorithm is also derived which makes use of the extra LOS observations to find the best fit to the quadratic equations in a least squares sense. Examples cases are again tested in the Linearized dynamics/Second-Order measurement equation environment to show that the IROD algorithm performs expertly, with small position errors in the initial relative states, to find an accurate estimate.

Results from Chapter 7 show that the IROD algorithm performs best in LEO when the inclination and eccentricity of the satellites considered are small. For this reason, the IROD algorithm was tested with many relative motion cases in GEO where the characterization of GEO satellites requires them to have small inclinations and eccentricities. The GEO results show that the IROD algorithm performs very well in these cases and its main future application can be GEO missions.

For LEO orbits, the effects due to J_2 can be significant [7] and previous research has shown that the effect of J_2 perturbations of relative motion at LEO is also significant [57]. Cases in Chapters 8 and 10 show that neglecting the J_2 perturbations in the IROD algorithm

when J_2 perturbations are used in generating the LOS measurements, yields large percent position errors for the initial state estimates. Neglecting the J_2 perturbations at smaller separations yields larger percent position errors than at larger separations due to the relative effect of J_2 perturbations on the LOS angles. These results show that the J_2 perturbation needs to be included in IROD algorithms for acceptable accuracy especially for small relative separations. Some preliminary analysis is also presented that shows the effect on IROD performance of varying magnitudes of measurement error in the LOS measurements. These cases show that with the camera measurement errors found in current technology, the vehicle separations must be large to find accurate IROD solutions.

Although the IROD algorithm works well in many of the cases presented in this research, there are a number of problems associated with the IROD algorithm that require further investigation. First, the IROD algorithm performs poorly at higher inclinations. This is a remnant of using the spherical coordinate frame in deriving the relative satellite motion equations. There is a singularity in the spherical coordinate frame as the inclination approaches 90° . Using the Cartesian coordinate frame would remove this singularity but it would be more difficult to include the effects of J_2 in a Cartesian coordinate frame and the Cartesian coordinate frame would lose the effect of arbitrarily large $\delta\theta$.

Another issue with the IROD algorithm deals with the iterative improvement algorithm. When nonlinearities are included in generating the LOS measurements, the iterative improvement often does not actually improve the estimate of the relative states from the IROD algorithm. As a reminder, the iterative improvement algorithm provides the exact solution (to numerical precision) to the IROD problem modelled using the second-order measurement equations and the linearized relative motion equations and does not provide the exact solution of the full, nonlinear two-body problem with J_2 perturbations. Conversely, the cases presented in Chapter 5 and 6 that generate the LOS measurements using the second-order measurement equations and linearized relative motion equations, the iterative improvement algorithm reduces the percent position errors to numerical precision, i.e., the iterative improvement algorithm works well.

Another problem of this IROD algorithm is that an increase in the number of LOS observations does not necessarily decrease the errors of the initial relative state estimates. It is expected that increasing the number of measurements would average out the errors of the IROD estimates and make the problem of disambiguation easier. Unfortunately, the LOS measurements generated with nonlinear dynamics and J_2 perturbations introduces a bias to the LOS measurements that increases the IROD estimate errors as the number of measurements increases.

There are several avenues of further investigation that would append nicely to this body of research and would be perfect follow-on projects for other Masters or Ph.D. students. A more in-depth study of the effect of measurement error on the performance of the IROD estimates is important for implementing this algorithm with real-world data. Errors in the LOS measurements can come from a variety of sources such as camera measurement errors, camera bias, camera misalignment and modeling errors. A comprehensive understanding of these error sources and their effect on the performance of the IROD estimates is vital.

The topic of disambiguity is also an important and non-trivial problem that should be investigated further in future research. As a reminder, all of this research deals with simulated cases where the initial relative states are already known and thus the problem of disambiguation is not present. In on-board applications, the true initial relative states are not known, so a set of helpful residuals can be used in a process to disambiguate multiple IROD solutions to arrive at the “best” solution. This disambiguation process is ultimately essential when sifting through actual, on-board mission LOS measurements for IROD applications. Some possible approaches to disambiguation of possible IROD estimates to arrive at the best IROD estimate include: LOS residuals, consistency checking, initializing a Kalman filter for each feasible IROD root, or initializing a nonlinear least square IROD algorithm for each feasible IROD root. Disambiguity with LOS residuals can be achieved in two ways: comparing LOS residuals using only the measurements used to obtain the IROD solution or comparing LOS residuals using other measurements that were not used to obtain the IROD solution (extra measurements). Consistency checking involves comparing the

feasible IROD solutions based on one set of measurements to the IROD solutions obtained from a different set of measurements. These and other disambiguating strategies for finding the best IROD solution are excellent avenues of future research.

Future research also includes investigating other approaches to the solution of N quadratic equations in 6 unknowns. Also, the process of feasible root selection is another useful area of research. Currently, the IROD algorithm only selects positive roots within a range acceptable for IROD algorithms. For $N > 3$ observations, there are often complex roots and only the real parts of the complex roots are used in the IROD solution. Investigating the meaning of complex roots and the criteria for feasible root selection are both prospective and important areas of research for continued validation of this IROD algorithm.

In summary, future topics include more measurement error analysis, disambiguity techniques, approaches to the solution of N quadratic equations in 6 unknowns and feasible root selection processes.

REFERENCES

- [1] Clohessy, W. and Wiltshire, R., “Terminal Guidance System for Satellite Rendezvous,” *Journal of the Aerospace Sciences*, Vol. 27, No. 9, September 1960, pp. 653–658.
- [2] Newman, B., Sinclair, A. J., Lovell, T. A., and Perez, A., “Comparison of Nonlinear Analytical Solution for Relative Orbital Motion,” *Proceedings of AIAA-AAS Astrodynamics Specialist Conference*, No. AAS-2014-4163, San Diego, California, August 2014.
- [3] Woffinden, D. C., *Angles-Only Navigation For Autonomous Orbital Rendezvous*, Ph.D. thesis, Utah State University, 2008.
- [4] Geller, D. K. and Lovell, T. A., “Angles-Only Navigation Range Observability During Orbital Rendezvous and Proximity Operations,” *Proceedings of AAS GN&C Conference - Rocky Mountain Section*, No. AAS 015-117, Breckenridge, February 2015.
- [5] Euler, E., “Optimal Low-Thrust Rendezvous Control,” *AIAA Journal*, Vol. 7, No. 6, 1969, pp. 1140–1144.
- [6] Schaub, H. and Junkins, J. L., *Analytical Mechanics of Space Systems*, AIAA Education Series, American Institute of Aeronautics and Astronautics, 2003.
- [7] Montenbruck, O. and Gill, E., *Satellite Orbits: Models, Methods, and Applications*, Springer Science & Business Media, 2000.
- [8] Hebert, L. M., *Angles-Only Initial Relative Orbit Determination via Successive Maneuvers*, Master’s thesis, Auburn University, May 2016.
- [9] Garg, S. K., *Initial Relative-Orbit Determination Using Second-Order Dynamics and Line-of-Sight Measurements*, Master’s thesis, Auburn University, May 2015.

- [10] LeGrand, K. A., “Initial Relative Orbit Determination Using Stereoscopic Imaging and Gaussian Mixture Models,” *Proceedings of 27th Annual AIAA/USU Conference on Small Satellites*, No. SSC13-VIII-6, August 2013.
- [11] Patel, H., Lovell, T., Allgeier, S., Russell, R., and Sinclair, A., “Relative Navigation for Satellite in Close Proximity Using Angles-Only Observations,” *Proceedings for 22nd AAS/AIAA Space Flight Mechanics Meeting*, No. AAS 12-202, January 2012.
- [12] Geller, D. K. and Lovell, T. A., “Non-Iterative Approximate Solution to the Angles-Only Initial Relative Orbit Determination Problem in Spherical Coordinates,” Tech. rep., Air Force Research Lab - Summer Faculty Fellowship Program, 2015.
- [13] Geller, D. K. and Perez, A. C., “Initial Relative Orbit Determination for Close-in Proximity Operations,” *Journal of Guidance, Control, and Dynamics*, Vol. 38, No. 9, September 2015, pp. 1833–1842.
- [14] Schaub, H., Vadali, R., Junkins, J. L., and Alfriend, K. T., “Spacecraft Formation Flying Control Using Mean Orbit Elements,” *Journal of Astronautical Sciences*, Vol. 48, No. 1, 2000, pp. 69–87.
- [15] Carter, T., “State Transition Matrices for Terminal Rendezvous Studies: Brief Survey and New Example,” *Journal of Guidance, Control, and Dynamics*, Vol. 21, No. 1, 1998, pp. 148–155.
- [16] Hill, G. W., “Researches in the Lunar Theory,” *American Journal of Mathematics*, Vol. 1, No. 1, 1878, pp. 5–26.
- [17] Lancaster, E., “Relative Motion of Two Particles in Elliptic Orbits,” *AIAA Journal*, Vol. 8, No. 10, 1970, pp. 1878–1879.
- [18] Van der Ha, J. C., “Exact Analytical Formulation of Planar Relative Motion,” *Astronautica Acta*, Vol. 7, No. 1, 1980, pp. 1–17.

- [19] Van der Ha, J. and Mugellesi, R., “Analytical Models for Relative Motion Under Constant Thrust,” *Journal of Guidance, Control, and Dynamics*, Vol. 13, No. 4, 1990, pp. 644–650.
- [20] Tschauner, J. and Hempel, P., “Rendezvous zu einem in elliptischer Bahn umlaufenden Ziel,” *Astronautica Acta*, Vol. 11, No. 2, March-April 1965, pp. 104–109.
- [21] Tschauner, J. and Hempel, P., “Neue Darstellung des Rendezvous bei elliptischer Zielbahn,” *Astronautica Acta*, Vol. 11, No. 5, 1965, pp. 312–321.
- [22] Yamanaka, K. and Ankersen, F., “New State Transition Matrix for Relative Motion on an Arbitrary Elliptical Orbit,” *Journal of Guidance, Control, and Dynamics*, Vol. 25, No. 1, January-February 2002, pp. 60–66.
- [23] Garrison, J. L., G., G. T., and Axelrad, P., “Relative Motion in Highly Elliptical Orbits,” *Advances in Astronautical Sciences*, Vol. 89, American Astronautical Society, Univelt, San Diego, CA, 1995, pp. 1359–1376.
- [24] Kelly, T., “An Analytical Approach to the Two-Impulse Optimal Rendezvous Problem,” *Advances in the Astronautical Sciences*, Vol. 87, No. Paper 94-156, 1994, pp. 337–347.
- [25] Brumberg, V., “Perturbation Theory in Rectangular Coordinates,” *Celestial Mechanics*, Vol. 18, 1978, pp. 319–336.
- [26] Inalhan, G., Tillerson, M., and How, J. P., “Relative Dynamics and Control of Spacecraft Formation in Eccentric Orbits,” *Journal of Guidance, Control, and Dynamics*, Vol. 25, No. 1, January-February 2002, pp. 48–59.
- [27] Melton, R. G., “Time-Explicit Representation of Relative Motion Between Elliptical Orbits,” *Journal of Guidance, Control, and Dynamics*, Vol. 23, No. 4, July-August 2000, pp. 604–610.

- [28] Schaub, H., “Relative Orbit Geometry Through Classical Orbit Element Differences,” *Journal of Guidance, Control, and Dynamics*, Vol. 27, No. 5, September-October 2004, pp. 839–848.
- [29] De Vries, J., “Elliptic Element in Terms of Small Increments of Position and Velocity Components,” *AIAA Journal*, Vol. 1, No. 9, 1963, pp. 2626–2629.
- [30] Lawden, D. F., “Fundamentals of Space Navigation,” *Journal of the British Interplanetary Society*, Vol. 13, 1954, pp. 87–101.
- [31] Carter, T., “New Form for the Optimal Rendezvous Equations Near Keplerian Orbit,” *Journal of Guidance, Control, and Dynamics*, Vol. 13, No. 1, 1990, pp. 183–186.
- [32] London, H. S., “Second Approximation to the Solution of the Rendezvous Equations,” *AIAA Journal*, Vol. 1, No. 7, 1963, pp. 1691–1693.
- [33] Anthony, M. L. and Sasaski, F. T., “Rendezvous Problem for NeNear Circular Orbits,” *AIAA Journal*, Vol. 3, No. 9, September 1965, pp. 1666–1673.
- [34] Stringer, M., Newman, B., Lovell, T., and Omran, A., “Second Order Nonlinear Initial Value Solution for Relative Motion Using Volterra Theory,” *Proceedings of the AAS-AIAA Space Flight Mechanics Meeting*, No. AAS-13-469, Lihue, Hawaii, February 2013.
- [35] Sengupta, P. and Vadali, R., “Relative Motion and the Geometry of Formations in Keplerian Elliptic Orbits,” *Journal of Guidance, Control, and Dynamics*, Vol. 30, No. 4, 2007, pp. 953–964.
- [36] Gim, D.-W. and Alfriend, K. T., “State Transition Matrix of Relative Motion for the Perturbed Noncircular Reference Orbit,” *Journal of Guidance, Control, and Dynamics*, Vol. 26, No. 6, November-December 2003, pp. 956–971.
- [37] Woffinden, D. and Geller, D., “Observability Criteria for Angles-Only Navigation,” *IEEE Transactions on Aerospace and Electronic Systems*, Vol. 45, No. 3, 2009, pp. 1194–1208.

- [38] Schneider, A. M., Prussing, J. E., and Timin, M. E., “A Manual Method for Space Rendezvous Navigation and Guidance,” *Journal of Spacecraft and Rockets*, Vol. 6, No. 9, 1969, pp. 998–1006.
- [39] Geller, D. and Klein, I., “Angles-Only Navigation State Observability During Orbital Proximity Operations,” *Journal of Guidance, Control, and Dynamics*, Vol. 37, No. 6, November-December 2014, pp. 1976–1983.
- [40] Stern, R. G., *Interplanetary Midcourse Guidance Analysis*, Ph.D. thesis, Massachusetts Institute of Technology, 1963.
- [41] Jones, J. B., “A Solution of the Variational Equations for Elliptic Orbits in Rotating Coordinates,” *Proceedings of AIAA/AAS Astrodynamics Conference*, No. AIAA Paper 80-1690, Aug. 1980.
- [42] Berreen, T. and Crisp, J., “An Exact and a New First-Order Solution for the Relative Trajectories of a Probe Ejected from a Space Station,” *Celestial Mechanics*, Vol. 13, 1976, pp. 75–88.
- [43] Alfriend, K. T., Vadali, R., Gurfil, P., and How, J., *Spacecraft Formation Flying: Dynamics, Control and Navigation*, Elsevier, 2009, pp. 99-103.
- [44] Geller, D. and Lovell, T., “Relative Orbital Motion and Angles-Only Relative State Observability in Cylindrical Coordinates,” *Proceedings of the AAS-AIAA Space Flight Mechanics Meeting*, No. AAS-14-211, Santa Fe, New Mexico, January 2014.
- [45] Gobetz, F., “Optimal Variable-Thrust Transfer of a Power-Limited Rocket,” *AIAA Journal*, Vol. 2, No. 2, 1964, pp. 339–343.
- [46] Karlgaard, C. and Lutze, F., “Second-Order Relative Motion Equations,” *Journal of Guidance, Control, and Dynamics*, Vol. 26, No. 1, January-February 2003, pp. 41–49.
- [47] Schweighart, S. and Sedwick, R. J., “High-Fidelity Linearized J2 Models for Satellite Formation Flight,” *Journal of Guidance, Control, and Dynamics*, Vol. 25, No. 6, November-December 2002, pp. 1073–1080.

- [48] Kechichian, J. and Kelly, T., “Analytical Solution of Perturbed Motion in Near-Circular Orbit Due to J2, J3 Earth Zonal Harmonics in Rotating and Inertial Cartesian Reference Frames,” *Proceedings of Aerospace Sciences Meeting*, No. AIAA 89-0352, Reno, Nevada, January 1989.
- [49] Schaub, H. and Alfriend, K. T., “J2 Invariant Relative Orbits for Spacecraft Formations,” *Celestial Mechanics*, Vol. 79, 2001, pp. 77–95.
- [50] Pulliam, W., “Catcher’s Mitt Final Report,” Tech. rep., Defence Advanced Research Projects Agency, 2010.
- [51] Curtis, H. D., *Orbital Mechanics for Engineering Students*, Elsevier Ltd., 2010, pp. 316-330.
- [52] Newman, B., Lovell, T. A., Pratt, E., and Duncan, E., “Quadratic Hexa-Dimensional Solution for Relative Orbit Determination,” *Proceedings of AIAA-AAS Astrodynamics Specialist Conference*, No. AIAA-2014-4309, San Diego, California, August 2014.
- [53] LeGrand, K. A., DeMars, K. J., and Darling, J. E., “Solutions of Multivariate Polynomial Systems Using Macaulay Resultant Expressions,” *Proceedings of AIAA-AAS Astrodynamics Specialist Conference*, No. AAS 014-229, 2014.
- [54] Aldrin, E. E., *Line-Of-Sight Guidance Techniques For Manned Orbital Rendezvous*, Ph.D. thesis, Massachusetts Institute of Technology, 1963.
- [55] Moon, T. K. and Stirling, W. C., *Mathematical Methods and Algorithms*, Prentice Hall, 2000, Chapter 7.
- [56] Harville, D., *Matrix Algebra From a Statistician’s Perspective*, Springer-Verlag, 1st ed., 1997.
- [57] Gong, B., Geller, D., and Luo, J., “Initial Relative Orbit Determination Analytical Error Covariance and Performance Analysis For Proximity Operations,” *Proceedings of AAS/AIAA Astrodynamics Specialist Conference*, Vail, CO, August 2015.

- [58] Geller, D. and Lovell, T. A., “Initial Relative Orbit Determination Performance Analysis in Cylindrical Coordinates Using Angles-Only Measurements,” *Proceedings of AAS/AIAA Spaceflight Mechanics Meeting*, No. AAS 14-212, Santa Fe, NM, January 2014, pp. 149–165.

CURRICULUM VITAE

Alex Perez
 18 Banks Street, Unit #2
 Belmont, MA
 +(801) 921-2686
 alexclarkeperez@gmail.com

Education

- Ph.D.** **Mechanical Engineering, Utah State University, Logan, Utah, 2016.**
Dissertation: Applications of Relative Satellite Motion Models Using Curvilinear Coordinate Frames
- M.S.** **Aerospace Engineering, Utah State University, Logan, Utah, 2015.**
- B.S.** **Mechanical Engineering, Brigham Young University, Provo, Utah, 2012.**
Senior Design Project: Formula Hybrid SAE Competition, 1st Place
- B.A.** **Russian Language, Brigham Young University, Provo, Utah, 2012.**

Work Experience

2016-Present Navigation Engineer, Draper, Cambridge, MA

Supporting Technical Staff, GN&C for DreamChaser

2016,2014,2013 AFRL Space Scholar Summer Intern/Summer Faculty Fellowship Program, Kirtland AFB, NM

Solved problems dealing with Closed-Loop GN&C Linear Covariance Analysis, Relative Satellite Motion and Initial Relative Orbit Determination.

- 2015 College Intern, Lockheed Martin, Littleton, CO
Provided support for GN&C Software Engineering Team related to rendezvous and proximity operations. Implemented collision detection code to be used in trajectory planning.
- 2012-2016 Graduate Research Assistant, Utah State University, Logan, UT
Researched aerospace engineering topics such as guidance, navigation, and control of spacecraft, relative satellite motion, convex optimization and linear covariance analysis. See below for more research projects.
- 2013 Numerical Methods Instructor, Utah State University, Logan, UT
Taught undergraduate course in numerical methods with a particular focus in programming with Fortran and MATLAB.
- 2013 Instrumentation Teaching Assistant, Utah State University, Logan, UT
Conducted instrumentation lab sessions and taught correct instrumentation engineering principles.

Research Projects

- 2016 Initial Relative Orbit Determination with J_2 Perturbations
Solved problems dealing with Closed-Loop GN&C Linear Covariance Analysis, Relative Satellite Motion and Initial Relative Orbit Determination.
- 2014 Relative Motion Solutions Using Curvilinear Coordinate Frames
Derived new relative motion solutions using formulations of the HCW equations in spherical and cylindrical coordinate frames.
- 2014 Effect of Camera Offset on Range Observability
Provided support for GN&C Software Engineering Team related to rendezvous and proximity operations. Implemented collision detection code to be used in trajectory planning.

- 2013 Closed-Loop GN&C Linear Covariance Analysis for Mission Safety
 Developed a Linear Covariance tool for relative motion rendezvous and proximity operations for mission safety design.

Publications

- Geller, D. and Perez, A., “Initial Relative Orbit Determination for Close-in Proximity Operations,” *Journal of Guidance, Control, and Dynamics*, Vol. 38, No. 9, September 2015, pp.1833-1842
- Perez, A., Lovell, T.A., and Geller, D., “Applications of Relative Satellite Motion Modeling Using Curvilinear Coordinate Frames,” *Proceedings of AAS/AIAA Astrodynamics Specialist Conference, Vail, CO, August 2015, AAS 015-678*
- Perez, A., Gunther, J., and Geller, D., “Relative Satellite Motion Optimal Control Using Convex Optimization,” *Proceedings of AAS/AIAA Astrodynamics Specialist Conference, Vail, CO, August 2015, AAS 015-679*
- Perez, A., Lovell, T. A., “Nonlinear Representations of Satellite Relative Motion Equations Using Curvilinear Transformations,” *Proceedings of AAS GN&C Conference - Rocky Mountain Section, Breckenridge, CO, January 2015, AAS 015-118*
- Perez, A., Lovell, T.A., Geller, D, Newman, B., “Relative Satellite Motion Solutions Using Curvilinear Coordinate Frames,” *Proceedings of AAS/AIAA Space FLight Mechanics Meeting, January 2015, Williamsburg, AAS 015-437*
- Newman, B., Lovell, T. A., Sinclair, A., Perez, A., “Comparison of Nonlinear Analytical Solutions for Relative Orbital Motion,” *Proceedings of AAS/AIAA Astrodynamics Specialist Conference, San Diego, CA, August 2014*
- Perez, A., “Closed-Loop GN&C Linear Covariance Analysis for Mission Safety,” *Proceedings of American Astronautical Society GN&C Conference - Rocky Mountain Section, Breckenridge, CO, January 2014, AAS 014-016*

Computer Skills

Computer Languages MATLAB, Simulink, Fortran

Office Suites Microsoft Office (Word, Excel, PowerPoint)

Language Skills

Fluent: English

Intermediate-High: Russian

Personal Interests

Reading, running, gaming, history